This electronic thesis or dissertation has been downloaded from Explore Bristol Research, http://research-information.bristol.ac.uk

Author:
Petkov, Alexander

Title:
Material properties of gallium oxides

material integration, thermal anisotropy, irradiation effects

General rights
Access to the thesis is subject to the Creative Commons Attribution - NonCommercial-No Derivatives 4.0 International Public License. A copy of this may be found at https://creativecommons.org/licenses/by-nc-nd/4.0/legalcode This license sets out your rights and the restrictions that apply to your access to the thesis so it is important you read this before proceeding.

Take down policy
Some pages of this thesis may have been removed for copyright restrictions prior to having it been deposited in Explore Bristol Research. However, if you have discovered material within the thesis that you consider to be unlawful e.g. breaches of copyright (either yours or that of a third party) or any other law, including but not limited to those relating to patent, trademark, confidentiality, data protection, obscenity, defamation, libel, then please contact collections-metadata@bristol.ac.uk and include the following information in your message:

- Your contact details
- Bibliographic details for the item, including a URL
- An outline nature of the complaint

Your claim will be investigated and, where appropriate, the item in question will be removed from public view as soon as possible.

Material properties of gallium oxides: material integration, thermal anisotropy, irradiation effects

By

Alexander Petkov

Department of Physics
University of Bristol

A dissertation submitted to the University of Bristol in accordance with the requirements of the degree of Doctor of Philosophy in the Faculty of Science.

January 2023

Word count: ~ 28,000

ABSTRACT

Gallium oxide (Ga_2O_3) is an ultra-wide band gap semiconductor with potential applications in power electronics due to its high predicted breakdown field (significantly higher than in materials such as SiC or GaN). One of Ga_2O_3's main drawbacks is its low and anisotropic thermal conductivity, which can be a limiting factor in thermal management for potential devices. Furthermore, low hole mobility makes impractical the use of any potential p-type Ga_2O_3. Because of this, the incorporation of Ga_2O_3 with other materials for improved thermal management, as well as designing well performing p-n junctions, is important for the further development of Ga_2O_3 technology.

While different types of adhesion of Ga_2O_3 to higher thermal conductivity substrates have been demonstrated, the effects of anisotropic thermal transport on the potential interface thermal boundary resistances has not been well studied. It is also notable that multiple Ga_2O_3 polymorphs exist (although the β phase is the most stable and most well studied). These polymorphs are known to have varying electronic properties, which could be tied back to the varying local coordination environments. This implies that as a result of irradiation damage or ion doping, induced structural defects could affect Ga_2O_3's electronic properties, or possibly lead to a partial or full polymorph transition. Therefore, understanding the structural changes in Ga_2O_3 as a result of ion implantation/irradiation is important.

In this thesis, we review several methods for adhesion of Ga_2O_3 to higher thermal conductivity substrates, discussing their benefits and drawbacks. We simulate the thermal boundary resistance (TBR) between β-Ga_2O_3 of different crystallographic orientations and (100) diamond with a Van der Waals bonded interface. We find said TBR to vary by as much as 70% depending on the β-Ga_2O_3 crystal face used at the interface, lowest for (100) β-Ga_2O_3 as 48.6 ± 0.3 m^2KGW^{-1}. We further estimate that the TBR between β-Ga_2O_3 and diamond can be reduced by at least 3.6 times when the bonding is realised through a 10 nm amorphous Al_2O_3 interlayer, compared to a direct Van der Waals interface.

We further investigate a method for thin film (ranging between 8 and 30 nm in thickness) Ga_2O_3 deposition from oxidised liquid gallium. We measure the valence band offset of the thin film to an SiO_2 substrate using x-ray photoelectron spectroscopy to be 0.1 eV and comment on what this implies for a potential interface with Si and diamond. We also measure the thin film's out of plane thermal conductivity as 3 ± 0.5 $Wm^{-1}K^{-1}$ using transient thermoreflectance.

Results from an in situ ion irradiation experiment on β-Ga_2O_3 using 200 keV Ar ions are discussed. We observe an anisotropic shrinking of the material's lattice dimensions with increasing irradiation dose. While the material's structure remains in the β polymorph, extra reflections appear in the material's diffraction pattern above an irradiation dose of 2 displacements per atom. We discuss the possible source of these. We also note a different mode for damage formation at higher incident ion energies, showing the absence of some of the complex defects (seen under 200 keV Ar ion irradiation) when irradiating β-Ga_2O_3 with Ar ions of 2 MeV incident energy. We propose a cellular automaton model of the ion irradiation process in β-Ga_2O_3, which suggests a significant decrease in the average local Ga-ion coordination number, which is expected to lead to changes in the material's electronic properties.

DEDICATION AND ACKNOWLEDGEMENTS

I would like to thank Martin Kuball and James Pomeroy, who acted as my supervisors for the duration of my PhD and supported my research in all of its tumultuous twists and turns. I would also like to thank all the researchers who helped me with experiments or useful discussion. None of this would have been possible without you. I want to thank Mattia Cattelan for his expertise and help in using the NanoESCA facility to take XPS measurements. Special thanks go to Jude Lavrock for his support and helpful comments. Big thanks go to Dan Field, who helped me with taking transient thermoreflectance (TTR) measurements and introduced me to the modelling procedure for results interpretation. Big thanks go to Abhishek Mishra who worked alongside me on thin film Ga_2O_4 from liquid gallium deposition. I also want to acknowledge the help of Andrew Murray, who trained me on most of the cleanroom equipment I've been using throughout my research, as well as Natalie Pridmore for help in using and analysing x-ray powder diffraction. Special thanks go to Aditya Kundapura for working alongside me on bonding trial experiments.

I want to give special thanks to David Cherns for his invaluable advice on working with and analysing transmission electron microscope (TEM) data, as well as his support throughout my research into irradiation effects on β-Ga_2O_3. Huge thanks also go to Dong Liu for her considerable involvement in said research, including data procured at Argonne Lab, USA. Big thanks go to Junliang Liu (from the University of Oxford) and Luke Antwis (from the Surrey Ion Beam Centre) for their help in preparing irradiated samples for TEM study.

I want to thank Taylor Moule, Filip Wach, Thomas Gerrer and Zeina Abdallah for their support and advice that has undoubtedly help me work through complex problems. I want to thank all my colleagues at the Centre for Device Thermography and Reliability (CDTR) as well as cohort 5 of the Condensed Matter Physics Centre for Doctoral Trainng (CMPCDT) for being a lovely bunch that has been a pleasure to work alongside. Big thanks also go to Chris Bell and Neil Fox for their advice and support during annual progress meetings. I also want to thank everyone I've worked alongside here at the University of Bristol, outside the context of my research, including Terence McMaster, the Equality Diversity and Inclusion Committee as well as the other demonstrators in the 2nd year Teaching Labs. The last few years would not have been the same without you all.

Immesurable thanks go to my family for their patience and support during the course of my research. I want to thank my closest friends who have consistently made my days brighter. I dedicate my accomplishments to you.

The author of this thesis acknowledges funding and support from the Engineering and Physical Sciences Research Council (EPSRC) Centre for Doctoral Training in Condensed Matter Physics (CDTCMP), Grant No. EP/L015544/1.

AUTHOR'S DECLARATION

I declare that the work in this dissertation was carried out in accordance with the requirements of the University's Regulations and Code of Practice for Research Degree Programmes and that it has not been submitted for any other academic award. Except where indicated by specific reference in the text, the work is the candidate's own work. Work done in collaboration with, or with the assistance of, others, is indicated as such. Any views expressed in the dissertation are those of the author.

SIGNED: .... DATE: ....

TABLE OF CONTENTS

Page

List of Tables **xi**

List of Figures **xiii**

1 Introduction **1**
- 1.1 Motivation . . . 1
- 1.2 Existing challenges . . . 3
  - 1.2.1 Gallium oxide and anisotropy . . . 4
- 1.3 Polymorphism in gallium oxide . . . 4
  - 1.3.1 Radiation damage and doping . . . 7
- 1.4 Thesis structure . . . 7
- 1.5 Outcomes and future direction . . . 8

2 Gallium oxide to substrate bonding: Review and experiments **11**
- 2.1 Gallium oxide substrates growth . . . 11
- 2.2 Ga_2O_3 adhesion to other materials . . . 15
  - 2.2.1 Van der Waals adhesion . . . 15
  - 2.2.2 Direct bonding . . . 16
  - 2.2.3 Epitaxial growth . . . 19
  - 2.2.4 Diamond growth on Ga_2O_3 . . . 20
- 2.3 Summary . . . 22

3 Electrical and thermal characterisation of liquid metal thin film Ga_2O_3-SiO_2 heterostructures **25**
- 3.1 Introduction . . . 25
- 3.2 Methods . . . 26
  - 3.2.1 Thin film deposition from liquid gallium . . . 26
  - 3.2.2 X-ray photoelectron spectroscopy . . . 28
  - 3.2.3 Transient thermoreflectance . . . 30
- 3.3 Results and discussion . . . 32

3.3.1 Band alignment to substrate . . . 32
3.3.2 Thermal transport across interface . . . 34
3.4 Conclusion . . . 37

4 Molecular dynamics study of thermal transport across Ga_2O_3 - substrate interfaces 39
4.1 Introduction . . . 39
4.2 Methods . . . 40
4.3 Simulations and results . . . 42
4.3.1 Thermal conductivity simulations . . . 42
4.3.2 Thermal interface simulations . . . 45
4.4 Conclusion . . . 47

5 Structural changes to β-Ga_2O_3 under ion irradiation 49
5.1 Introduction . . . 49
5.2 Methodology . . . 50
5.2.1 Quantifying irradiation dose . . . 50
5.2.2 Analysing TEM images and diffraction patterns . . . 52
5.3 Results . . . 55
5.3.1 Low irradiation doses (below 1 dpa) . . . 55
5.3.2 Higher irradiation doses (above 1 dpa) . . . 57
5.4 Conclusion . . . 62

6 Modelling of defect evolution in β-Ga_2O_3 from ion radiation 65
6.1 Introduction . . . 65
6.2 Methodology . . . 66
6.2.1 SRIM simulations . . . 66
6.2.2 Cellular automaton model . . . 67
6.3 Results . . . 70
6.3.1 Coordination number and vacancy evolution . . . 70
6.3.2 TEM analysis . . . 72
6.3.3 Effects of ion energy on defect production . . . 74
6.4 Conclusion . . . 76

7 Conclusions and future work 79

A Code and input files 87
A.1 LAMMPS code . . . 87
A.2 Cellular automaton code . . . 92

B List of abbreviations **107**

Bibliography **109**

LIST OF TABLES

TABLE **Page**

1.1 Some properties of β-Ga_2O_3 and other common wide bandgap materials, relevant for high power electronics. 3

3.1 Table of biding energies used for valence band offset determination. 34
3.2 Parameters used for the TTR fitting. 36

4.1 Table of pairwise interaction parameters for Born-type interatomic potential in Equation (4.1) 41
4.2 TBR values across interfaces between different orientations of β-Ga_2O_3 and two materials: (100) diamond and amorphous Al_2O_3. 47

6.1 Table of β-Ga_2O_3 unit cell base and interstitial sites, including fractional coordinates, occupation energies, and nearest neighbours for displacement. 68

LIST OF FIGURES

FIGURE **Page**

1.1 Relevance of gallium oxide in power electronics 2
1.2 Visualisation of Ga_2O_3 β, α and κ polymorph unit cells 5
1.3 Visualisation of Ga_2O_3 ϵ and γ polymorph unit cells 6

2.1 Diagram of Czochralski and Edge-defined film-fed growth methods for bulk Ga_2O_3 . . 12
2.2 Diagram showing the near close packed planes in β-Ga_2O_3 13
2.3 Diagram of donor and acceptor levels within a material band gap 14
2.4 Atomic force microscope image of (010) β-Ga_2O_3 flake deposited onto silicon with thermal oxide 15
2.5 Diagram of the method for direct hydrophilic bonding of gallium oxide to diamond . . 17
2.6 Diagram of the equipment used for applying pressure to Ga_2O_3 directly bonded to Si using Al_2O_3 interlayer 18
2.7 SEM image and EDX analysis of diamond film grown on β-Ga_2O_3 21

3.1 Diagram of exfoliation method, image of deposition, and linescans across deposition edge 27
3.2 Diagram of x-ray photoelectron spectroscopy 29
3.3 Diagram of the transient thermoreflectance (TTR) experimental setup 31
3.4 XPS energy spectra of sample, and band alignment diagram of deposited G_2O_3 to other materials 33
3.5 TTR measurement and modelling of thermal transport across deposited Ga_2O_3-SiO_2-Si interface 36

4.1 Visualisation of boundary conditions in LAMMPS 40
4.2 Visualisation of a Ga_2O_3 slab used in the $< 100 >$ thermal conductivity simulations with extracted temperature profile 43
4.3 Relationship between inverse thermal conductivity and inverse size of simulation box for each of the main crystallographic directions of Ga_2O_3 44
4.4 Visualisation of (010) Ga_2O_3 to diamond system; (001) Ga_2O_3 to Al_2O_3 system - both with extracted temperature profiles 46

4.5 Simulations of the temperature profile across β-Ga_24O_3 to amorphous Ga_2O_3 heterojunctions . . . 48

5.1 IVEM-Tandem facility TEM diagram and imaging schematic . . . 51
5.2 Example Bright Field image and contrast profile . . . 52
5.3 TEM diffraction schematics . . . 54
5.4 Indexed diffraction pattern data at low levels of irradiation . . . 56
5.5 Changes with irradiation to the estimated $d_{(020)}$ and $d_{(\overline{7}\overline{1}2)}$ interplane spacings . . . 57
5.6 Diffraction pattern data for higher levels of irradiation . . . 59
5.7 Simulated diffraction pattern data for different sublattice symmetry in β-Ga_2O_3 . . . 61

6.1 β-Ga_2O_3 unit cell with added interstitial sites . . . 69
6.2 Cellular automaton model of β-Ga_2O_3 Ga-ion coordination number, energy per atom for occupied sites and total vacancies as a function of ion damage level . . . 71
6.3 TEM images of irradiated band in β-Ga_2O_3 under 2 MeV Ar ion irradiation . . . 73
6.4 Ion energy loss plots for varying Ar ion energy irradiation of β-Ga_2O_3 . . . 75
6.5 Recoils distribution for different Ar ion energy radiation onto β-Ga_2O_3 . . . 76

CHAPTER 1

INTRODUCTION

The study of wide bandgap semiconductors (WBGS) is relatively new compared to that of silicon and III-V semiconductors such as GaAs. Most notable among these materials, defined as having bandgaps above 2.2 eV, are SiC and GaN, with bandgaps of 3.2 and 3.4 eV respectively. These materials also have high critical breakdown field and high saturated drift velocity. Because of this, they have the potential for achieving higher device reliability, power, frequency and temperature operation than devices made from traditional semiconductors such as Si.

1.1 Motivation

Gallium oxide is an ultra-wide band gap material (4.8 eV for its β polymorph[1]) that has attracted a lot of attention for power electronics in recent years. Its breakdown electric field is predicted to be around 8 $\mathrm{MVcm^{-1}}$,[2] significantly higher than the 2.6 $\mathrm{MVcm^{-1}}$ and 3.3 $\mathrm{MVcm^{-1}}$ for the currently considered materials in power electronics SiC and GaN respectively,[3] offering the potential for ultra-high voltage power device technology even exceeding 10 kV. This is further illustrated in Figure 1.1 **a)**, taken from Pearton *et al.*,,[4], where gallium oxide and other commonly used semiconductors are compared with respect to their operational voltage capabilities. A high critical breakdown field is crucial for power switching applications, meaning it is possible for gallium oxide to supplement Si and SiC devices for use as power converters.

β-Ga_2O_3 also has a Baliga figure of merit superior to that of SiC or GaN, which implies reduced conduction losses in potential power-switching devices.[7] Values for the Baliga figure of merit and other material properties relevant for power electronics are given in Table 1.1 for a few notable wide (and ultra-wide) bandgap materials. An illustration of the significance of the Baliuga figure of merit (BFOM) can be seen in Figure 1.1 **b)** (taken from Chabak *et al.,*[5]).

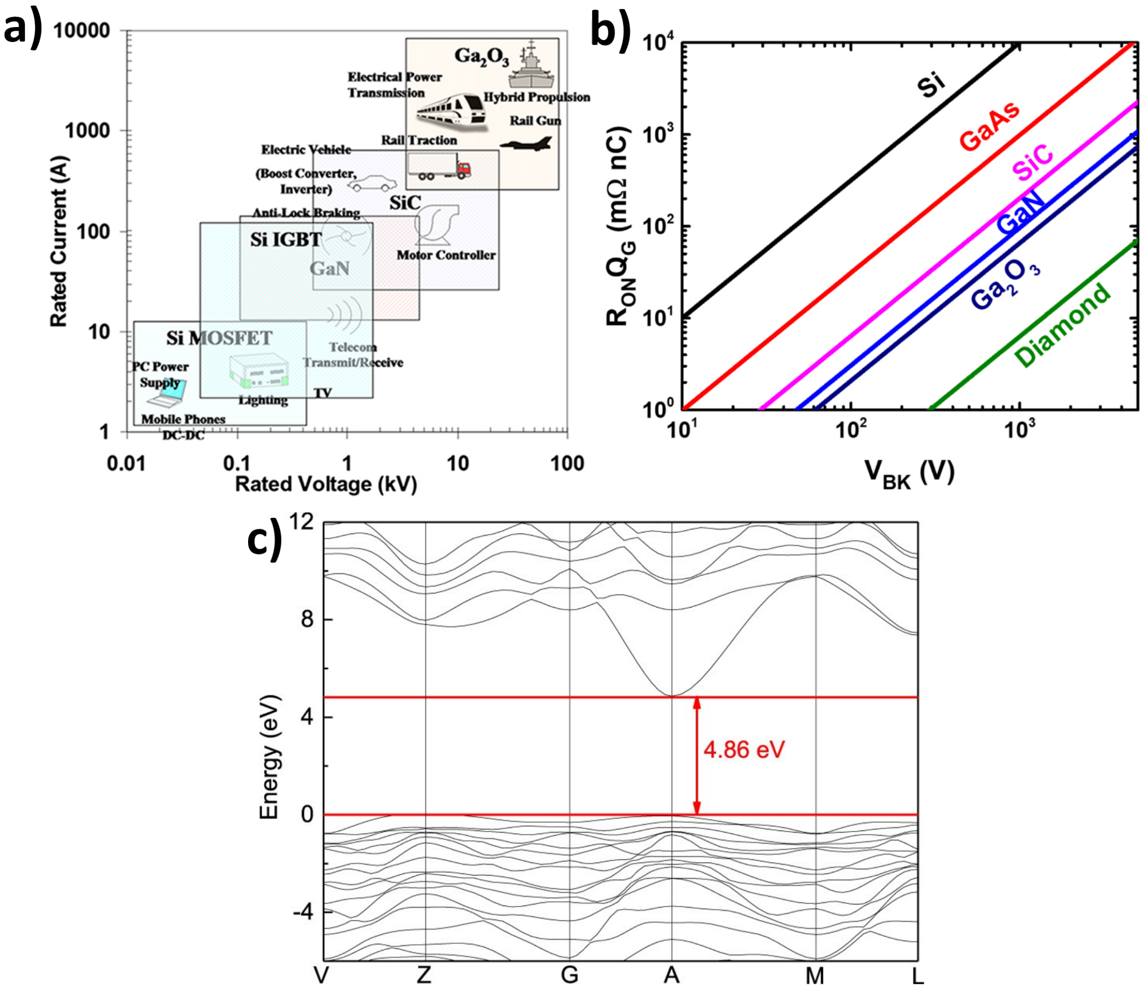

FIGURE 1.1. **a)** Possible power electronics applications for wide bandgap materials depending on operational voltage requirements (Reused with permission from Pearton *et al.,* [4]); **b)** Specific on-resistance for vertical power switches versus breakdown voltage for different materials (lines represent constant Baliga figure of merit) (Reused with permission from Chabak *et al.,* [5]); **c)** Band structure of β-Ga$_2$O$_3$ (Reused with permission from Wei *et al.,* [6])

The straight lines signify theoretical limits for device operation for constant BFOM, showing an expected lower specific on-resistance for a vertical power switches using gallium oxide, compared to SiC or GaN. It should be noted that β-Ga$_2$O$_3$ has electron mobility lower than that of SiC or GaN (as seen from Table 1.1), which can correlate with lower switching speeds. However, the predicted lower on-resistance suggests it's possible to achieve more efficient devices when using gallium oxide.

As can be seen from the data presented in Table 1.1, other materials, such as AlGaN also have significant potential for high-voltage applications that can exceed the capabilities of currently

Table 1.1: Some properties of β-Ga_2O_3 and other common wide bandgap materials, relevant for high power electronics.

Parameter	SiC	GaN	$Al_{0.7}Ga_{0.3}N$	β-Ga_2O_3	Diamond
Bandgap, E_g [eV]	3.3	3.4	5.8	4.85	5.5
Critical breakdown field, E_C [MVcm^{-1}]	2.6	3.3	12.7	8	10
Dielectric constant, ε	9.7	9	8.7	10	5.5
Electron mobility, μ_e [cm^{2}V^{-1}s^{-1}]	1000	1200	310	250	2000
Hole mobility, μ_h [cm^{2}V^{-1}s^{-1}]	90 - 120	120	30	N/A	450
Thermal conductivity, T_c [Wm^{-1}K^{-1}]	420	160	320	10 - 30	2000
Doping	n-type, p-type	Primarily n-type	Primarily n-type	n-type	Primarily p-type
Baliga Figure of Merit, $\varepsilon\mu_e E_C^4$	340	870	11773	2870	24660

Values and data in table extracted from review articles by Pearton *et al.* [4] [8]

used SiC and GaN devices. A significant benefit of gallium oxide over such materials, however, is in the low cost of device technology. This is due to the availability of melt-grown Ga_2O_3 substrates (currently up to 6 inch), making the material competitive with SiC, with the growth costs for gallium oxide wafers already ~3 times lower than for SiC and continuing to drop. [9]

All these factors - high voltage capability, reduced conduction losses in power switching, as well as the low cost of wafer production - has made gallium oxide an attractive material for power electronic devices for use in various high-voltage applications. Some potential areas for gallium oxide applications are terrestrial (including power conversion, electric vehicles, data centres[4]). Others are space-based (such as telecommunication or navigation satellites),[10] where a potential device could be subjected to various types of radiation (including electrons, protons as well as heavy ions) with energies of up to several hundred MeV.[11] There has also been significant interest in the fabrication of 2D thin film gallium oxide for potential applications in gas sensing,[12] water-splitting solar cells[13] and even wearable electronics.[14]

1.2 Existing challenges

One of the main challenges that using Ga_2O_3 in devices presents has to do with thermal transport. The most thermodynamically stable phase of gallium oxide - β-Ga_2O_3 has a relatively small thermal conductivity, which is also anisotropic, ranging between 11 Wm^{-1}K^{-1} and 27 Wm^{-1}K^{-1} depending on crystallographic direction . [15] [16] To put this in perspective, the relevant values for SiC and GaN are about an order of magnitude higher as 420 Wm^{-1}K^{-1} and 160 Wm^{-1}K^{-1}

respectively.[17] For any potential device, the low thermal conductivity of the semiconductor may lead to device failure under operation due to a significant self-heating effect. One common solution to this is the integration of gallium oxide with a high thermal conductivity material/substrate in order to form a superjunction. Numerous approaches have been reported including integration with SiC via wafer bonding, where heating effects have been predicted to reduce by up to 30% for a bottom side cooling scheme.[18]

Another issue with Ga_2O_3 is its poor hole mobility. This can be appreciated from the β-Ga_2O_3 band structure in Figure 1.1 **c)** (taken from Wei *et al.,*[6]). A flat valence band correlates with a high effective hole mass and therefore a negligible hole mobility. This, together with the lack of suitable shallow acceptors, makes Ga_2O_3-based bipolar or p-type devices so far impossible.[19] This is in contrast with the other wide bandgap materials discussed, such as GaN and AlGaN, where the use of p-type doping is possible but less common due to higher acceptor ionisation energies.[4]

A p-n junction, however, can still be established by integration of n-type Ga_2O_3 with a p-type material, which has been accomplished with p-doped nickel oxide for the purpose of diodes with tuneable electrical and optical properties,[20] as well as p-doped GaN for self-powered photodetectors.[21] Furthermore, modelling showed that a p-n Ga_2O_3-diamond superjunction would lead to approximately 60% reduction in temperature rise under operation.[22]

1.2.1 Gallium oxide and anisotropy

The anisotropy in β-Ga_2O_3's properties, however, is not limited to its thermal conductivity. For example, the light absorption coefficient for the material depends significantly on the direction of linear polarization of the light.[23] There is also evidence that the band alignment of crystalline β-Ga_2O_3 with other materials depends on the crystallographic orientation of the crystal towards the interface.[24]

It is likely that the anisotropy within the material has even more significant effects on potential devices. For example, it has been found that the forward conduction in Ga_2O_3 trench Schottky barrier diodes is dependent on the orientation of the fin-channels.[25] Because of this, considering the anisotropy in β-Ga_2O_3 and its effect on potential devices is of great importance. So far, there is no comprehensive study on the effects of anisotropy in β-Ga_2O_3 on device architecture.

1.3 Polymorphism in gallium oxide

The most widely studied phase of gallium oxide is the β phase, which has a $C12/m1$ space group and is thermodynamically stable up 2,400°C.[26] Other notable phases are α, ϵ, κ and γ, with space groups of $R\bar{3}2/c$, P_63mc, $Pna2_1$ and $Fd\bar{3}m$ respectively, κ being a more ordered subgroup of ϵ.[27] According to first principles calculations, the κ phase has the second lowest formation energy after β and converts to the latter only after prolonged annealing over 800°C.[28] It has

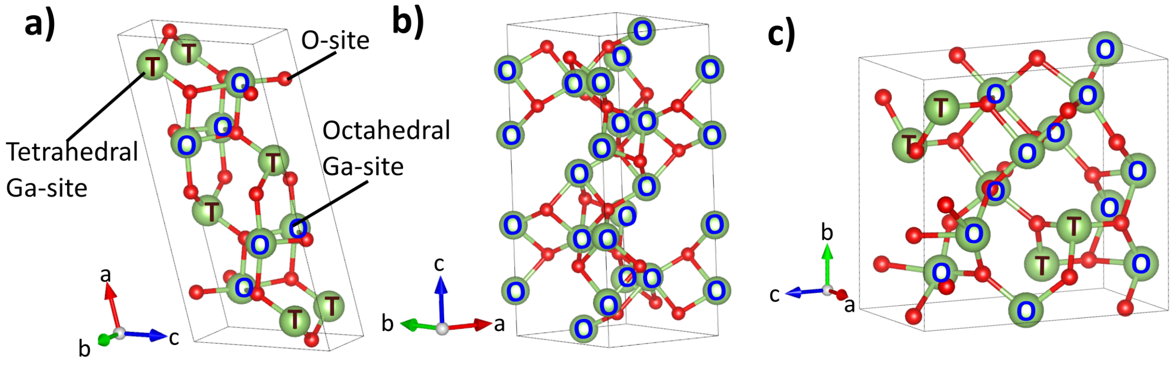

FIGURE 1.2. Visualisation of the unit cells of the **a)** β, **b)** α and **c)** κ polymorphs of Ga_2O_3.

been shown that other grown phases of gallium oxide also revert to the β phase when annealed at high temperatures.[15] The unit cells of the β, α and κ polymorphs, visualised with the help of the VESTA software, can be appreciated in Figure 1.2. One notable distinction between the polymorphs is the ratio between octahedrally (GaO_6) and tetrahedrally (GaO_4) occupied cationic sites. This ratio is 1:1 in the β polymorph, but 3:1 in κ, while Ga-sites in α-Ga_2O_3 are purely octahedral.

The structures of the ϵ and γ polymorphs, on the other hand, are more complicated due to the fractional occupancy of the Ga-sublattice sites. ϵ-Ga_2O_3 has 3 types of gallium sites (as seen in Figure 1.3 **a)**), two of each within a unit cell. Only one of the three is tetrahedral.However, the octahedral to tetrahedral Ga-ion ratio is not 2:1, but closer to 2.15 due to the macroscopic distribution of the site types within the ϵ phase. Similarly, for γ-Ga_2O_3 there are 3 types of Ga-sublattice sites. There are 48 tetrahedral sites with occupancy 0.122, 16 octahedral sites with occupancy of 0.5690 and 8 tetrahedral sites of occupancy 0.797. The γ-Ga_2O_3 unit cell is shown in Figure 1.3 **b)**). For γ-Ga_2O_3 the octahedral to tetrahedral Ga-ion ratio is around 0.74 - being the only considered phase of Ga_2O_3 with a higher number of tetrahedrally occupied Ga-sites.[29].

The shift in tetrahedral to octahedral site ratio between the different polymorphs is significant as local coordination environments have been shown to affect the core, semi-core and valence states in Ga_2O_3.[30] This leads to significant changes to the valence and conduction band density of states. This implies differences in the material's bandgap and conduction or valence band offset to other materials within a heterojunction, which has also been suggested by ab initio hybrid density functional theory calculations.[31] Thus, it is expected that different polymorphs of Ga_2O_3 have distinct electronic as well as structural properties, which would have unique effects on potential devices. A recent computational study also predicted a couple of new polymorph types with $P\overline{1}$ and $Pmc2_1$ space group structures, where the former was suggested to be only slightly less energetically stable than β-Ga_2O_3.[32]

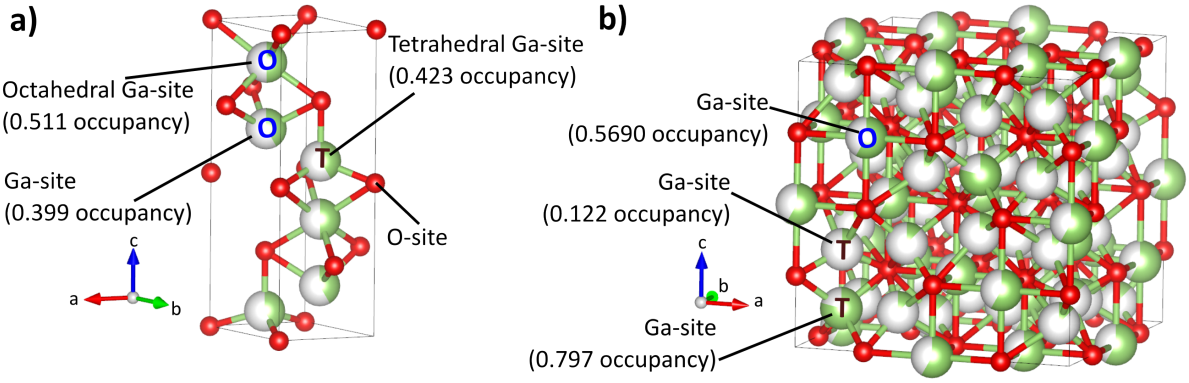

FIGURE 1.3. Visualisation of the unit cells of the **a)** ϵ and **b)** γ polymorphs of Ga_2O_3. The different types of Ga-ion site are labelled and coloured in green proportionally to their fractional occupancy.

If changes to the local coordination number of Ga-sites is expected to affect the electronic properties of Ga_2O_3, this well could extend to the properties of amorphous or polycrystalline samples depending on the process used for their production. It has been shown that different quantities of HCl flow during metal organic chemical vapour deposition (MOCVD) growth of gallium oxide films may produce different polymorphs, such as β, α and ϵ.[33] Despite the metastable nature of some of these structures, the tuneablility of gallium oxide electronic properties is within experimental reach. When considering how different phases of gallium oxide may function in potential devices, the majority of work has been based on ab initio density functional theory (DFT) calculations.[34] It should be noted that anisotropic material properties are not unique to the β phase of Ga_2O_3. Recent first principles calculations have suggested that the thermal conductivity in α-Ga_2O_3 is also anisotropic, ranging between 8.9 and 11.6 $Wm^{-1}K^{-1}$ along the $<001>$ and $<100>$ directions respectively.[35]

One reason for the interest in the κ polymorph of Ga_2O_3 is because of its spontaneous electrical polarisation.[36] Doping the material with In and Al has been shown to tune the κ polymorph's bandgap.[37] Its ferroelectric properties have also been investigated when grown onto a sapphire substrate.[38]

There is evidence that the structure of γ-Ga_2O_3 is locally reproduced at the boundaries between gallium oxide phases.[39][40] This was also experimentally observed, showing the appearance of the γ phase when annealing amorphous Ga_2O_3 material prior to the global relaxation into the β structure.[41]

1.3.1 Radiation damage and doping

Studying the radiation hardness and radiation-induced defects within materials is important to determine the lifetime of electronics in radiation environments such as for space or nuclear applications. The effects of various types of radiation on Ga_2O_3 have been examined in literature. Neutron damage in Ga_2O_3 has been shown to introduce defects, acting as electron traps. The irradiation was found to reduce the electrical conductivity, but increase thermoelectric power after an irradiation fluence of $10^{17}cm^{-2}$.[42] 1.5 MeV electron irradiation on Ga_2O_3 devices was shown to cause a reduction in carrier concentration, with a removal rate of 4.9 cm^{-1}[43] Proton damage on the same material using 10 MeV protons on the other hand was shown to remove carriers with a rate of 300 cm^{1-}.[44] Significant radiation hardness against gamma radiation has been suggested for Ga_2O_3, showing a tolerance as high as 1.6 MSy.[45]

The study of ion irradiation on Ga_2O_3, however, is of particular interest as it also relates to ion implantation and doping of the material. In Ga_2O_3, for example, it has been shown that implantation of compensating impurities helps suppress leakage current between Ga_2O_3 epitaxial layer and substrate.[46] Doping Ga_2O_3 can also be used to increase carrier mobility, shift the material band gap or obtain an n-type material.[47]

There are still a lot of unanswered questions when it comes to the effects of ion irradiataion/implantation on Ga_2O_3. A work by Wendler *et al.* investigated the irradiation effects of a set of different ion types - P, Ar and Sn on β-Ga_2O_3, found evidence of correlated displacement of lattice atoms that increases with ion fluence[48]. One possible explanation for this is the emergence of a different gallium oxide phase as a result of high doses of irradiation. Anber *et al.* looked at the diffraction patterns before and after 200 keV 7×10^{13} cm^{-2} Ge-ion implantation of β-Ga_2O_3. The pattern post irradiation was suggested to represent the [001] zone axis of κ-Ga_2O_3 as a deviation from the pre-implantation recorded pattern for the β-Ga_2O_3 [101] zone axis[49]. Similar observations were also made by Azarov *et al.*,, though the appearance of extra diffraction spots in the post-irradiation patterns remained unexplained in both papers[50]. Another recent paper by Kjeldby *et al.* shows how defect accumulation in β-Ga_2O_3 from Si-ion implantation results in the formation of a structure reminiscent of γ-Ga_2O_3.[51] If a polymorph transition resulting from irradiation could be confirmed, this would be important for potential devices as it has been shown that different polymorphs of gallium oxide have different radiation hardness, with surface damage accumulation rate being an order of magnitude larger for the β than for the α polymorph[52]. Thus, a polymorph transformation could affect the material's radiation hardness.

1.4 Thesis structure

The primary aim of the presented work is the investigation of key Ga_2O_3 properties, specifically as they relate to designing better Ga_2O_3-based electronic devices. This can be largely broken down into three main areas of research.

Due to the inherent downsides of Ga_2O_3 with regards to its low thermal conductivity and lack of p-type doping, integrating with other materials is paramount. We therefore investigate the different types/methods of adhesion for Ga_2O_3 onto higher thermal conductivity substrates. Chapter 2 is primarily dedicated on reviewing key literature related to the growth of commercial Ga_2O_3 substrates and the main methods used to incorporate Ga_2O_3 with other materials for the purpose of electronic devices. Some initial experiments carried out are also detailed there. This includes direct Van der Waals adhesion of (010) Ga_2O_3 onto a Si substrate with thermal oxide, hydrophilic bonding of (001) Ga_2O_3 onto Si (using amorphous Al_2O_3 as interlayer, and a brief discussion on the viability of growing diamond onto Ga_2O_3. In Chapter 3 we take a closer work into a method for depositing thin film Ga_2O_3 by means of liquid gallium passivation layer delamination. We also characterise the resulting deposition's structure, valence band alignment to the substrate (Si with thermal oxide), and its out-of-plane thermal conductivity.

We also explore the effects of anisotropy in Ga_2O_3 on the thermal transport across different Ga_2O_3-material interfaces. We use molecular dynamics simulations to model how the thermal conductivity of β-Ga_2O_3 changes with layer thickness along different crystallographic orientations. We estimate the thermal boundary resistances between different orientation β-Ga_2O_3 and (100) diamond (in a Van der Waals bonded interface). We also simulate thermal boundary resistances across β-Ga_2O_3-to-amorphous-Al_2O_3 and β-Ga_2O_3-to-amorphous-Ga_2O_3 ionically bonded interfaces. This work is detailed in Chapter 4. Examples of the molecular dynamics code used is given in Appendix A.1.

Finally, we investigate the structural changes in β-Ga_2O_3 under ion irradiation. In Chapter 5 we give the details of an in situ ion irradiation experiment on β-Ga_2O_3 and discuss the possible causes for crystal structure deformation at high doses of irradiation. We further explore the topic of ion irradiation damage on β-Ga_2O_3 in Chapter 6, where we present a cellular automaton model of the atomic displacements in the material as a function of ion irradiation dose. We also discuss the effects of ion irradiation energy on the types of defects produced, drawing comparisons with a follow-up ion irradiation experiment on β-Ga_2O_3. The code for the cellular automaton model is given in Appendix A.2. Chapter 7 provides a summary of all results outlined in this thesis.

1.5 Outcomes and future direction

While investigating the possible methods for adhesion of Ga_2O_3 to higher thermal conductivity substrates, we confirm that direct Van der Waals adhesion of β-Ga_2O_3 flakes is possible along multiple crystallographic orientations. The flakes that can be transferred however, tend to be limited in size. This type of bonding is also associated with higher thermal boundary resistances (TBR) across the interface. We have confirmed by means of molecular dynamics simulations that the TBR values across Van der Waals bonded β-Ga_2O_3 to (100) diamond can vary by up to 70% depending on the Ga_2O_3 crystallographic orientation. The lowest TBR value was estimated for the diamond interface with the (100) face of β-Ga_2O_3 - 48.6±0.3 m^2KGW^{-1}.

Our investigation of hydrophilic bonding between β-Ga_2O_3 and Si confirms that the method requires a high level of surface flatness in order to consistently provide results. By applying pressure to the bonding samples, we reduce the requirements on root-mean-squared surface roughness (from less than 0.5 nm to less than 2 nm). The use of an amorphous interlayer for bonding β-Ga_2O_3 to substrates such as diamond is also considered. Our molecular dynamics simulations suggest a TBR between β-Ga_2O_3 and amorphous Al_2O_3 to be within 0.9±0.3 m^2KGW^{-1} largely irrespective of the Ga_2O_3 crystal orientation. This implies that the TBR across a β-Ga_2O_3-diamond heterojunction (where the bond is realised through a 10 nm amorphous Al_2O_3 interlayer) could be at least 3.6 times lower than the TBR across the same junction where the bonding is realised through direct Van der Waals adhesion. We also briefly investigate the growth of pollycrystalline diamond on β-Ga_2O_3 substrate with a thin SiO_2 interlayer, confirming that significant spontaneous delamination of the grown diamond film makes that method impractical for the purpose of fabricating devices.

We examine thin film Ga_2O_3 deposition from oxidised liquid gallium surface layers. We demonstrate a large area deposition of thickness ranging between 8 and 30 nm on a Si substrate with thermal oxide (SiO_2). We measure the valence band offset across the Ga_2O_3-SiO_2 heterojunction, finding it to be 0.1 eV, implying a valence band offset of our thin film with respect to diamond as -2.3 eV. This suggests a 0.8 eV higher energetic barrier for minority carriers across a Ga_2O_3-diamond heterojunction, compared with pure β-Ga_2O_3. We further measure the out-of-plane thermal conductivity of our Ga_2O_3 film, finding it to be about 3±0.5 $Wm^{-1}K^{-1}$, which is higher than what has previously been achieved for polycrystalline films of comparable thickness.

A good future direction for research is into the thermal properties of other Ga_2O_3 polymorphs. To this end, molecular dynamics simulations similar to the ones presented in this thesis, could be used. Before this could be done, however, some density functional theory (DFT) simulations may be required in order to obtain working inter-atomic potentials that correctly model the structures and properties of the sought Ga_2O_3 polymorphs. In our work, without access to such potentials, we could only model the behaviours of β and amorphous Ga_2O_3. However, incorporating some further DFT work could be beneficial for the future development of this research.

Our molecular dynamics simulations confirm that the thermal transport through β-Ga_2O_3 layers is affected by the material's crystallographic orientation. We find that the change in thermal conductivity with increasing β-Ga_2O_3 thickness varies across crystallographic directions. We also simulate the TBR across β-Ga_2O_3 to amorphous Ga_2O_3 junctions, finding the TBR to vary with crystallographic orientation of the β-Ga_2O_3, estimated as of the order of and lower than the TBR between β-Ga_2O_3 and Al_2O_3.

From our investigation on the structural changes in β-Ga_2O_3 arising from in situ ion irradiation, we demonstrate that with increasing 200 keV Ar ion dose, a continuous anisotropic reduction in lattice dimensions takes place. Above a threshold irradiation dose (first observed at 2 displacements per atom (dpa)), extra reflections appear in the material's diffraction pattern. We attribute these to complex planar defects and reject the hypothesis that a polymorph transition occurs.

Our cellular automaton model of the ion irradiation process in β-Ga_2O_3 suggests a significant reduction in the average local Ga-ion coordination number, which may lead to changes in the electronic properties of the material. We also confirm that the types of defects ion irradiation induces in β-Ga_2O_3 strongly depend on the ion energy - with two main modes of defect formations at lower and higher incident ion energies, respectively. For instance, despite the large density of defects, we do not observe the same type of structural changes in β-Ga_2O_3 after high dose irradiation with 2 MeV Ar ions as we do after irradiation with 200 keV Ar ions.

The actual crossover energy between the two modes of defect formation is still not ascertained. Future research into the types of defects produced, and how their relative quantities vary for different ion irradiation energies, could be further explored. A valuable future addition to the currently presented research could be the development of reliable means of identifying different types of defects and dislocations, especially in materials with very high defect densities.

CHAPTER 2

GALLIUM OXIDE TO SUBSTRATE BONDING: REVIEW AND EXPERIMENTS

One way of addressing the low thermal conductivity in β-Ga_2O_3, when considering the material for use in power electronics, is to use it in tandem with another, high thermal conductivity material. In this chapter we examine some existing literature, looking at the types of Ga_2O_3 bulk substrates that are available, as well as some of the most common methods for adhering Ga_2O_3 to other materials. With regards to bulk substrates, we specifically focus on the crystallographic orientations available (which are important due to the material's inherent anisotropy), as well as the different types of doping. We then further examine the different methods for adhesion, outlining their benefits and shortcomings, as well providing some additional information from initial experiments carried out.

2.1 Gallium oxide substrates growth

β-Ga_2O_3 substrates are commercially grown using various from melt techniques. Here we briefly discuss the commonly used Czochralski method for β-Ga_2O_3 growth, a general diagram of which can be seen in Figure 2.1 **a)**. The process is carried within an induction furnace at the temperature of melting for β-Ga_2O_3 - 1820° C. Due to the high temperature, an iridium crucible is used to contain the melt, formed from high purity gallium oxide powder. A crystal seed is lowered to contact with the melt and then slowly pulled up as the crystal boule (cylindrical ingot) is formed. During the process the seed holder and the crucible are usually rotated in opposite directions to one another in order to facilitate a uniform boule formation. The crystal seed also dictates the growth direction of the β-Ga_2O_3. The $< 010 >$ growth direction is used for β-Ga_2O_3 as $< 100 >$ and $< 001 >$ oriented seeds are prone to easy cleaving and blistering.[53]

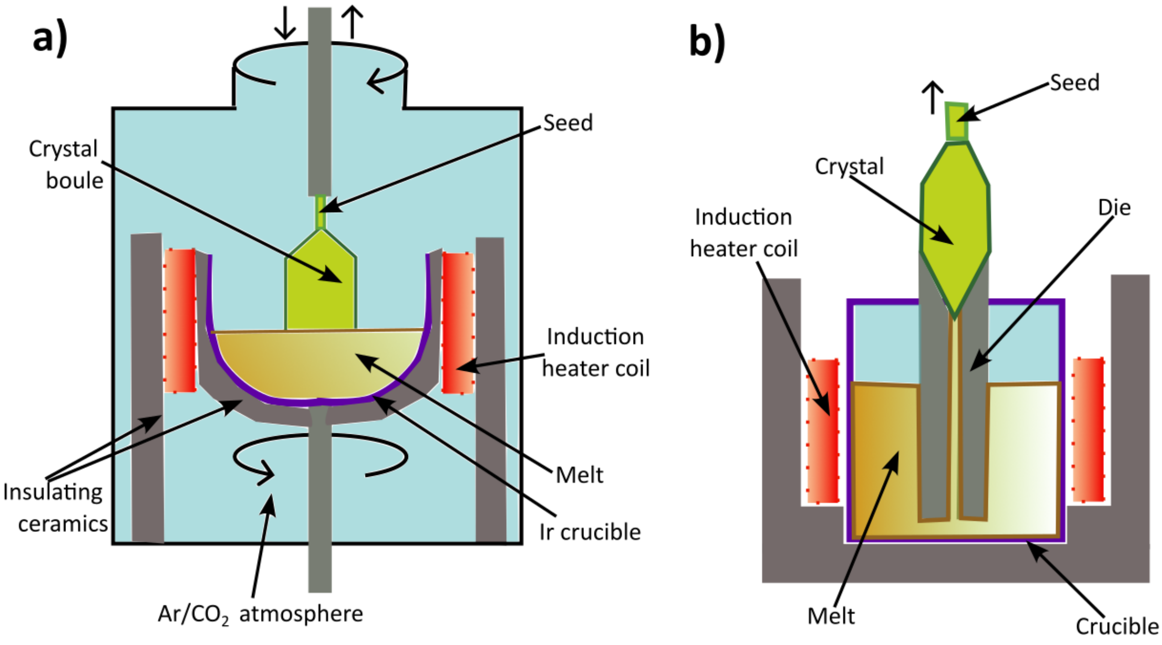

FIGURE 2.1. Diagram of **a)** Czochralski, and **b)** Edge-defined film-fed growth (EFG) method for bulk Ga_2O_3.

When using an iridium crucible, a low-oxygen environment is necessary in order to suppress crucible degradation from oxidation into IrO_2, as well as Ir-related defects in the grown β-Ga_2O_3. In a low-oxygen atmosphere and high temperature (such as the one required for the growth process), however, Ga_2O_3 can dissociate to GaO and Ga_2O. For suppression of these unwanted effects, one possible atmosphere consists of Ar/CO_2 in a 9:1 ratio. The oxygen partial pressure in such atmosphere increases with temperature due to the decomposition of CO_2, sufficient to stabilise Ga_3O_3 at its melting temperature, while remaining low enough in the temperature range where the iridium crucible is most sensitive to oxidation (1200 to 1400° C).[54]

β-Ga_2O_3 boules grown along the $< 010 >$ direction can be produced with sizes up to 50 mm in diameter (2 inches) and up to 35 mm in length.[55] Unfortunately, the poor thermal conductivity of β-Ga_2O_3 proves a limiting factor in the diameter of boules that can be grown using the Czochralski method.[56] β-Ga_2O_3 wafers of up to 6 inch diameter, however, have been demonstrated using another common from melt growth technique, known as Edge-defined film-fed growth (EFG), a diagram of which is shown in Figure 2.1 **b)**. What distinguishes EFG from Czochralski is that a die for producing the crystal shape is mounted in the crucible, allowing for the melt to be fed up through a slit in the die via capillary action.[57]

Once the bulk β-Ga_2O_3 boule is grown, wafers can be sawed and polished. The β-Ga_2O_3 substrates produced usually keep the growth orientation ($< 010 >$), however, commercial substrates

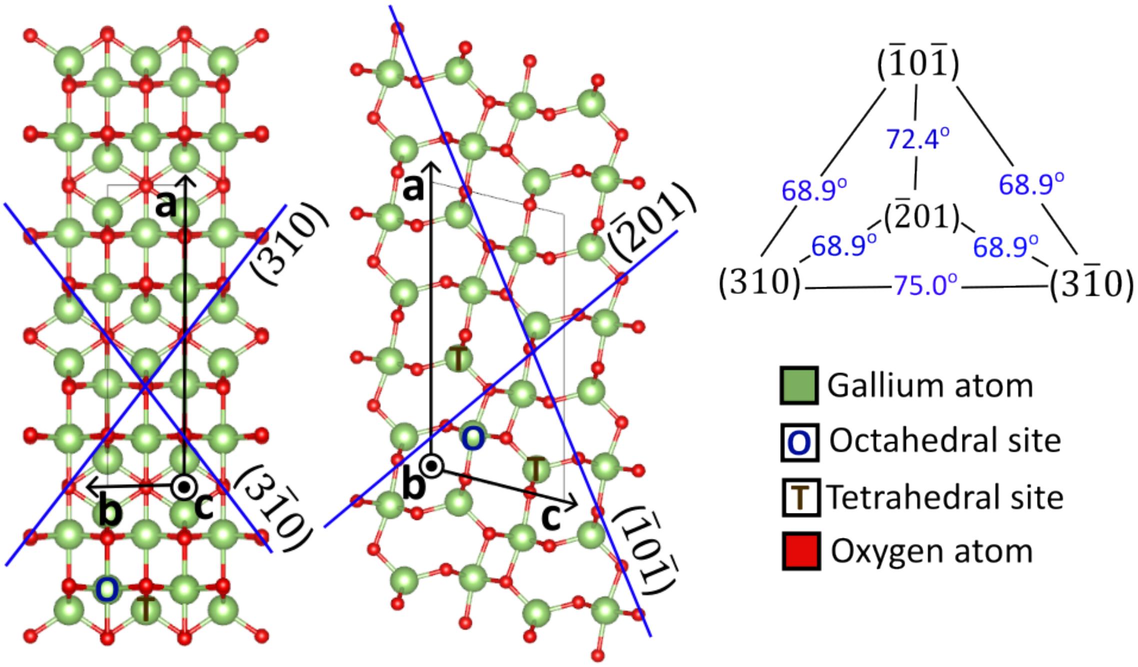

FIGURE 2.2. Diagram showing the near close packed planes in β-Ga_2O_3

are available also having been sawed to have the $<100>$, $<001>$ and $<\bar{2}01>$ orientations. ($\bar{2}$01) is significant as it is one of four near close packed β-Ga_2O_3 planes, and has been identified as a slip plane in the material.[58] The four near close packed β-Ga_2O_3 planes - ($\bar{2}$01), ($\bar{1}$0$\bar{1}$), (3$\bar{1}$0) and (310) form the faces of a distorted tetrahedron as illustrated in Figure 2.2.[59] The directional diversity of available β-Ga_2O_3 substrates is something that can be taken advantage of for the design of better and more efficient electronic devices.

β-Ga_2O_3 substrates can be unintentionally doped (UID), which normally involves the presence of Si and H impurities in the material. These unintentional dopants are known to enhance n-type conductivity in grown β-Ga_2O_3.[60] The grown boules can also be intentionally doped with a wide array of possible dopants depending on the desired properties of the β-Ga_2O_3 substrate.

Doping with donor impurities creates energy levels close to the material's conduction band. An electron within such donor level can then be excited to the conduction band, which can improve n-type conductivity. On the other hand, doping with acceptors creates energy levels close to the valence band. When electrons get excited into these acceptor levels, mobile holes are left in the valence band. A diagram of donor and acceptor levels within a material band gap can be seen in Figure 2.3. What is also important about these impurity levels, is how close they are to the conduction or valence bands respectively. If the energy needed to remove an electron/hole from the impurity level is significantly larger than k_BT, the characteristic thermal energy (K_b being the Boltzmann constant and T being temperature), these energy levels are referred to as deep

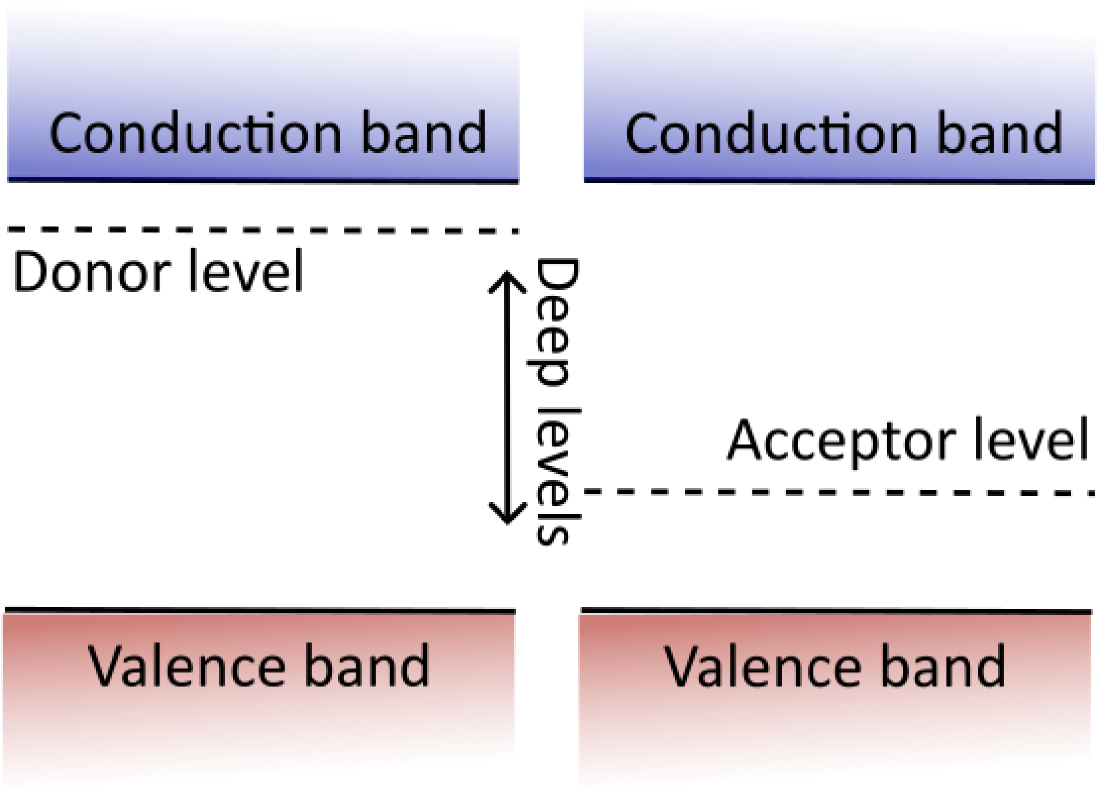

FIGURE 2.3. Diagram of donor and acceptor levels within a material band gap

level defects. For enhancing n or p-type conductivity in semiconductors, deep level defects are usually avoided in favour of more "shallow" dopant levels.

Si or Ge being substituted into tetrahedral Ga-sites act as a shallow donors in β-Ga_2O_3, with donor level energy with respect to the conduction band estimated to be around 30 meV.[47] Other shallow donors in β-Ga_2O_3 are Sn, substituted in octahedral Ga-sites, as well as Cl or F substituted in O-sites.[61] Part of the reason the use of p-type conductivity in β-Ga_2O_3 is impractical is the lack of suitable shallow acceptors. A recent work by Islam *et al.,* demonstrated p-type conductivity in β-Ga_2O_3 by hydrogen diffusion into gallium vacancy sites, however, the poor hole mobility resulting from the flat valence band of the material remains an issue.[62] Doping β-Ga_2O_3 with deep acceptor impurities can result in semi and highly insulating substrates. For this, most commonly Fe or Mg dopants are used, although other dopants, such as Co or Ni, as well as Ga or O vacancies within the material have been found to act as deep acceptors.[63]

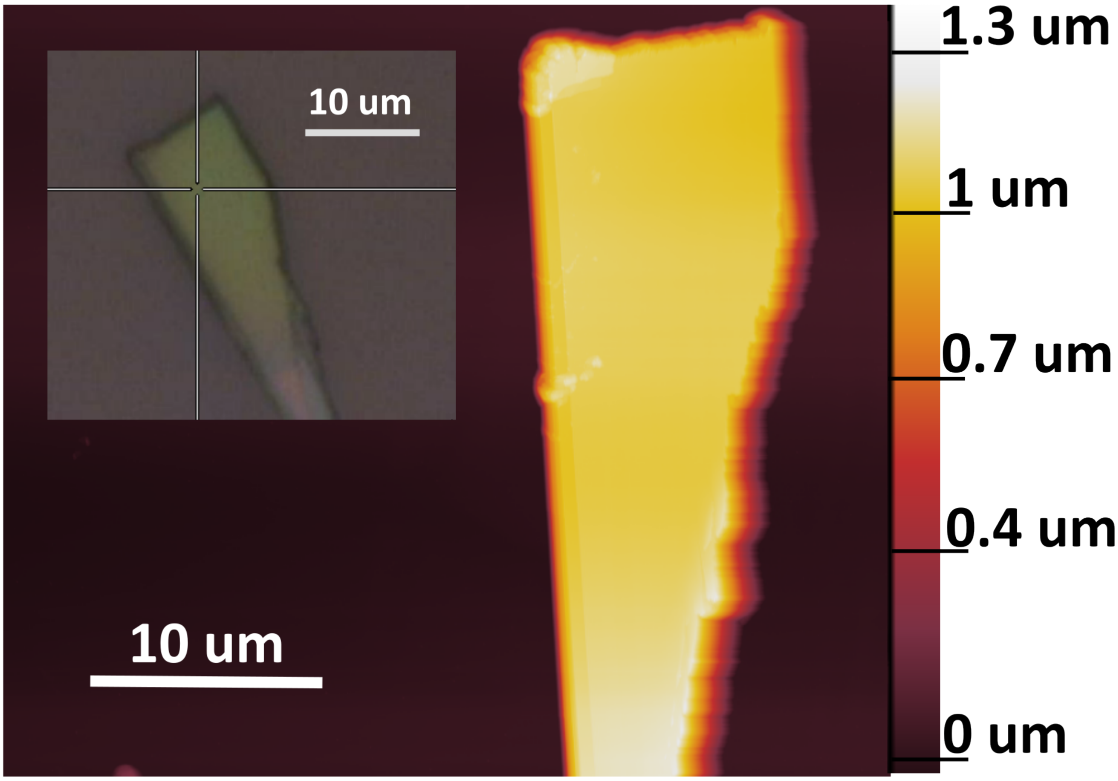

FIGURE 2.4. Atomic force microscope image of (010) β-Ga_2O_3 flake deposited onto silicon with thermal oxide, regular microscope image in inset.

2.2 Ga_2O_3 adhesion to other materials

2.2.1 Van der Waals adhesion

The (100) and (001) are easy cleavage planes for β-Ga_2O_3. Bae *et al.,* have demonstrated that large area flakes can be directly exfoliated from the bulk by use of regular adhesive tape and dry transferred onto a silicon with thermal oxide substrate. The resulting β-Ga_2O_3 deposition, a few hundred nm in thickness, is thus adhered to the substrate by weak Van der Waals forces.[64] Such transfer has also been demonstrated with ($\overline{2}01$) β-Ga_2O_3 onto a (100) single crystal diamond substrate. The resulting thermal boundary conductance (TBC) was estimated by Cheng *et al.,* to be about 17 $MWm^{-2}K^{-1}$, similar to the TBC across a lead on diamond interface, with the metal being physical-vapour deposited.[65] Molecular dynamics simulations of how the the crystallographic orientation of the β-Ga_2O_3 crystal would affect the thermal conductance (and thermal resistance) across a Van der Waals bonded β-Ga_2O_3 to (100) diamond interface, due to β-Ga_2O_3's inherent anisotropy, are presented in Chapter 4.

There are also downsides to the direct exfoliation method. While exfoliation from β-Ga_2O_3

faces other than the easy cleavage (100) and (001) planes is possible, the area of the resulting flakes can be quite limited. We have demonstrated β-Ga_2O_3 flake exfoliation using standard scotch tape from a (010) bulk substrate. An atomic force microscope (AFM) image of the flake, post direct transfer onto silicon with thermal oxide, can be seen in Figure 2.4. The flake is needle-like with a width of only about 10 microns and length less than 100 microns, which is also consistent with the sizes of flakes reported in literature exfoliated from other β-Ga_2O_3 faces.[64] The flake seen here is also fairly thick - about 1 micron in thickness. The thickness of the exfoliated flakes is also remarked on by Kwon *et al.,*, who find β-Ga_2O_3 flakes primarily over 200 nm thick. Therefore, ultra-thin (below 100 nm) β-Ga_2O_3 depositions from this method can only be consistently achieved via additional etching procedures.[66]

2.2.2 Direct bonding

Another method for direct bonding of β-Ga_2O_3 onto a diamond substrate has been proposed by Matsumae *et al.,*, relying on functionalising both material surfaces with OH groups. A schematic of the general procedure is shown in Figure 2.5. Once both material surfaces have been properly functionalised, the β-Ga_2O_3 and diamond may be brought into contact under ambient conditions. Finally, the bonding is realised through a thermal dehydration reaction at 250^{circ} over 24 hours. It is important to note that Matsumae *et al.,* observed a limited area of bonding in samples that were not left in desiccant for approximately 3 days prior to the annealing step.[67]

Surface functionalisation for β-Ga_2O_3 with OH-groups can be realised by treatment with oxygen plasma (200 W under 60 Pa for 30 s as performed by Matsumae *et al.,*). For the diamond surface, however, it has been shown that functionalising the surface with OH-group can be reliably achieved using cleaning in Piranha solution (H_2SO_4 mixed with H_2O_2 in a 4 to 1 ratio at 75° C for 10 min). Using this method, diamond has also successfully been hydrophilically bonded to a silicon with thermal oxide substrate.[68]

A p-n junction using p-doped single crystal (100) diamond and an n-type (100) β-Ga_2O_3 has recently been demonstrated using this method of bonding. However, in order for this bonding to be consistently reproducible, it should be noted that both surfaces need to have a root-mean-squared roughness less than 0.5 nm.[69] This implies that further polishing may be required in order for Ga_2O_3, SiC or diamond substrates to be reliably used for hydrophilic bonding. Furthermore, the surface roughness requirement is not viable for pollycrystalline diamond substrates, and relying on single crystal diamond for p-n devices of this type is unscaleable.

Other forms of direct bonding of materials usually rely on some form of interlayer in order to overcome issues related to surface roughness. For example, surface-activated bonding of β-Ga_2O_3 to SiC has been demonstrated with deposition of a thin film Al_2O_3 (via atomic layer deposition to serve as interlayer) on the Ga_2O_3 side, followed by bombardment on both surfaces with Ar ions in ultra-high vacuum. This process allows for the bonding between the two materials to occur spontaneously upon contact without the need for further thermal treatment.[70] This type

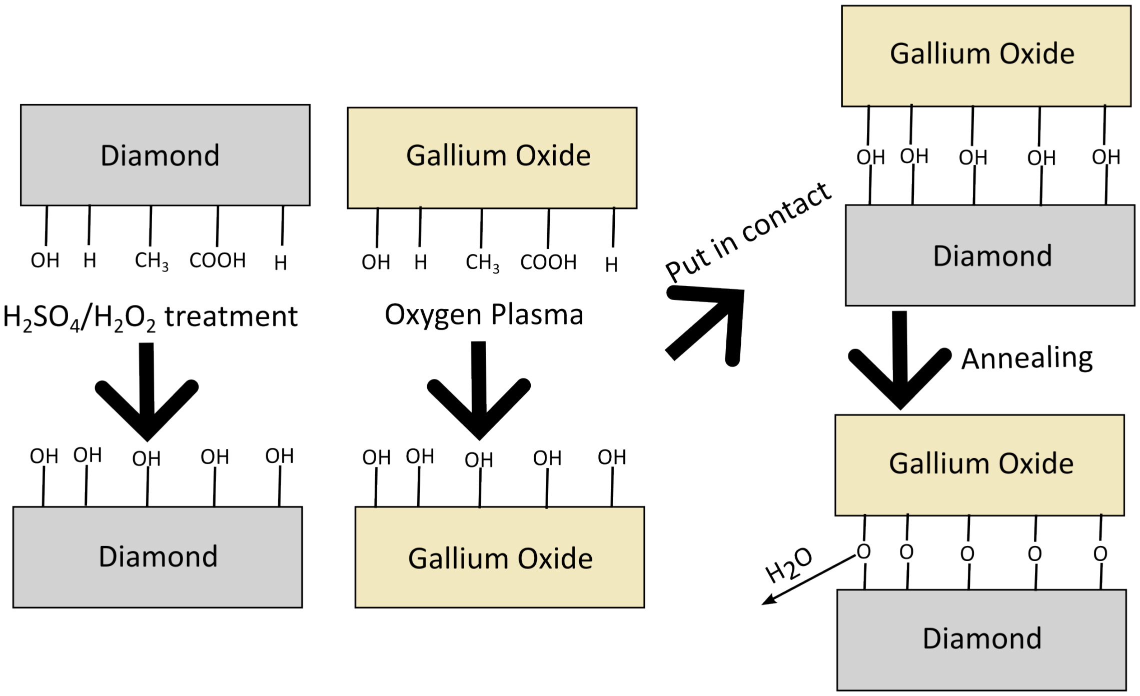
Diamond
OH H CH$_3$ COOH H
H$_2$SO$_4$/H$_2$O$_2$ treatment
OH OH OH OH OH
Diamond
Gallium Oxide
OH H CH$_3$ COOH H
Oxygen Plasma
OH OH OH OH OH
Gallium Oxide
Put in contact
Gallium Oxide
OH OH OH OH OH
Diamond
Annealing
Gallium Oxide
H2O
O O O O O
Diamond

FIGURE 2.5. Diagram of the method for direct hydrophilic bonding of gallium oxide to diamond.

of bonding is usually carried out with wafers or wafer dies, so the question of controlling the thickness of the bonded Ga_2O_3 naturally arises. This can be accomplished via H^+ implantation of the β-Ga_2O_3 wafer prior to bonding. By annealing at 450° (in N_2 for 6 hours) after the surface-activated bonding, a splitting of the β-Ga_2O_3 wafer across the plane of highest H^+ concentration occurs, leaving a layer of β-Ga_2O_3 bonded to SiC via a thin Al_2O_3 interlayer. The thickness of the bonded β-Ga_2O_3 layer can naturally be adjusted depending on the energy (and hence projected penetration depth) of the ion implantation. This method for wafer-cutting is known as Smartcut.[71] A benefit of this method is that it can be used to bond any orientation of β-Ga_2O_3 crystal, so long as a substrate with such orientation can be procured.

We performed initial direct bonding experiments, designing a bonding procedure that takes inspiration both from the work of Matsumae *et al.*,, as well as the use of Al_2O_3 as bonding interlayer. We sucessfully demonstrated bonding of 10×10 mm^2 n-type (Sn-doped) (001)-oriented Ga_2O_3 die to a 10×10 mm^2 (100) p-type Si die. Our modified version of the hydrophilic bonding method involves deposition of 20 nm of amorphous Al_2O_3 onto each of the two dies prior to bonding, deposited by means of atomic layer deposition (ALD). The bonding of the Ga_2O_3 to Si is then realised through the hydrophilic bonding of the two thin film amorphous Al_2O_3 layers to one another. Surface functionalisation of the Al_2O_3 surfaces was done using oxygen plasma, similarly to the process for a Ga_2O_3 surface. By doing this, we avoid any potential issues with

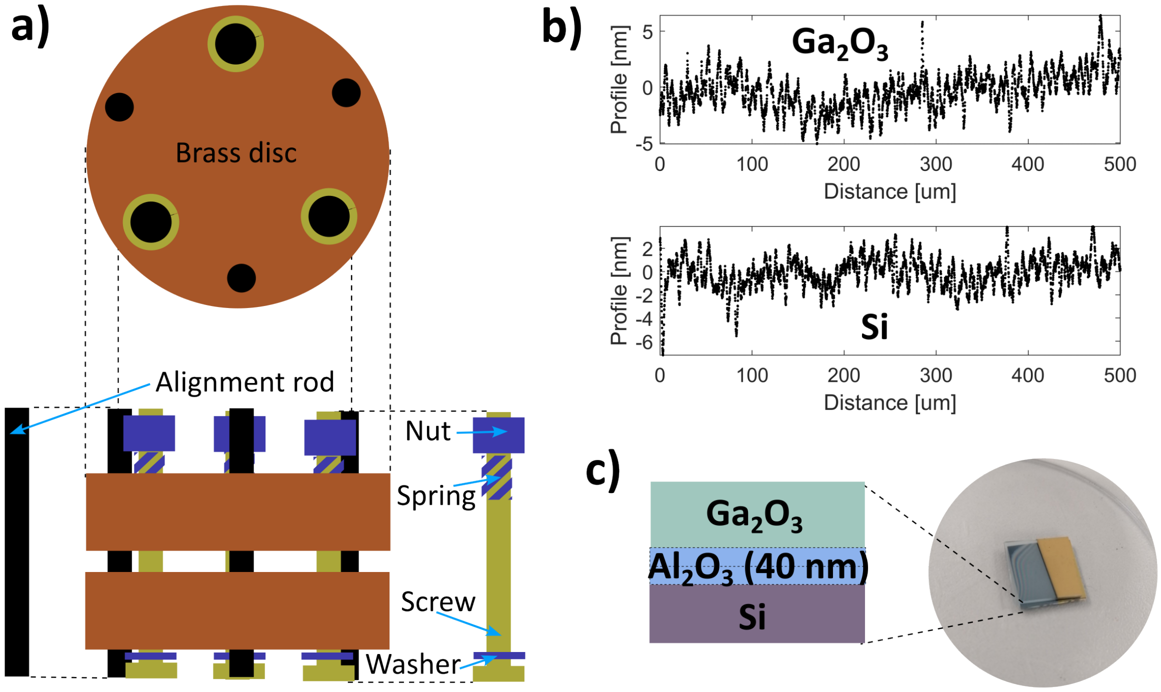

FIGURE 2.6. **a)** Diagram of the equipment used for applying pressure to samples for bonding, consisting of two brass discs, three alignment rods and three sets of screw, washer, spring and nut; **b)** Profiles across the surfaces of the two dies to be bonded - Ga_2O_3 and Si; **c)** Image of the sample post bonding, with diagram of the sample's layer composition. Some gold has been deposited on top of half the sample after the successful bonding.

lattice mismatching at the interface resulting in fewer bonds being formed. Using an amorphous interlayer allows for the outcome of the process to be consistent regardless of the crystal structure of the dies used to bond.

A remaining concern with using the hydrophilic bonding method is the requirement for ultra-flat surfaces. We further apply pressure on the dies during the bonding process in order to minimise issues with the bonding arising from bowing of the die surfaces or other surface imperfections. A diagram of the bonder used to apply pressure to the Ga_2O_3 and Si dies after they are placed in contact can be seen in Figure 2.6 **a)**. The bonder consists of two brass discs, ~5 cm in diameter, each having six holes. After the ALD deposition of 20 nm Al_2O_3 on both Ga_2O_3 and Si surfaces, followed by the functionalisation with O_2 plasma, the dies are put into contact and then placed in the centre of one of the discs. The second disc is then lowered on top of the bonding samples, using three alignment rods, so as to minimise any disturbance to the dies. Screws are used to tighten the two discs together, applying the pressure to the bonding samples. Springs of known force constant (11 Nmm^{-1}) were placed before the nuts to make sure the tightening of the screws was done consistently. Thus, a compression of the springs by about 2 mm corresponds to an approximate pressure applied to the bonding samples of around 30 kPa. The sample is kept in a desiccator for approximately 3 days (as outlined in the process by Matsumae *et al.,*) and then annealed for 24 h at 250° with the pressure from the bonder being consistently applied during the entire procedure. Finally, the successfully bonded sample is removed from the bonder.

Figure 2.6 **b)** shows the surface profiles over a distance of 0.5 mm of both Ga_2O_3 and Si dies prior to the bonding, taken using a profilometer. From these, we can estimate the root mean squared (RMS) roughness of the dies as approximately 1.3 nm for the Si, and 1.7 nm for the Ga_2O_3. While both surfaces are polished, they do not fulfill the condition as expressed by Matsumae *et al.,* of having RMS roughness below 0.5 nm. This indicates that the use of pressure when performing hydrophilic bonding can overcome some of the method's limitations arising from surface roughness. An image of the bonded sample - 10×10 mm^2 Ga_2O_3 on 10×10 mm^2 Si with 40 nm Al_2O_3 interlayer can be seen in Figure 2.6 **c)**. Some faint contours can be seen along the edges of the sample, indicating the bonding is not uniform throughout.

Our initial bonding experiments show that the hydrophilic bond method can be consistently used regardless of the crystal structure of the dies used. Applying pressure on the samples can help lower the requirements on surface roughness for successful bonding (from less than 0.5 nm to less than 2 nm RMS roughness). However, issues with surface bowing or other imperfections may still affect the success of bonding. Due to their higher surface roughness, polycrystalline substrates, such as diamond, are still not viable for bonding using this method.

2.2.3 Epitaxial growth

Another way of integrating Ga_2O_3 films onto other materials is by epitaxially growing Ga_2O_3 thin films. Since single crystal substrates exist only for the β phase of Ga_2O_3, this is also a means of incorporating other Ga_2O_3 polymorphs into device architectures. Many different methods for epitaxial growth of thin film Ga_2O_3 exist, such as pulsed layer deposition (PLD), metal organic chemical vapour deposition (MOCVD), atomic layer deposition (ALD) and more. Growth of most Ga_2O_3 polymorphs - α, β, ϵ and κ has been demonstrated using MOCVD, while the γ polymorph has primarily been grown via PLD (also demonstrated to work for β and κ).[72]

PLD works by directing laser pulses at a material target in order to direct material plasma from said target onto a substrate. Laser energy, growth temperature and pressure are important parameters for this method that affect the quality of crystals grown. Yadav *et al.,* examined the effects of annealing on the band alignment of PLD-grown polycrystalline β-Ga_2O_3 onto a (100) Si substrate. They observed that the valence band offset of the grown film with respect to the silicon substrate changed from -3.35 eV (for the thin film as deposited) to -3.55 eV after annealing at 600°.[73]

MOCVD works by introducing precursor gases into a reactor, containing a substrate wafer, at high temperature and low pressure. The gases undergo chemical decomposition and their subspecies get absorbed onto the substrate surface. For Ga_2O_3 the precursor gases used are generally either trimethylgallium ($Ga(CH_3)_3$) or triethylgallium ($Ga(C_2H_5)_3$), as well as O_2. Chen *et al.,* found that it is possible to grow different phases of Ga_2O_3, using $Ga(CH_3)_3$ and O_2 in Ar as precursors at 600° temperature and 45 Torr pressure, by introducing different gas flow rates of HCl. At up to 5 sccm of HCl flow, the growth was identified using x-ray diffraction to consist purely of β-Ga_2O_3. Increasing the HCl flow further was shown to grow both β and ϵ polymorphs, up to a flow rate of 30 sccm, at which point the growth was identified as entirely ϵ-Ga_2O_3. With a HCl flow rate of 60 sccm, on the other hand, the deposition was identified as primarily α-Ga_2O_3.[33] Lee *et al.,* have further demonstrated MOCVD growth of κ-Ga_2O_3 onto a sapphire substrate that remained structurally stable even after high temperature annealing at 1000°.[74]

Growing Ga_2O_3 using ALD also makes use of $Ga(CH_3)_3$ as a precursor as well as of oxygen plasma (at 8 mTorr pressure) within a reactor at about 300°. What distinguishes ALD is that the precursors are introduced in a sequence of pulses, so that after each step the reaction between the precursors is self-limiting, resulting in a single atomic layer. Because of this, ALD can be used to achieve superior film thickness control over a large area. A recent work by Cheng *et al.,* demonstrated polycrystalline β-Ga_2O_3 film growth onto (100) diamond substrate. The thermal boundary resistance between the ALD-deposited Ga_2O_3 and the diamond was estimated to be 10 times smaller than that between Van der Waals bonded β-Ga_2O_3 and diamond, reaching as low as 5.6 m^2KGW^{-1}. The thermal conductivity of the Ga_2O_3 film at about 30 nm thickness, however, was measured to be fairly low - about 1.5 $Wm^{-1}K^{-1}$.[75] In Chapter 3 we explore an alternative method for thin film Ga_2O_3 deposition that does not rely on epitaxial growth, while the measured out-of-plane thermal conductivity for our polycrystalline film is double that achieved by Cheng *et al.,* for the same film thickness.

2.2.4 Diamond growth on Ga_2O_3

Another option for integrating β-Ga_2O_3 with diamond is to perform diamond growth on the Ga_2O_3 itself. Growth of diamond relies on a CH_4/H_2 gas (usually 3% or 5%) at high temperature and low pressure (usually about 630° with 50 Torr chamber pressure and 3.7 kW microwave power). Commonly, however, heteroepitaxial growth of diamond results in only a few isolated diamond islands rather than a continuous film. Because of this, substrates prepared for diamond growth are treated in an ultrasonic bath in an aqueous mixture containing nanodiamonds (crystallite size of approximately 5 nm) for about 30 mins. The nanodiamonds that remain on the substrate surface then act as seeds during the growth process, allowing for a continuous diamond film to be grown.[76] Another issue that can occur during diamond growth is damage to the substrate resulting from the hydrogen plasma. When growing on $(\bar{2}01)$ β-Ga_2O_3, Mandal *et al.,* found that this issue could be mitigated by first depositing ~90 nm of SiO_2 as a buffer layer onto the β-Ga_2O_3.[77]

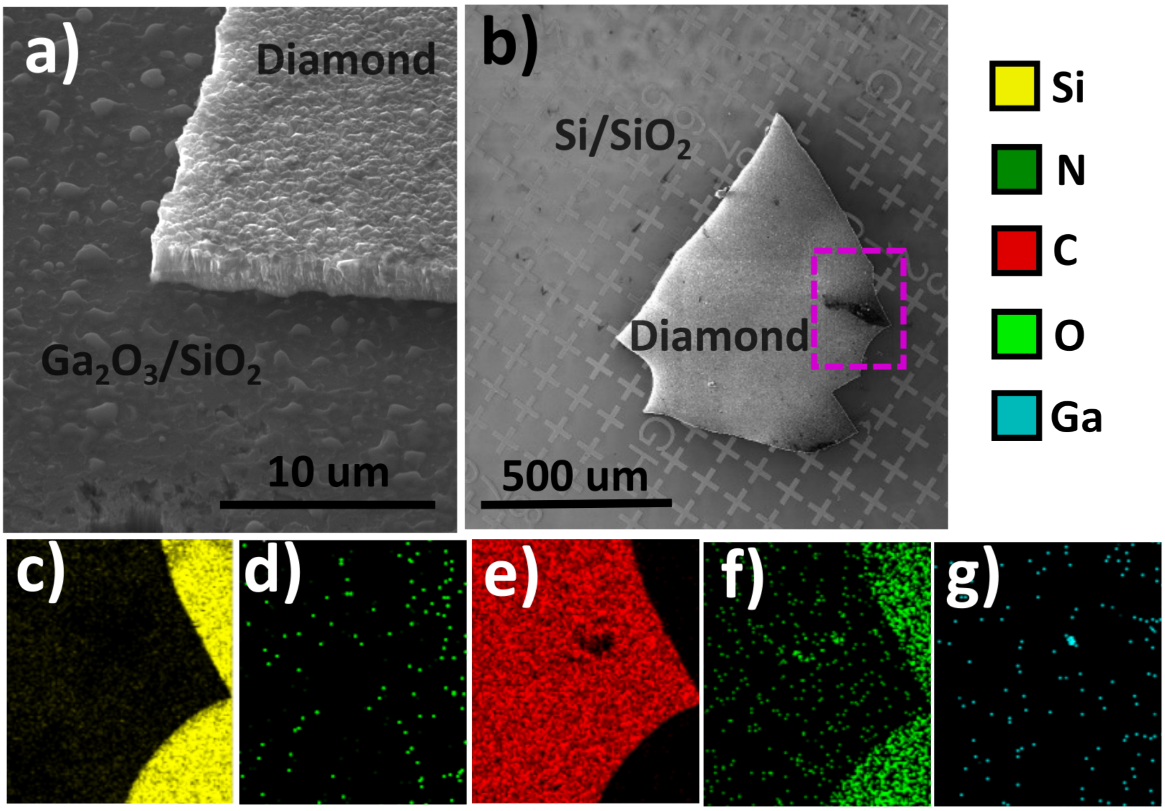

FIGURE 2.7. SEM image of **a)** diamond film grown onto β-Ga_2O_3 with SiO_2 interlayer, image tilted at 45° with respect to surface, and **b)** delaminated diamond film flake placed onto a marked Si/SiO_2 substrate. The marked rectangle denotes area on which EDX analysis was carried out. Si, N, C, O and Ga element analysis of the area can be seen in plots **c)**-**g)**.

We performed analysis on one such sample - diamond grown onto $(\bar{2}01)$ β-Ga_2O_3 with an SiO_2 interlayer, prepared at the University of Cardiff. Figure 2.7 **a)** shows a scanning electron microscope (SEM) image taken at a 45° tilt with respect to the sample's surface. The image clearly shows the edge of a piece of diamond film, indicating the substrate is not uniformly covered by the deposition. This is because the grown diamond film spontaneously delaminates off the sample. In order to further investigate the nature of the delamination occurring, we selected a small piece of delaminated diamond film and transferred it on a marked Si wafer with thermal oxide. An SEM image of the examined diamond flake can be seen in Figure 2.7 **b)**.

We used energy-dispersive x-ray spectroscopy (EDX) in order to investigate the elemental makeup of the delaminated diamond flake and confirm whether the diamond film remains attached to a β-Ga_2O_3 or SiO_2 layer post delaminating. EDX works by detecting the x-rays emitted by inter-shell electron transitions, excited by the SEM's electron beam. These x-rays are characteristic for different elements, and can thus be easily assigned to the presence of a particular atomic species at a penetration depth of up to a couple of microns when using a 20 keV electron beam. We chose a rectangular area at the corner of the diamond flake for EDX analysis - as marked in Figure 2.7 **b)**. The received signal for each of the Si, N, C, O and Ga atomic species within that rectangular area is shown in the Figure 2.7 plots **c)**, **d)**, **e)**, **f)** and **g)** respectively. In the Ga EDX signal we can distinguish a single clump of Ga-atoms, which likely represents a small piece of Ga_2O_3, as a comparable clump of O-atoms can also be seen in the same area within the oxygen signal. However, apart from that one isolated spot,the Ga EDX signal is fairly uniform within the chosen area, both on and off of the diamond flake. It is also similar in intensity to the N signal, which should be considered as negligible. Thus we can conclude that there is no large area Ga_2O_3 lifted off together with the delaminated diamond film. This shows that the adhesion of the grown diamond to the substrate is not strong enough to also lift off a gallium oxide layer when delaminating. While growth of diamond onto β-Ga_2O_3 has been achieved using an SiO_2 buffer layer, the spontaneous delamination of the diamond film with few traces of attached Ga_2O_3 shows that this is not an effective method for creating a good Ga_2O_3-diamond interface for use in devices.

2.3 Summary

Bulk β-Ga_2O_3 substrates can be grown from the melt, producing commercial substrates as large as 6 inch wafers. While the growth direction is primarily $< 010 >$, due to the existence of easy cleave planes in the material, (100), (001) and $(\bar{2}01)$-oriented substrates are also currently commercially available. Substrates can be unintentionally n-type doped, intentionally n-type doped, or implanted with deep acceptors, making the substrate semi-insulating.

Delamination of thin films from bulk β-Ga_2O_3 along easy cleave planes is a viable strategy for integrating β-Ga_2O_3 with other materials for the purpose of devices. However, these depositions are usually needle-like, with a width of up to 20 microns. Tuning of these flakes' thickness usually also requires further etching. While direct adhesion of the delaminated flakes onto a substrate using Van der Waals forces is easy to perform, it also involves a relatively high thermal boundary resistance across the interface. The thermal transport across Van der Waals bonded β-Ga_2O_3-diamond interfaces is further explored in Chapter 4. Other forms of direct bonding usually require some form of interlayer between the Ga_2O_3 and the high thermal conductivity substrate. A notable exception is direct hydrophilic bonding, which unfortunately relies on low RMS roughness for both surfaces, and thus has limited applicability. We find that applying pressure to the bonding samples can alleviate the requirement on RMS surface roughness (from lower than 0.5 to lower than 2 nm), however, this still currently excludes materials such as polycrystalline diamond from bonding using said method.

Ga_2O_3 may also be epitaxially grown on substrates. This is the main way other Ga_2O_3

polymorphs can be integrated for use in devices as bulk substrates for them are not currently available. Grown Ga_2O_3 films can also be polycrystalline. Epitaxial growth is also preferable to Van der Waals adhesion as it tends to result in lower thermal boundary resistance between the Ga_2O_3 and the chosen substrate. We examine the possibility of growing diamond on β-Ga_2O_3 and conclude that it is not a viable means of integrating the two materials for the purpose of device fabrication. Other methods for achieving adhesion between Ga_2O_3 (including thin films) and other materials can exist, one of which is detailed and explored in Chapter 3.

CHAPTER

3

ELECTRICAL AND THERMAL CHARACTERISATION OF LIQUID METAL THIN FILM GA_2O_3-SIO_2 HETEROSTRUCTURES

We discussed in Chapters 1 and 2 how heterostructures of Ga_2O_3 with other materials such as Si, SiC or diamond, are a possible way of addressing the low thermal conductivity and lack of p-type doping of Ga_2O_3 for device applications, as well as of improving device reliability. In this chapter we examine the electrical and thermal properties of Ga_2O_3-SiO_2 heterostructures, produced through thin film Ga_2O_3 deposition on a Si with thermal oxide substrate by means of oxidised liquid gallium layer delamination. We include details of x-ray photoelectron spectroscopy and transient thermoreflectance experiments. We report on the valence band offset of the Ga_2O_3 film deposited via this method to the substrate, as well as its out-of-plane thermal conductivity. This chapter is based on the author's publication, published in *Scientific Reports*.[78]

3.1 Introduction

In Chapter 1 we outlined some of the main pros and cons of gallium oxide with regards to the material's potential for applications in power electronics. The listed benefits included β-Ga_2O_3's high predicted breakdown field (8 $MVcm^{-1}$[2]), notably higher than the values of 2.6 $MVcm^{-1}$ for SiC and 3.3 $MVcm^{-1}$ for GaN,[3] as well as the availability of low-cost bulk substrates, which was then further elaborated on in Chapter 2. A main downside associated with the material is its relatively low (and anisotropic) thermal conductivity, ranging between 11 $Wm^{-1}K^{-1}$ and 27 $Wm^{-1}K^{-1}$ depending on crystallographic direction.[16] The thermal conductivities of SiC and GaN, on the other hand, are much higher, 420 $Wm^{-1}K^{-1}$ and 160 $Wm^{-1}K^{-1}$ respectively.[17] For a potential device, low semiconductor thermal conductivity may cause poor thermal dissipation under operation, which could end in device failure.

Integrating Ga_2O_3 with a high thermal conductivity substrate is an attractive potential solution to this issue. This way, another inherent downside of the material could be overcome, namely Ga_2O_3's poor hole mobility and consequent lack of practical bipolar or p-type devices. A p-n junction can be realised using an n-type Ga_2O_3 with a p-type material. An example of such a device being realised can be seen in the work by Li *et al.,* demonstrating self-powered photodetectors using n-type β-Ga_2O_3 and p-type GaN.[21] There has also been interest in realising a Ga_2O_3-diamond p-n superjunction, modelling of which has estimated an approximate 60% reduction in temperature rise under operation.[22]

Fabrication of thin film Ga_2O_3 has also attracted attention, specifically due to potential applications of the material in gas sensing,[12] solar cells for water-splitting[13] as well as wearable electronics.[14]. As discussed in Chapter 2, a primary way for adhesion of Ga_2O_3 to a substrate (specifically thin film Ga_2O_3) is epitaxial growth. In this Chapter, however, we aim to examine a simpler and more cost-effective method for depositing thin film Ga_2O_3 onto different substrates - relying on the spontaneous oxidation of liquid gallium in air. To characterise the emerging heterojunction between the deposition and substrate, one should examine both the thermal transport across the interface, as well as the band alignment across the junction. The latter is especially relevant for p-n or other vertical devices. Furthermore, we know that local changes in the coordination environments (inhomogeneities) of Ga_2O_3 can lead to shifts in core and valence energy states.[79] This is also evident from the reported variety in valence band offsets between different Ga_2O_3 polymorphs and Si - ranging from -2.9 eV (for ϵ-Ga_2O_3) to -3.7 eV (for κ-Ga_2O_3).[31] Because of this, we may expect different electronic properties from different amorphous/polycrystalline Ga_2O_3 samples, such as the one examined here.

Here we investigate the electrical and thermal properties of a Ga_2O_3-based heterointerface, realised through deposition of thin films of Ga_2O_3 onto silicon with thermal oxide. The deposition method used is based on the exfoliation of thin-film gallium oxide from liquid gallium - a recently proposed technique to realise 2D metal oxides.[80] Silicon has a thermal conductivity of about 130 $Wm^{-1}K^{-1}$,[81] significantly higher than Ga_2O_3 and so is a potential material for thermal management of Ga_2O_3-based devices. We obtain values for the valence band offset of the deposited gallium oxide with SiO_2, its out-of-plane thermal conductivity and thermal boundary resistance to the silicon substrate. This data can also be used predictively to assess the thin-film gallium oxide viability for use in tandem with other high thermal conductivity substrates, such as diamond.

3.2 Methods

3.2.1 Thin film deposition from liquid gallium

Pure gallium has a melting point slightly above room temperature - at 29°C. When exposed to air, the surface of the liquid metal is spontaneously oxidised due to a low Gibbs Free Energy for the

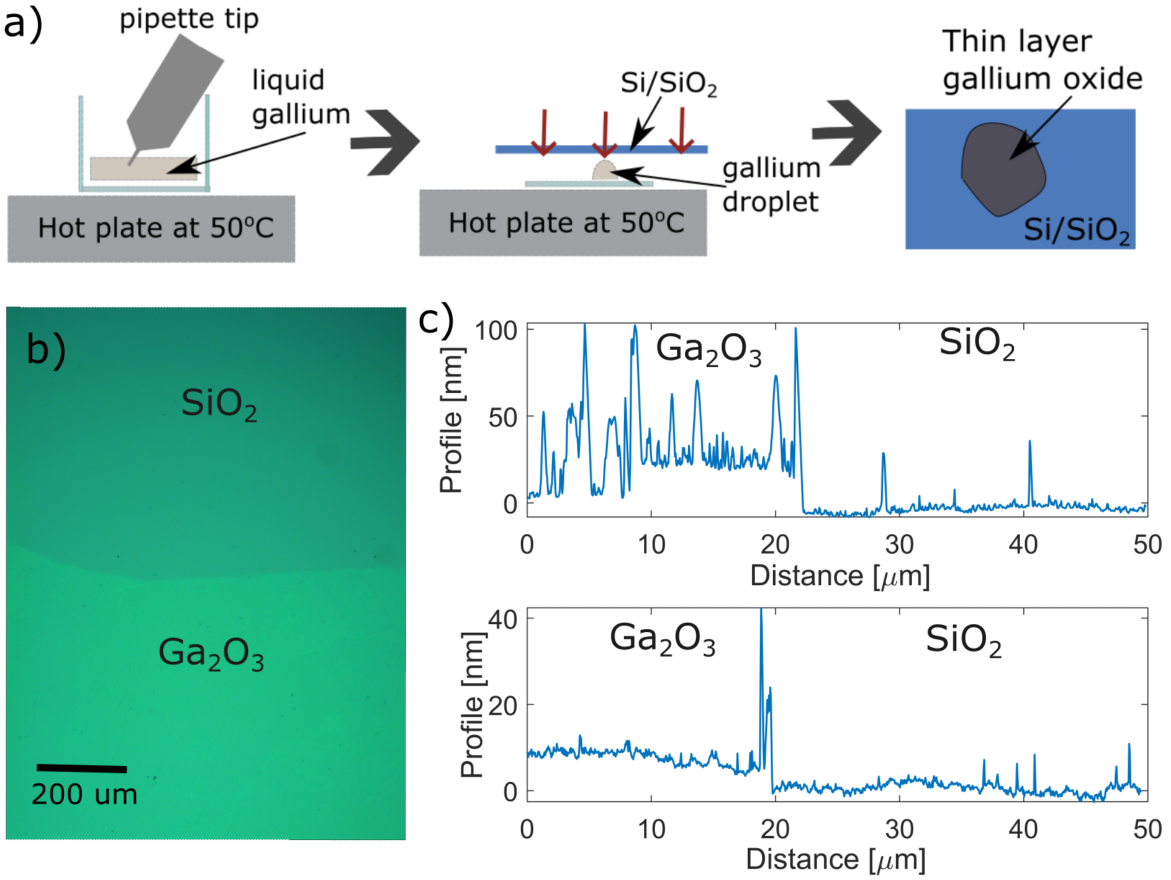

Figure 3.1: **a)** Schematic of the exfoliation method - a liquid gallium droplet is isolated and its passivation oxide is directly transferred onto a substrate. **b)** Microscope image of the Ga_2O_3 film deposited on thermally oxidised Si substrate after annealing at 250°C for 1 hour. **c)** Atomic Force Microscopy linescans taken across thin film oxide to substrate edges in two different areas.

formation of Ga_2O_3.[82] This passivating oxide layer is up to a few nanometres thick and with a large chemical potential gradient at the interface between the liquid core and oxide layer.[83] Because of this van der Waals forces have been found sufficient to detach this oxide layer from the bulk and adhere it to a separate substrate.[84] A gallium pellet is taken and heated on a hot plate to 50°C, i.e. above its melting temperature. A pipette tip is then used to pick up a liquid gallium droplet, which is in turn placed on a glass slide, kept in liquid form on the hot plate. The thin film of Ga_2O_3 or oxide skin is then put in contact with a B-doped Si substrate with thermal oxide, resulting in large area transfer of Ga_2O_3 film, as illustrated in Figure 3.1 **a)**. Excess gallium is cleaned off by rinsing the sample in heated ethanol. The sample is then annealed in oxygen at 250° C for 1 hour. This step has been suggested to aid in stabilising the stoichimometry of the deposited Ga_2O_3 film.[80] A microscope image of the layer post annealing is shown in Figure 3.1 **b)**; the boundary between the substrate and thin-film oxide is evident. An Agilent 5420 Atomic force microscope (AFM) was used in tapping mode, confirming that the layers prepared had a thickness ranging from 8 to 30 nm, shown in Figure 3.1 **c)**. The extracted profile for a thicker sample is visibly uneven. This is likely due to an overlapping of several oxidation layers.

There is some uncertainty relating to the exact structure of the deposited thin film. High resolution transmission electron microscopy (HRTEM) characterisation on films deposited under identical conditions (by Lin *et al.,*) have identified the resulting structure as polycrystalline β-Ga_2O_3, which is the assumption that is carried forward in this chapter.[84] However, further discussions, such as pertaining to domain size, orientation or crystallite quality, have not been made. We should note here that our attempts to directly characterise the deposited thin film have been so far unsuccessful. Prepared and annealed samples were probed using x-ray diffraction (XRD), grazing incidence x-ray diffraction (GIXRD) and electron back-scatter diffraction (EBSD). While these techniques are notable for extracting crystallographic information, our samples consistently produced no detectable signal in all three cases. The thin film nature of our deposition is certainly a limiting factor for signal amplitude, however, we expect other issues are also significantly contributing to the lack of visible signal from any of the three methods. It is possible that the crystallites in the film are of poor quality (large defect density) or are small and poorly aligned. Further in this chapter there is some limited speculation on the possible nature of the film's structure based on the band alignment and thermal conductivity measurement results. However, confirmation of the film structure cannot be made without significant further study. It should be noted that we reject the hypothesis that the film is either not gallium oxide or not crystalline. Our results from x-ray photoelectron spectroscopy (discussed in detail later in this chapter) confirm we are indeed observing gallium oxide. Similarly, our thermal conductivity results for the thin film are incompatible with an assumption of an amorphous structure. These points will be elaborated on later in this chapter.

3.2.2 X-ray photoelectron spectroscopy

High resolution x-ray photoelectron spectroscopy (XPS) was used to measure the valence band alignment of the Ga_2O_3 film to the substrate using a monochromatic Al kα ($h\nu$ = 1486.7 eV) excitation source with a pass energy of 50 eV. A diagram of the XPS setup is given in Figure 3.2. The x-rays incident on the sample in ultra high vacuum have enough energy to eject photoelectrons from atoms near the material's surface. Upon entering the hemispherical energy analyser, the photoelectrons are slowed down, so that their mean kinetic energy is equal to the pass energy. As they travel, they are energetically separated by a voltage applied across the hemispheres (with higher energy electrons having an increased path length through the analyser), and are finally detected.[85] From the kinetic energy E_K of the detected photoelectrons, we can obtain information about the ejected electrons' binding energies E_B within the atoms as $E_K = h\nu - (E_B + \phi)$, where ϕ is the work function of the sample. This way we obtain information about the energetics of core levels, as well as the valence band maximum of an investigated sample. The valence band

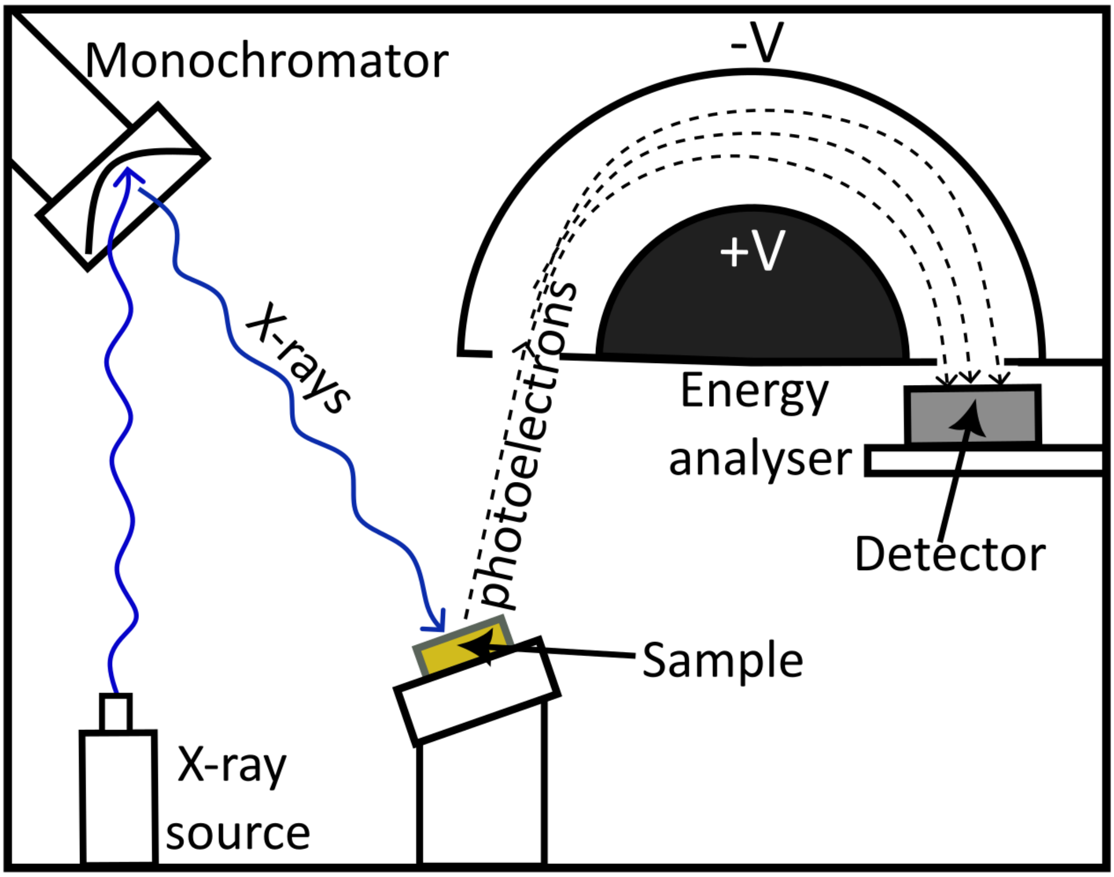

Figure 3.2: Diagram of the experimental setup for x-ray photoelectron spectroscopy.

offset of Ga_2O_3 with respect to SiO_2 is given as[86]

$$\Delta E_V = (E_{Ga3d}^{Ga_2O_3} - E_V^{Ga_2O_3}) - (E_{Si2p}^{SiO_2} - E_V^{SiO_2}) - (E_{Ga3d}^{Ga_2O_3-SiO_2} - E_{Si2p}^{Ga_2O_3-SiO_2}), \tag{3.1}$$

where $E_V^{Ga_2O_3}$ and $E_V^{SiO_2}$ denote the valence band energies for the two materials - Ga_2O_3 and SiO_2, respectively, $E_{Si2p}^{SiO_2}$ and $E_{Ga3d}^{Ga_2O_3}$ denote the energies of the core levels Si 2p and Ga 3d in the spectra taken solely from SiO_2 and Ga_2O_3, respectively, while $E_{Ga3d}^{Ga_2O_3-SiO_2}$ and $E_{Si2p}^{Ga_2O_3-SiO_2}$ denote the the energies of the two core levels as measured across the Ga_2O_3-SiO_2 interface. XPS has a low probing depth that rarely exceeds few tens of nanometres, however, due to the thin film nature of the gallium oxide deposition, any measurement taken from the Ga_2O_3 film is expected to probe through the interface and into the SiO_2 layer. Because of this, values for $E_V^{Ga_2O_3}$ and $E_{Ga3d}^{Ga_2O_3}$ cannot be reliably determined from our data, and a standard value for the term $E_{Ga3d}^{Ga_2O_3}$-$E_V^{Ga_2O_3}$=17 eV is used instead.[87] For measurements, an area on the sample with gallium oxide deposition of 8 nm thickness was chosen, from which $E_{Ga3d}^{Ga_2O_3-SiO_2}$ and $E_{Si2p}^{Ga_2O_3-SiO_2}$

data was extracted. An area on the sample without deposition was also chosen for the estimation of $E_V^{SiO_2}$ and $E_{Si2p}^{Ga_2O_3-SiO_2}$.[88] The peak positions for Ga 3d and Si 2p were estimated from the data via Gaussian fitting.

3.2.3 Transient thermoreflectance

In order to measure the out-of-plane thermal conductivity of the Ga_2O_3, transient thermoreflectance (TTR) was used. This technique relies on the temperature dependence of a material's refractive index. Over small changes in temperature, the dependence of refractive index on temperature can be considered linear.[89] This also results in a change in the material's reflectivity R, which for linearly polarised light at 0° angle of incidence (and assuming the refractive index of air to be 1 regardless of temperature) can be expressed as

$$R = \left| \frac{1-n}{1+n} \right|^2, \tag{3.2}$$

where n is the refractive index of the material. This means that across small temperature changes, one could track the change in temperature in a material through the changes in reflected intensity. a diagram of the experimental setup for TTR can be seen in Figure 3.3. A frequency tripled 10 ns 355 nm Nd:YAG pump laser with a 30 kHz repetition rate and a spot diameter of 85 μm was used to heat up the sample surface and a 532 nm probe laser was used to measure the induced transient reflectivity change as the temperature diffuses through the sample. The probe laser signal, reflected back from the sample is recorded using a balanced photodetector. In order to reduce signal noise and systematic errors, a second channel in the photodetector records a reference signal from the probe laser, that is subtracted from the reflected signal. This is accomplished with the help of a half-wave (λ/2) plate, a polarising beam splitter (PBS), followed by a quarter-wave (λ/4) plate. The λ/2 plate rotates the plane of linearly polarised light in the probe laser, so that its signal can be split equally by the PBS - half proceding to the sample and half redirected to the second channel of the photodetector. The λ/4 plate transforms linear polarisation into circular and vice versa, which results in the polarisation of the reflected probe laser (after having passed the λ/4 plate twice) to rotate by 180°, causing it to be redirected in the direction opposite to the reference probe laser signal by the PBS - and towards the first channel of the photodetector.

It should be noted that the probing depth of TTR does not exceed 10 microns, and has lower sensitivity for layers under 100 nm.[90] Because of this, for the purpose of said measurements we choose to investigate the deposition area with the largest thickness (30 nm). Prior to the measurement, 10 nm of chromium and 100 nm of gold were thermally evaporated on the sample surface, in order to enhance the reflected signal from the sample. Once normalised, the obtained reflectivity trace from the measurement is equivalent to a normalised temperature trace due to the linear proportionality between the two quantities over small temperature changes. By

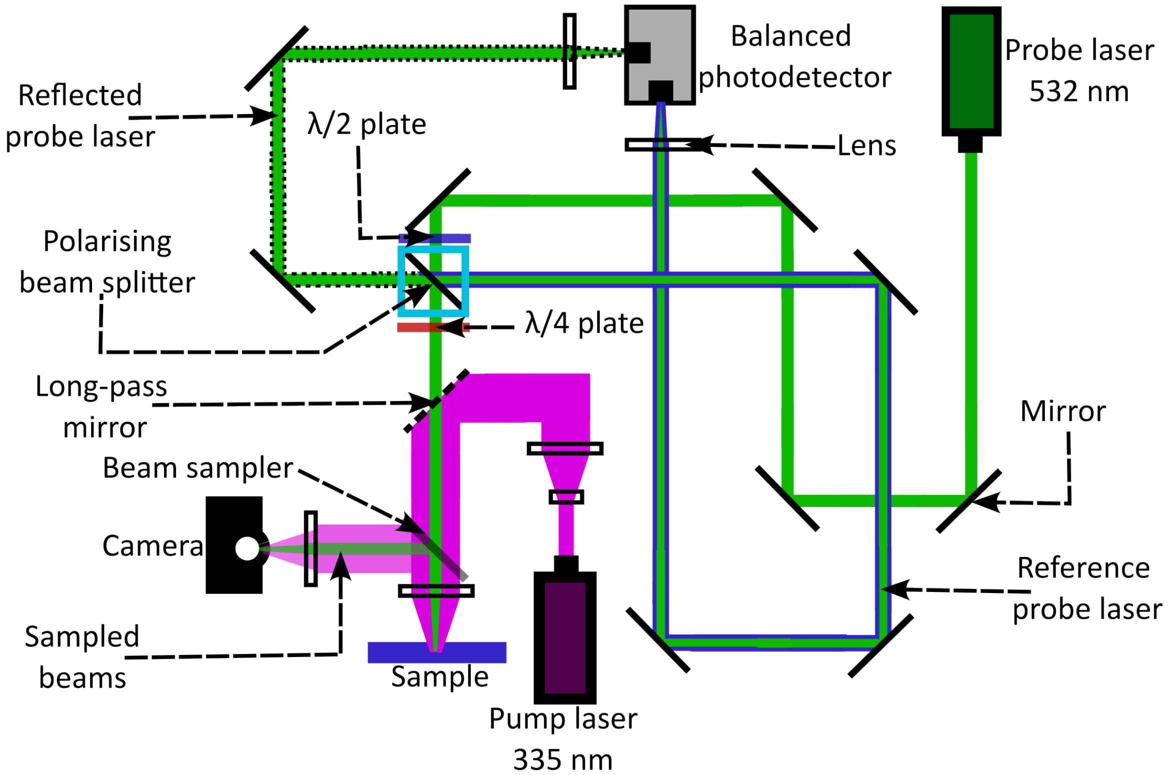
Balanced
photodetector
Probe laser
532 nm
Reflected
probe laser
λ/2 plate
Lens
Polarising
beam splitter
λ/4 plate
Long-pass
mirror
Mirror
Beam sampler
Camera
Reference
probe laser
Sampled
beams
Sample
Pump laser
335 nm

Figure 3.3: Diagram of the transient thermoreflectance (TTR) experimental setup

having the spot size of the pump laser be significantly larger than that of the probe laser, we ensure the measurement is sensitive to transport in the out of plane (z), rather than in-plane (r) direction. The pulse-induced thermal transport through the ith layer across an N-layer medium, with out-of-plane thermal conductivity κ_i, density ρ_i and specific heat capacity c_i can thus be described using

$$\frac{\partial^2 \epsilon_i}{\partial r^2} + \frac{1}{r}\frac{\partial \epsilon_i}{\partial r} + \frac{\partial^2 \epsilon_i}{\partial z^2} = \frac{\rho_i c_i}{\kappa_i}\frac{\partial \epsilon_i}{\partial t}, \tag{3.3}$$

where ϵ_i is the temperature rise through the layer. A solution to this set of transport equations has been proposed by Hui and Tan involving a transformation into the spatial and temporal frequency domain (β, s).[91] The thermal impedance Z of the entire N-layer stack can be iteratively calculated, beginning from the bottom layer, assumed to be a perfect heat sink (Z_0=0). A recursive formula for the thermal impedance at layer $i = n$ can be expressed as

$$Z_{i=1}^{i=n} = Z_n \frac{Z_{i=0}^{i=n-1} + Z_n \times \gamma_n}{Z_n + \gamma_n \times Z_{i=0}^{i=n-1}}, \tag{3.4}$$

where Z_n is $\sqrt{\kappa_n \rho_n c_n s + \kappa_n^2 \beta^2}$ for layers of $i = n > 0$, while γ_n is defined as $\tanh\left(d_n \sqrt{\frac{\rho_n c_n s}{\kappa_n} + \beta^2}\right)$. This has been incorporated into an analytical model for fitting the thermal conductivities of the constituent sample layers, as described by Yuan *et al.*,.[92]. We recorded thermoreflectance transients from the sample including the Ga$_2$O$_3$ layer as well as from the SiO$_2$ without any deposition. This helped us distinguish the contribution of the Ga$_2$O$_3$ layer on the thermal transport through the stack, and hence, to determine its out-of plane thermal conductivity.

3.3 Results and discussion

3.3.1 Band alignment to substrate

The recorded XPS spectra from the SiO$_2$ and deposited Ga$_2$O$_3$ on SiO$_2$ can be seen in Figure 3.4 **a)** in red and blue respectively. Both data sets were rigid-shifted by 2.3 eV so that the Si 2p peak from the SiO$_2$ ($E_{Si2p}^{SiO_2}$) spectrum is apparent at 103.3 eV as is standard.[93] The Si 2p peak is also visible in the Ga$_2$O$_3$-SiO$_2$ spectrum, although is slightly obscured by several overlapping Ga 3p peaks. On the Ga$_2$O$_3$-SiO$_2$ spectrum the Ga 3d peak is apparent at 21.5 eV with the additional peak at about 25 eV being related to oxidation - a characteristic feature of a Ga$_2$O$_3$ spectrum.[94] This indicates that we are indeed observing signal from gallium oxide film. These peaks are also visible in the spectrum obtained from the SiO$_2$, though with significantly lower intensity, likely appearing due to residual traces of gallium from the deposition. The SiO$_2$ XPS spectrum in the close vicinity of the valence band maximum is seen in Figure 3.4 **b)**. The value for the valence band energy is taken as the intercept of two linear fits around the points of steepest increase, determined as 4.4 eV. The error for the extracted values is related to the full width at half maximum for the XPS peaks, giving an uncertainty of ± 0.1 eV. This value is in line with expected margins of error using this method.[87]

It should be noted that while the XPS data can confirm we are dealing with a thin gallium oxide film, it cannot tell us anything more about the specific film structure. Work by Swallow *et al.,* has examined the differences in XPS spectra for different Ga$_2$O$_3$ polymorphs (α, κ, β), finding slight variations in the core peak widths for each examined polymorph. Furthermore, it is suggested that these variations result primarily from different ratios of tetrahedral to octahedral Ga-sites.[30] This approach could be useful when comparing measurements with the same instrument on two separate gallium oxide samples, giving a qualitative estimate for which one has a larger average Ga-ion coordination number. Because of this, such analysis is not applicable here, and we cannot extract any further information about the thin film structure from the XPS data.

The obtained 0.12 eV valence band offset of Ga$_2$O$_3$ with respect to SiO$_2$ is shown schematically in Figure 3.4 **c)**. The binding energy values used for calculating said offset using (3.1) from the experimental data are given in Table 3.1. Since the estimated band gap for the most stable phase, β-Ga$_2$O$_3$, is 4.8 eV, we can assume that as a value for the band gap of our film for the purpose

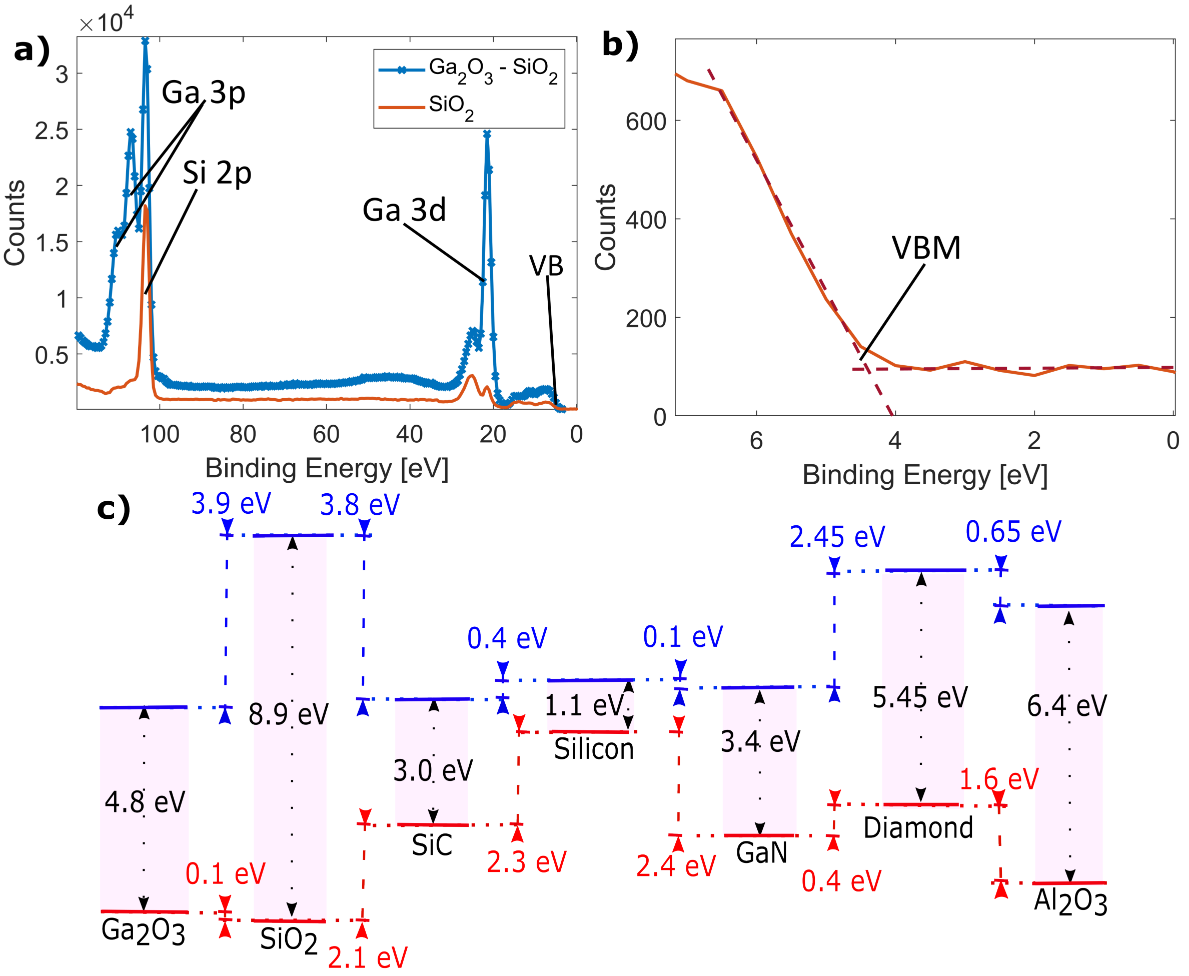

Figure 3.4: XPS energy spectra recorded from the **a)** SiO_2 and Ga_2O_3 film on SiO_2; a zoom into the valence band region for the SiO_2 is shown separately in **b)**, where the intersect of dashed lines is used to identify the valence band maximum (VBM); **c)** shows a diagram of the band alignment of the Ga_2O_3 film to the SiO_2 and extended to other materials. A band gap of 4.8 eV is assumed for our Ga_2O_3 film to determine conduction band offsets.

of estimating conduction band offsets (This assumption is consistent with discussion from Lin *et al.*, on thin film gallium oxide deposited under identical conditions[84]). Taking the silicon oxide band gap as 8.9 eV,[95] that results in a conduction band offset of -4.0 eV for our thin film Ga_2O_3 with respect to SiO_2. Comparing to reported values in the literature, considering a valence band offset of 4.4 eV between Si to SiO_2,[96] the here obtained valence band offset of Ga_2O_3 to Si ΔE_V would be -4.3 eV, with a conduction band offset of -0.6 eV. For comparison, a value of -3.5 eV was reported for the valence band offset in a PLD β-Ga_2O_3-Si interface (with a conduction band offset of 0.2 eV), showing a significant difference with the thin film deposited here.[73] The change of sign between the two conduction band offsets implies that while a β-Ga_2O_3-Si junction has type I alignment, the Ga_2O_3 film deposited in this work would have a type II alignment to

Table 3.1: Table of biding energies used for valence band offset determination.

	Ga_2O_3	SiO_2	Ga_2O_3/SiO_2
Ga 3d	20.25 eV*		21.5 eV
Si 2p		103.3 eV	103.5 eV
VBM	3.23 eV*	4.4 eV	

*Values taken from Huan *et al.*[87]

silicon. Figure 3.4 **c)** also shows predicted band alignment of the deposited thin-film Ga_2O_3 to GaN, SiC, Al_2O_3 and diamond, based on the measured band alignment of GaN with respect to SiO_2 and SiC,[97] GaN with respect to Al_2O_3,[98] and GaN with respect to diamond.[99] We thus estimate the valence band offset of the thin-film Ga_2O_3 to diamond as -2.3 eV, with a predicted conduction band offset of -2.95 eV. This alignment provides significant energetic barriers for minority carriers across a potential n-type Ga_2O_3 to p-type diamond heterojunction - about 0.8 eV higher than in PLD β-Ga_2O_3. This also correlates to a higher breakdown field in a potential Schottky barrier diode, such as the one proposed by Mishra *et al.,* using a Ga_2O_3-Al_2O_3-diamond superjunction.[22]

The question remains as to what is the cause for the energetic differences between PLD β-Ga_2O_3 and gallium oxide thin film deposited using the current method. As discussed earlier, XPS cannot give us any concrete information about the film's structure, and difficulties were encountered when attempting XRD, GIXRD and EBSD on the deposited film. Among the gallium oxide polymorphs whose band alignments has been modelled, the κ phase is the only one that has a predicted valence band level lower than in the β phase.[31] That alone, however, does not necessarily point to a different phase of gallium oxide having formed, as we know that energetic differences between phases are primarily governed by local coordination environments.[30] Such stoichiometric deviations can also occur within polycrystalline films depending on the nature and orientation of grain boundaries. Apart from the κ phase, possible similarities with the γ phase should also be considered (being the only known one with an average Ga-site coordination number lower than in β-Ga_2O_3). Currently there is no conclusive work on the energetics and band alignment of γ-Ga_2O_3. However, the phase is notable as there is evidence of γ-Ga_2O_3 forming alongside β when annealing amorphous gallium oxide.[41] Further research is required in order to confirm or reject whether the band alignment of the film deposited here is affected by γ-like defects. Some further discussion on the possible formation of γ-like defects in ion-damaged gallium oxide are given in Chapter 5 and Chapter 6.

3.3.2 Thermal transport across interface

Next, we investigate the thermal properties of the deposited thin gallium oxide film. As discussed earlier, 10 nm of Cr and 100 nm of Au were evaporated on the sample surface prior to TTR measurements. A diagram of the layers for the two areas thermoreflective transients were recorded for can be seen in Figure 3.5 **a)**. Values for the out-of-plane thermal conductivity, heat capacity and density of the individual layers are presented in Table 3.2. The thermal conductivities used for gold and SiO_2 are reduced with respect to their bulk values due to their thin-film nature.[100],[101] The thermal conductivity for the silicon is also reduced from its pure bulk literature value due to the effects of doping.[102] A sensitivity analysis[103] of the thermoreflectance transient trace with respect to the thermal conductivities of the individual layers (κ_i) was carried out and is shown in Figure 3.5 **b)**. The Sensitivity S_{κ_i} is defined as

$$S_{\kappa_i} = \frac{\partial(\ln E)}{\partial(\ln \kappa_i)}, \tag{3.5}$$

where E is the normalised temperature change. This way we decouple the contributions from each layer to the overall data, with the sensitivity analysis indicating their relative weighting when summed up into the full transient thermal response. We note that the sensitivity to the thermal conductivity of the Ga_2O_3 is fairly low, which would imply a larger uncertainty in the fitting. On the other hand, we observe a high sensitivity to the thin Cr adhesion layer. Its thermal conductivity is first determined from fitting to the data from the bare thermal oxide on the Si substrate as κ_{Cr}=0.14±0.005 $Wm^{-1}K^{-1}$, equivalent to a TBR of 7.1±0.2 m^2KGW^{-1}. The normalised transients trace measured on the thin gallium oxide film with its fit as determined by the model is shown in Figure 3.5 **c)**. With the remaining values for the layers' thermal conductivities set (including that of the Cr layer ascertained from the dataset without any Ga_2O_3 deposition), the out-of-plane thermal conductivity of the Ga_2O_3 film is obtained as 3 ± 0.5 $Wm^{-1}K^{-1}$. Taking into account the non-uniform nature of the deposition thickness, we further estimate the thermal conductivity of the film to vary between approximately 1.7 $Wm^{-1}K^{-1}$ and 4.8 $Wm^{-1}K^{-1}$ for thicknesses between 20 and 40 nm, respectively. This is in line with theoretical predictions for the thermal conductivity of $(\bar{2}01)$ β-Ga_2O_3 thin films (with expected values up to 4 $Wm^{-1}K^{-1}$ for films of about 30 nm thickness).[104] In our case, the thermal conductivity value is slightly lower, possibly due to the film not being single crystal. In any case, however, the relatively high value obtained for the thermal conductivity of the film deposited here rejects the possibility of our gallium oxide having an amorphous structure.

This thermal conductivity value for the thin film deposited here is twice as high as the thermal conductivity achieved from atomic layer deposition (ALD) of polycrystalline β-Ga_2O_3 film of comparable thickness onto diamond.[75] Previously the thermal conductivities of polycrystalline β-Ga_2O_3 films (grown by open atmosphere annealing of GaN films) have been measured in the range between 0.34 $Wm^{-1}K^{-1}$ up to 8.85 $Wm^{-1}K^{-1}$ for thicknesses ranging between 12.5 nm and 895 nm respectively, which makes the result presented here on the high end of the spectrum of predicted values.[105] While our results are consistent with expectations for a polycrystalline film, any further speculations about the film's structure from the thermal conductivity measurement cannot be made with any confidence. As will be discussed in Chapter 4, the way thermal conductivity in single crystal β-Ga_2O_3 varies with thickness further depends on the crystallographic orientation.

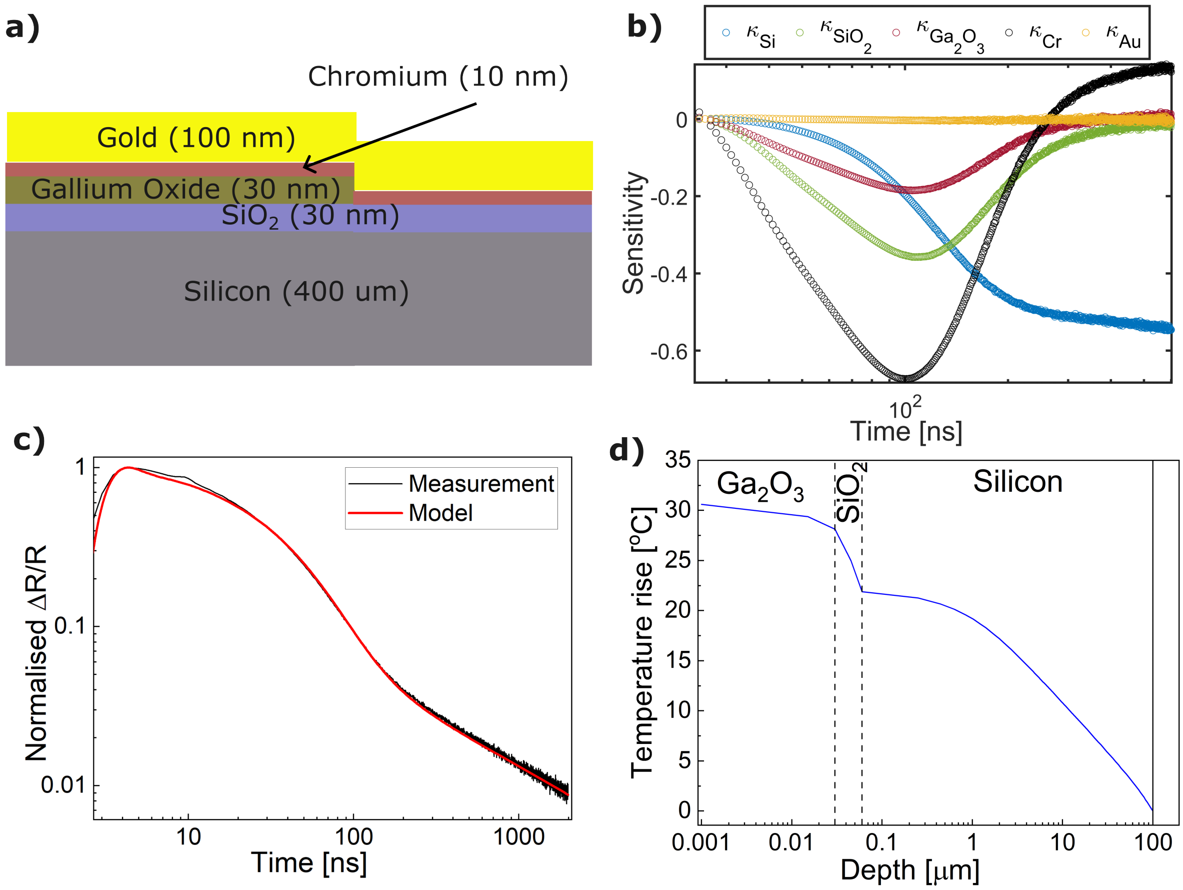

Figure 3.5: **a)** Schematics of sample layer structure - with and without Ga_2O_3 deposition. **b)** Plot of the fitting model's sensitivity to the layers' thermal conductivities as parameters. **c)** Measured and modelled transient thermoreflectance traces for data including the Ga_2O_3 layer. **d)** 2D FEM thermal simulation showing the ΔT versus depth below a 4 μm-length, 1 Wmm^{-1} heat source in the Ga_2O_3 layer.

Table 3.2: Parameters used for the TTR fitting.

Layer	Out-of-plane thermal conductivity [$Wm^{-1}K^{-1}$]	Heat capacity [$Jkg^{-1}K^{-1}$]	Density [kgm^{-3}]	Thickness [nm]
Au	200[100]	129[106]	19300[106]	100
Cr	0.14*	448[106]	7150[106]	10
Ga_2O_3	3*	560[106]	5880[106]	30
SiO_2	1.2[101]	1000[106]	2370[106]	30
Si	80[102]	700[106]	2329[106]	400,000

*Obtained from fitting the experimental data.

Because of this, we can expect domain alignemnt and size may also significantly affect the thermal conductivity changes with thickness of a polycrystalline film. It should also be noted that so far research has only been done on the thermal transport within the β and α phases of gallium oxide, so the effects of strucutural deformations on the thermal conductivity are not well studied in Ga_2O_3.

In Figure 3.5 **d)** an ANSYS 2D finite element method (FEM) simulation of the steady state temperature rise across the heterojunction is shown, using the standard and measured thermal conductivities and thicknesses given in Table 3.2. The simulation predicts a temperature rise of approximately 10° C across the SiO_2 layer from a 4 μm long 1 Wmm^{-1} heat source within the Ga_2O_3 layer. By comparison, the ΔT across the Ga_2O_3 layer is much smaller. This illustrates that for a typical device heat source (such as in a metal-oxide-semiconductor field-effect transistor (MOSFET)) the Ga_2O_3 layer presents a negligible thermal resistance because it is very thin. Therefore, this is a viable thermal management approach for a thin-channel transistor.

3.4 Conclusion

In this Chapter, we discussed the electrical and thermal properties of thin-film Ga_2O_3-SiO_2 heterostructures. We reported band offsets and out-of-plane thermal conductivity of thin-film Ga_2O_3, realized through delamination of thin passivation layers from a liquid gallium droplet onto Si with thermal oxide substrate. The estimated valence band offset of our thin film Ga_2O_3 with respect to SiO_2 is 0.1 eV and the predicted offset with respect to diamond is -2.3 eV, suggesting possibly a non-blocking interface of Ga_2O_3 with SiO_2 and a blocking interface with diamond. Moreover, out-of-plane thermal conductivity of thin-film Ga_2O_3 was found to be around 3 $Wm^{-1}K^{-1}$, which is lower than bulk β-Ga_2O_3, although higher than what has previously been achieved for polycrystalline films of comparable thickness.

CHAPTER 4

MOLECULAR DYNAMICS STUDY OF THERMAL TRANSPORT ACROSS GA_2O_3 - SUBSTRATE INTERFACES

While the thermal conductivity of β-Ga_2O_3 is known to be low and anisotropic, the effect of crystallographic orientation on the thermal interface resistance between β-Ga_2O_3 and other materials has not been studied extensively. Such knowledge is relevant and significant for optimising the design of potential device architectures. In this Chapter we use molecular dynamics simulations to investigate the crystal orientation-dependent thermal boundary resistance (TBR) across Van der Waals bonded diamond-β-Ga_2O_3 and ionically bonded amorphous Al_2O_3-β-Ga_2O_3 interfaces. We also investigate the thermal boundary between crystalline β and amorphous Ga_2O_3. We thus conclude on the optimal direction of β-Ga_2O_3 to use for reducing the TBR in these heterostructures. This chapter is based on the author's publication published in *Applied Physics Letters*.[107]

4.1 Introduction

As touched on in Chapter 1, a major concern for the implementation of β-Ga_2O_3 in devices remains the material's low thermal conductivity - anisotropic and reaching only 27 W $m^{-1}K^{-1}$ along the $< 010 >$ axis, as overheating may result in device failure.[108] Because of this, current research explores the integration of β-Ga_2O_3 with higher thermal conductivity substrates for better device thermal management. For instance, direct attachment of β-Ga_2O_3 to diamond via Van der Waals bonding has been achieved for the purpose of a photodiode p-n junction.[109] The effects of the orientation of the β-Ga_2O_3 crystal on the thermal transport across the interface, however, have not been explored. Other attempts at integrating gallium oxide with higher thermal conductivity substrates rely on adhesion via a thin interlayer, such as SiO_2 or Al_2O_3. Such interlayers are known to be necessary when growing diamond on a gallium oxide substrate[77] and β-Ga$_2$O$_3$-diamond superjunctions with Al$_2$O$_3$ interlayers have been considered.[22] Furthermore, there is evidence that the stronger bonding leads to a significant reduction in TBR between Ga$_2$O$_3$ and other materials.[75]

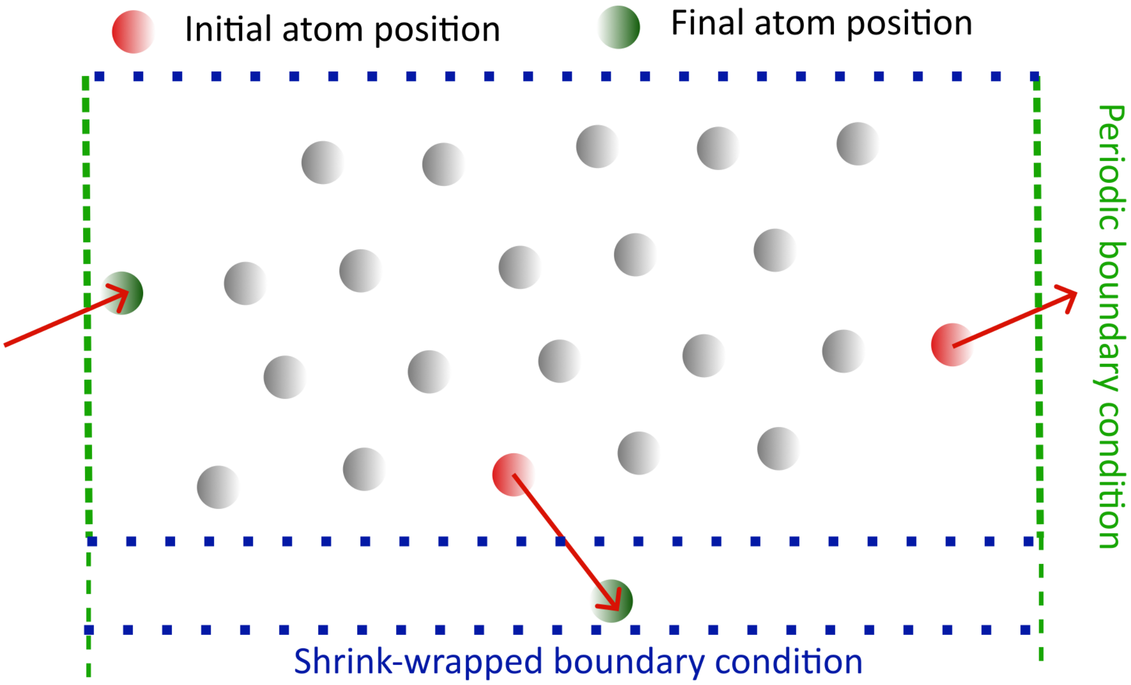
Initial atom position
Final atom position
Periodic boundary condition
Shrink-wrapped boundary condition

Figure 4.1: Boundary conditions in LAMMPS: An atom moving across the boundary under "periodic" conditions reappears on the other side, while under "shrink-wrapped" conditions, the boundary itself moves in order to include the moving atom.

Here we perform simulations to study the thermal properties of β-Ga$_2$O$_3$ along three main crystallographic axes, investigating how thermal conductivity varies with Ga$_2$O$_3$ layer thickness for different crystal orientations. We estimate the TBR across interfaces to Van der Waals bonded diamond and to ionically bonded amorphous Al$_2$O$_3$ for the (100), (010) and (001) faces of β-Ga$_2$O$_3$. We thus help identify the optimal crystallographic orientations of β-Ga$_2$O$_3$ favourable for different device concepts.

4.2 Methods

Simulation of the thermal properties of β-Ga$_2$O$_3$ were performed via the molecular dynamics code LAMMPS (Large-scale Atomic/Molecular Massively Parallel Simulator).[110] Molecular dynamics is a highly versatile computational method for simulating thermal transport through single materials as well as more complex heterostructures and even superlattices.[111][112] The code is made to incorporate Newton's equations of motion for a set of interacting particles. For a

Table 4.1: Table of pairwise interaction parameters for Born-type interatomic potential in Equation (4.1)

Pairwise interaction	A [eV]	ρ [Å]	C [eVÅ^6]
Ga-Ga[113]	0	16.0	0
Ga-O[113]	907.89	0.345	10.0
O-O (Ga_2O_3)[113]	22764.0	0.149	0
Al-Al	0	16.0	0
Al-Ga	0	16.0	0
Al-O[114]	1554.14	0.29	0
O-O (Al_2O_3)[114]	452.51	0.29	0

LAMMPS simulation, a volume is defined and populated with atoms (or other particles), whose interactions can be specified through potentials between pairs of particles (or 3-body interactions). Temperature and heat input/output may be introduced to a subset of or to all atoms, allowing for the simulation of heat sources or sinks. Boundary conditions on the simulated cell perimeter are set. Under "periodic boundary conditions", any atom that leaves the defined volume reenters from the opposite wall of the simulation box, retaining its momentum. Using "shrink-wrapped boundary conditions" allows for the simulation box to self-adjust in size to include all introduced atoms regardless of their movement. This disrupts the periodicity of the simulated system and can be used to introduce finite-size effects to the simulation. A diagram of how these two types of boundary conditions operate in LAMMPS can be seen in Figure 4.1. In the present study we primarily relied on periodic boundary conditions. Shrink-wrapped boundary conditions were only used when simulating heterostructures for the purpose of TBR calculations, along the direction of material stacking (with periodic boundary conditions along the remaining directions). Because of the orthorhombic symmetry of the simulation box in LAMMPS in contrast to the monoclinic C2/m symmetry of β-Ga_2O_3, simulation data taken along the $\hat{z}$ direction would not perfectly map onto the <001> direction, but would be closer to <-109> in the β-Ga_2O_3 crystal.

In this work a Born-Mayer-Huggins type expression for simulating the pairwise atom interaction in β-Ga_2O_3 is used. Such potential is commonly used for simulating thermal properties of oxides.[115] A general form of the potential as a function of distance r (up to a cut-off r_c) can be expressed as[116]:

$$E = A\exp(\frac{\sigma - r}{\rho}) - \frac{C}{r^6} + \frac{D}{r^8}, r < r_c, \tag{4.1}$$

where ρ is an ionic-pair dependent length parameter, σ is an interaction-dependant length parameter, while A, C and D are interaction strength parameters. When $C = D = \sigma = 0$, this is also referred to as a Buckingham potential, which used alongside a Coulombic interaction can be utilised to simulate interactions of ionically bonded materials.[117] The parameters for the pairwise interactions in Al_2O_3 and Ga_2O_3 are shown in Table 4.1. All cation-cation interactions are considered negligible as standard.[118] The cut-off r_c was set to 16.0 Å. The Coulomb interaction between the Ga^{3+} and O^{2-} ions in β-Ga_2O_3 (similarly for $Al^{1.5+}$ and O^{1-} ions in Al_2O_3) was accounted for using an adiabatic core/shell (CS) model[119] as well as a damped shifted force (DSF) model,[120] so as to avoid any unphysical divergences in the computation. The damping parameter for the DSF model was set to 0.2, similarly to previous work on simulating Ga_2O_3 done by Aller *et al.*.[121]

For simulating Van der Waals interactions between Ga_2O_3 and diamond, universal force field method potentials (UFF) are used.[122] Within molecular dynamics, UFF may be implemented as a Lennard-Jones type potential as a function of distance r up to a cut-off r_c:

$$E = 4\epsilon[(\frac{\sigma}{r})^{12} - (\frac{\sigma}{r})^{6}], r < r_c, \tag{4.2}$$

where ϵ is a parameter proportional to the well depth with units of energy and σ denotes the Van der Waals bond length. Extracting data from the 1992 work by Rappé, *et al.*, the parameters chosen for C-O interactions were set as $\epsilon = 0.00086047202$ eV and $\sigma = 3.67130766894$ Å. The parameters used for the C-Ga pairwise interaction were set to $\epsilon = 0.00226302317$ eV and $\sigma = 4.10839786291$ Å. A similar method for modelling the inter-slab interactions was recently employed for simulating Van der Waals attachment of graphene to β-Ga_2O_3.[123] Modified embedded atom method potentials (MEAM) were used for the C-C interactions in diamond.[124]

It should be noted that the interatomic potentials for β-Ga_2O_3, shown in Table 4.1 are not suitable for simulating the behaviour of other Ga_2O_3 polymorphs. When attempting to simulate an interface between β-Ga_2O_3 and κ-Ga_2O_3, the atoms on the κ polymorph side rearranged themselves into an amorphous structure. More details on this simulations and the results obtained from it are discussed later in this Chapter. In order for the present work to be extended to other Ga_2O_3 polymorphs, suitable interatomic potentials need to be prepared and tested. This could be accomplished by obtaining interatomic cohesive energy curves for the wanted crystalline polymorph or material using Density functional theory (DFT).[125]

4.3 Simulations and results

4.3.1 Thermal conductivity simulations

We first performed simulations of the thermal conductivity of β-Ga_2O_3 for different crystallographic orientations and different material thicknesses. An example of the simulation setup for these calculations is shown in Figure 4.2 **a)**. A defined volume is spanned with repeating unit cells of β-Ga_2O_3.[26] Visualisation of the material is accomplished using the VESTA (Visualisation for Electronic and Structural Analysis) software.[126] A heat source in the centre of the simulation box and two heat sinks at opposing edges are set up. Periodic boundary conditions are used; the width of the sink volumes are each set as twice as small as that of the heat source, as from a simulation standpoint the two sinks should act as a single entity due to the periodic boundary condition. First, equilibration at 300 K (room temperature) with a timestep of 1 femtosecond over 100,000 timesteps is run, followed by a further 600,000 timesteps, simulating the effects of the heat source/sinks so that a non-equilibrium steady state is reached. Finally, temperature profile data is averaged over a further 10,000 timesteps. An example of this data is seen in Figure 4.2 **b)**; the temperature change from the cold to hot reservoirs would be approximately linear, from which a value of the thermal conductivity κ may be extracted from its gradient as $\kappa = \frac{Q\Delta L}{S\Delta T}$, where Q is the amount of heat transferred across an area S, and $\frac{\Delta L}{\Delta T}$ is the inverse of the calculated temperature profile gradient. The LAMMPS code used for simulating the thermal conductivity of a (100) β-Ga_2O_3 slab of approximate thickness 120 nm is shown in Appendix A.1.

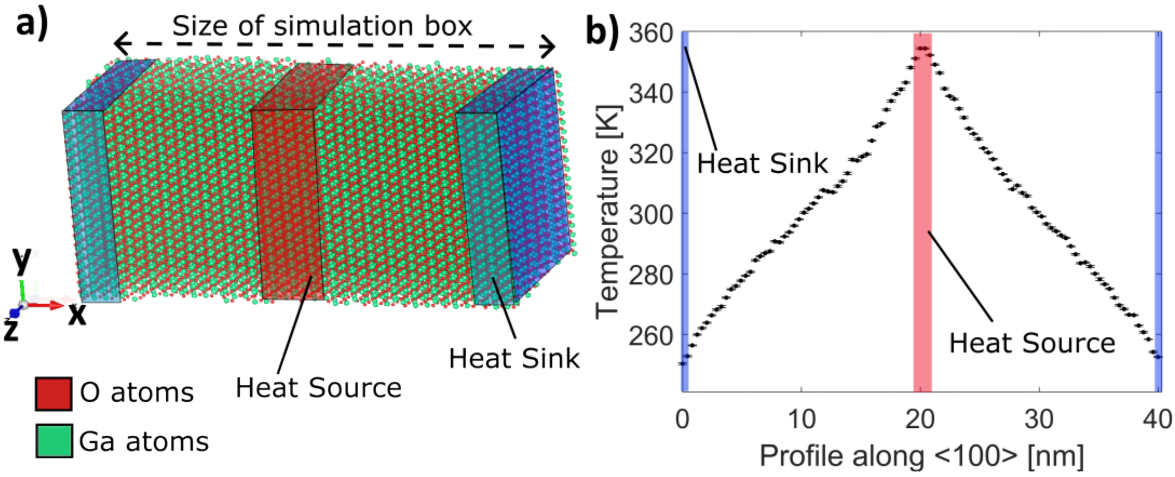

Figure 4.2: **a)** Visualisation of a Ga_2O_3 slab used in the $< 100 >$ thermal conductivity simulations. Periodic boundary conditions apply. **b)** Extracted temperature profile along $\hat{x}$-axis (corresponding to $< 100 >$ crystallographic orientation).

This method is only an approximation of the assumed behaviour of a bulk material due to the limited volume being analysed, limiting the phonon mean free path, which may lead to some of the longer-range phonon interactions within the material, to not be accounted for.[127] In the case of silicon, a linear relationship between the inverse thermal conductivity and the inverse size of simulation can be derived.[128] It can be expected that a similar type of relationship would also be observed for β-Ga_2O_3.

For each of the crystallographic directions ($\hat{x}$, $\hat{y}$ and $\hat{z}$ directions in the simulation box representing the <100>, <010> and <001>/<$\bar{1}$09> crystallographic directions respectively) the thermal conductivity is extracted from simulations of varying box size along the temperature profile direction - between 12 nm to 100 nm. Figure 4.3 shows the evolution of inverse thermal conductivity in Ga_2O_3 as a function of inverse size of simulation box for the three considered directions of thermal transport. Each data set follows a linear trend, with the fit's intercept giving

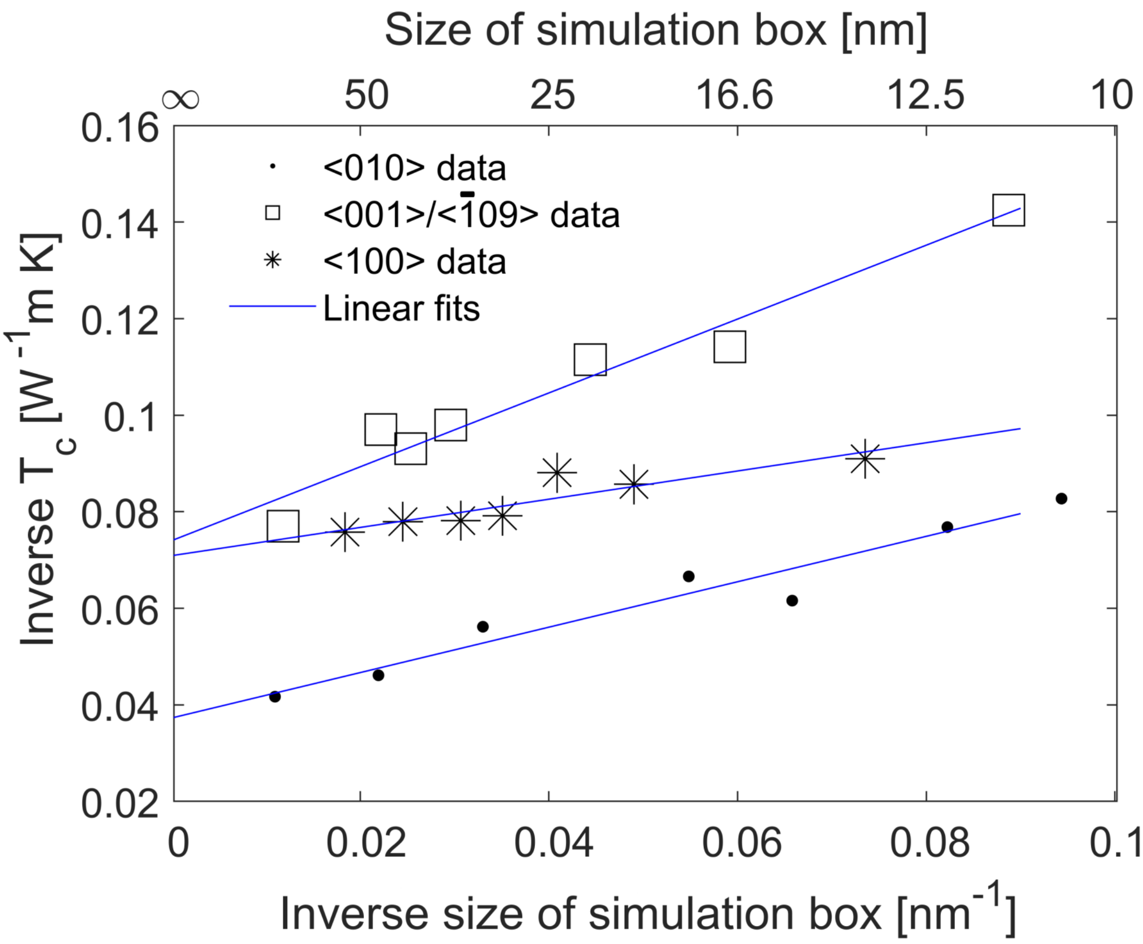

Figure 4.3: Relationship between inverse thermal conductivity and inverse size of simulation box for each of the main crystallographic directions of Ga$_2$O$_3$. Lines of best fit are included to highlight the linear nature of the trend in each case and to extrapolate the bulk thermal conductivity.

the thermal conductivity value for an "infinitely large" or bulk crystal. The value of gallium oxide's thermal conductivity obtained for the <100> direction was determined as 14.0±0.8 Wm^{-1}K^{-1}, in agreement with the experimental value of 13.0±1.0 Wm^{-1}K^{-1} obtained via a laser-flash method by Zhi Guo *et al.*.[129]<This also relates to the speed of sound below> Similarly there is agreement between the 26.8±2.0 Wm^{-1}K^{-1} value obtained for the <010> direction and the literature value of 27±2.0 Wm^{-1}K^{-1}. Finally, our obtained thermal conductivity along the $\hat{z}$ direction of 13.6±1.0 Wm^{-1}K^{-1} can be compared to the <001> literature value from the same study - 14.7±1.5 Wm^{-1}K^{-1}. These values show that the computational setup, including the choice of potentials to represent gallium oxide, is suitable for modelling the thermal properties of the material. Furthermore, the data in Figure 4.3 shows not only how thermal conductivity in β-Ga$_2$O$_3$ would vary with respect to slab thickness, but also demonstrates that this dependence has a distinct character for each of the considered crystallographic orientations. The straight line fit slopes in Figure 4.3 indicate, for example, how thermal conductivity along the $< 010 >$ direction varies with slab thickness significantly more than it does along the other investigated directions in β-Ga_2O_3. This may indicate a discrepancy in the average phonon mean free path in β-Ga_2O_3 along different crystallographic orientations.

4.3.2 Thermal interface simulations

We next model the thermal transport across the interface of Ga_2O_3 with a different material. We are first considering the case of a Ga_2O_3 slab attached to a slab of (100) diamond. Figure 4.4 **a)** shows the simulated setup. A slab of Ga_2O_3 is placed in contact proximity (~2 Å) from a diamond slab of the same cross-sectional area. The slabs are prepared with approximate size of 5 nm by 5 nm by 10 nm (with slight variation depending on crystallographic orientation). The two materials and their interface will be relaxed during the thermalisation stage of the simulation. A heat source is defined at the far end of the Ga_2O_3 slab, whereas a heat sink is defined at the end of the diamond side (with heat flux $\pm$ 1.6×10^{-7} Js^{-1}, respectively). The simulation is run with the same parameters (timestep, temperature, duration) as before in order for a temperature profile to be extracted, giving the temperature discontinuity at the interface. We calculate the TBR between two slabs as $R = \frac{\Delta T}{Q}$, where ΔT is the temperature discontinuity at the interface and Q is the heat transferred from one slab to the other.[130] The temperature profile data across the (010) Ga_2O_3 to diamond system is also seen in Figure 4.4 **a)**. The temperature discontinuity is taken as the difference between the straight lines fitted to the temperature on each side at the interface. The obtained TBR for that system is $R_{(010)}$= 55.8±0.3 m^2KGW^{-1}. This is in line with experimental measurements using time-domain thermoreflectance (TDTR), where the thermal boundary conductance of $(\bar{2}01)\beta$-Ga_2O_3 nanomembranes adhered to diamond was determined to reach as high as 17±2 $MWm^{-2}K^{-1}$, which is equivalent to a TBR of about 58.8m^2KGW^{-1}.[65] Figure 4.4 **b)** shows the simulated setup and temperature profile for the (001) face of β-Ga_2O_3 bonded ionicly to amorphous Al_2O_3, , which is run under equivalent conditions to the Ga_2O_3-diamond slabs. The calculated TBR for the (001) β-Ga_2O_3 to amorphous Al_2O_3 interface is 0.9±0.3 m^2KGW^{-1}. The obtained TBR values for each of the three main crystallographic faces of $\beta-Ga_2O_3$ interfacing with the (100) diamond and amorphous Al_2O_3 are given in Table 4.2. An example of the LAMMPS code used to simulate the Van der Waals bonded (100) β-Ga_2O_3 to (100) diamond heterojunction is given in Appendix A.1.

The TBR values for Ga_2O_3 to ionically bonded amorphous Al_2O_3 are significantly lower than those to Van der Waals bonded diamond. This is expected as TBR generally has an inverse correlation to interface adhesion strength.[131] Also, the phonon energy spectrum matching between β-Ga_2O_3[132] and Al_2O_3[133] is greater than between β-Ga_2O_3 and diamond,[134] which furthermore implies better thermal transport across the former pair of materials. We can see that there is a 70% difference between the highest ((001) Ga_2O_3 face) and lowest ((100) Ga_2O_3

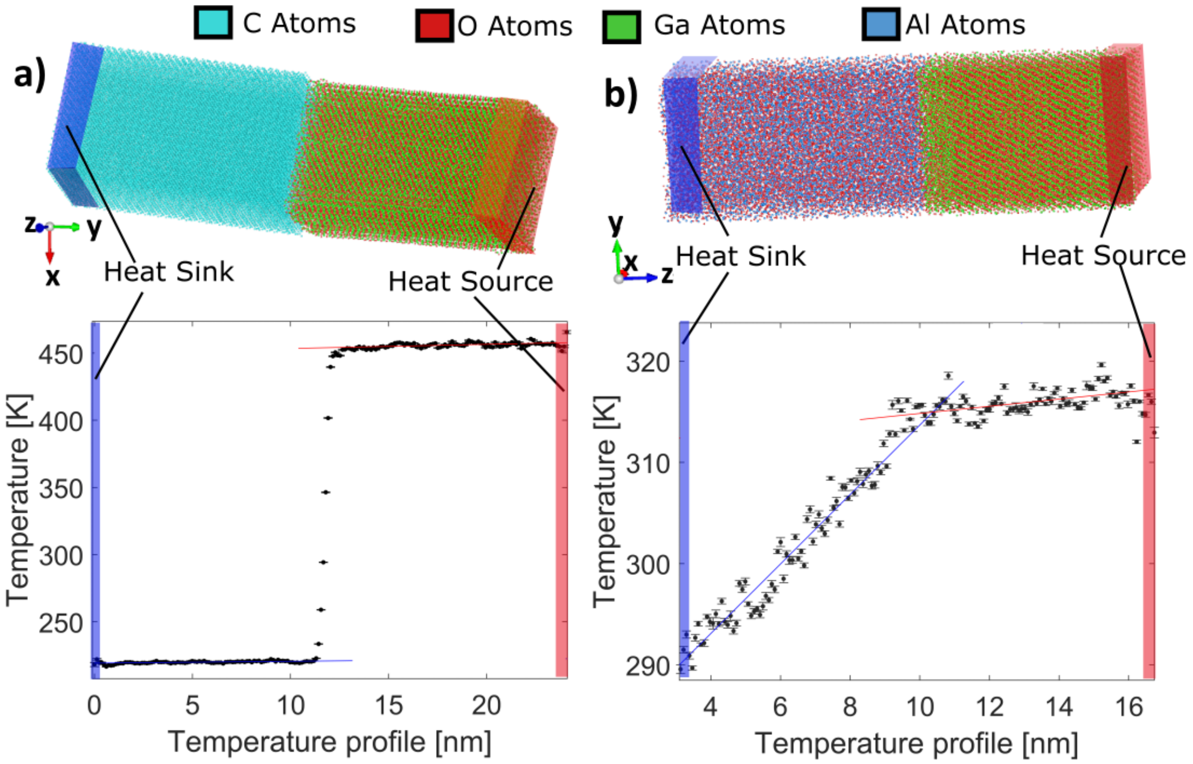

Figure 4.4: **a)** Visualisation of (010) Ga$_2$O$_3$ to diamond system; **b)** Visualisation of (001) Ga$_2$O$_3$ to Al$_2$O$_3$ system - both with extracted temperature profiles. Lines of best fit are plotted for each of the two halves for each system.

face) TBR values for a β-Ga$_2$O$_3$-diamond Van der Waals heterostructure, while all TBR values in the β-Ga$_2$O$_3$-Al$_2$O$_3$ case are equal within simulation error margins.

Due to the lower TBR between Ga$_2$O$_3$ and Al$_2$O$_3$, one could consider using amorphous Al$_2$O$_3$ as an interlayer material between Ga$_2$O$_3$ and diamond to reduce the overall interface TBR. This is in particular as a recent paper measuring the thermal boundary conductance across Al-diamond junctions with atomic layer deposited Al$_2$O$_3$ interlayer of varying thickness through time domain thermoreflectance estimated a thermal conductance of the order of 80 MWm^{-2}K^{-1}, equivalent to an effective TBR of about 12.5 m^{2}KGW^{-1} when using a 10 nm interlayer.[135] This implies a significant (3.6 times or more) reduction in the (100) β-Ga$_2$O$_3$-diamond junction TBR value when using 10 nm atomic layer deposited Al$_2$O$_3$ as interlayer, compared to a direct Van der Waals bonded β-Ga$_2$O$_3$-diamond junction. Orientation of the β-Ga$_2$O$_3$ crystal furthermore would be less important when using an Al$_2$O$_3$ interlayer as the primary TBR contribution would come from the Al$_2$O$_3$ itself.

As mentioned earlier in the chapter, we also attempted to simulate the thermal transport across an interface between β-Ga$_2$O$_3$ and κ-Ga$_2$O$_3$. Without specialised interatomic potentials for the κ phase, however, during the thermalisation stage of the simulation, the κ-Ga$_2$O$_3$ structure

Table 4.2: TBR values across interfaces between different orientations of β-Ga_2O_3 and two materials: (100) diamond and amorphous Al_2O_3.

β-Ga_2O_3 face	TBR with diamond [m^2KGW^{-1}]	TBR with amorphous Al_2O_3 [m^2KGW^{-1}]
(100)	48.6±0.3	0.8±0.3
(010)	55.8±0.3	1±0.3
(001)	83.1±0.4	0.9±0.3

that was input relaxed into an amorphous one. An example of this can be seen in Figure 4.5 **a)**, showing an amorphous slab of Ga_2O_3 in interface with the (010) face of β-Ga_2O_3. The TBR extracted across said interface is estimated as 0.9±0.3 m^2KGW^{-1}, similar to the TBR values estimated between β-Ga_2O_3 and amorphous Al_2O_3. However, unlike the Al_2O_3-to-β-Ga_2O_3 case, anisotropy in the thermal transport depending on the crystallographic orientation of the β-Ga_2O_3 slab is more noticeable here. The TBR estimated across an amorphous Ga_2O_3 to (001) β-Ga_2O_3 junctions (as seen in Figure 4.5 **b)**) is 0.56±0.3 m^2KGW^{-1}. This suggests a slightly better thermal transport across amorphous Ga_2O_3 to β-Ga_2O_3, compared to amorphous Al_2O3 to β-Ga_2O_3 junctions. This can be expected as phonon mode overlap between gallium oxides is likely to be larger than between Ga_2O_3 and other materials.[136]

One way to take this research further is using auxiliary DFT simulations. Molecular dynamics calculations strongly rely on the interatomic pair-wise potentials available, which are currently not available for Ga_2O_3 polymorphs other than β. Extracting cohesive energies, and hence interatomic interaction strengths for different Ga_2O_3 polymorphs using DFT would allow for further thermal transport simulation work, such as the one presented here, to be done. Currently, information about Ga_2O_3 thermal conductivity (anisotropic in both cases) is only known about the β and α polymorphs.[35] With access to the relevant potentials, this could further be expanded to all known Ga_2O_3 polytypes. TBR values for interfaces between materials such as diamond and other Ga_2O_3 polymorphs could also be extracted using the methods outlined in this chapter. Such simulations could show whether the use of thin film epitaxially grown Ga_2O_3 (either amorphous or different polymorph) may provide an enhanced thermal transport between β-Ga_2O_3 and high thermal conductivity substrates. Another added benefit of using DFT simulation alongside molecular dynamics is the ability to simulate the energetics of different material surface terminations or different types of surface functionalisation.[137] This could open the way for simulating more complex types of interface adhesion, such as the hydrophilic bonding between Ga_2O_3 and diamond, mentioned in Chapter 2, for example.

4.4 Conclusion

Here we have considered the thermal properties of β-Ga_2O_3 along different crystallographic directions by means of molecular dynamics simulations. We confirm that the orientation of the

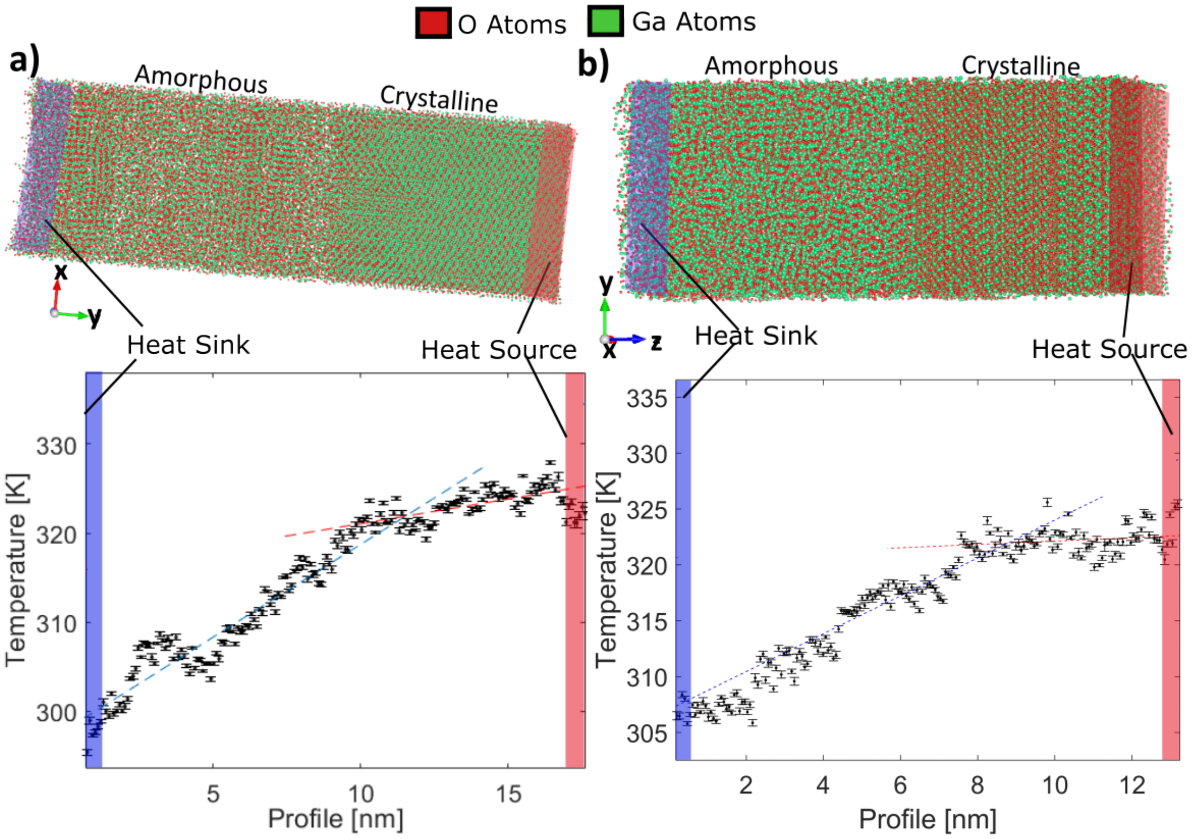

Figure 4.5: Simulations of the temperature profile across β-Ga$_2$O$_3$ to amorphous Ga$_2$O$_3$ heterojunctions, where **a)** the interface is with the (010) β-Ga$_2$O$_3$ face, and **b)** the interface is with the (001) β-Ga$_2$O$_3$ face. Lines of best fit are plotted for each of the two halves for each system.

β-Ga$_2$O$_3$ has a significant effect on thermal transport, in agreement with experimental data. Our simulations suggest that the β-Ga$_2$O$_3$ thermal conductivity change with thickness is dependant on the crystallographic orientation. We also find that the thermal boundary resistances across β-Ga$_2$O$_3$-substrate interfaces may vary significantly depending on the β-Ga$_2$O$_3$ direction/face used. We estimate the lowest TBR for Van der Waals bonded β-Ga$_2$O$_3$-diamond system as 48.6±0.3 m^{2}KGW^{-1} for the (100) face of β-Ga$_2$O$_3$, while the TBR for ionically bonded Ga$_2$O$_3$-Al$_2$O$_3$ systems is estimated around 0.9±0.3 m^{2}KGW^{-1} regardless of β-Ga$_2$O$_3$ orientation. As the $<010>$ is the direction along which β-Ga$_2$O$_3$ has its highest thermal conductivity, we suggest that $<010>$ is optimal in terms of thermal transport, when adhesion to the high thermal conductivity material is facilitated by an amorphous Al$_2$O$_3$ interlayer. We estimate that the TBR across a Ga$_2$O$_3$-diamond junction may be reduced by a factor of at least 3.6 by introducing a thin amorphous Al$_2$O$_3$ interlayer, compared to a direct Van der Waals adhesion.

CHAPTER 5

STRUCTURAL CHANGES TO β-GA_2O_3 UNDER ION IRRADIATION

In this chapter we explore the structural changes to β-Ga_2O_3 as a consequence of ion irradiation. As outlined in Chapter 1, understanding the radiation hardness of a material is important for determining the lifetime of potential electronic devices in radiation environments. Electronics on communication and navigation satellites, for example, may be subjected to a wide range of radiation including high energy heavy ions. Structural changes to β-Ga_2O_3 are also likely to affect the material's electronic properties, which have been shown to vary based on local stoichiometry. This chapter is based on the author's publication in *Applied Physics Letters*.[138]

5.1 Introduction

Wendler *et al.* used Stopping Range of Ions in Matter (SRIM) modelling[139] and Rutherford backscattering (RBS) to investigate the irradiation effects of a set of different ion types - P, Ar and Sn - on β-Ga_2O_3, identifying lattice damage primarily composed of point defects and defect complexes. They also found evidence of correlated displacement of lattice atoms that increases with ion fluence.[48] One possible explanation suggested for these observations was the emergence of a different gallium oxide phase caused by high doses of irradiation. Anber *et al.* studied the diffraction patterns of β-Ga_2O_3 before and after 200 keV Ge-ion implantation (7×10^{13}cm^{-2}).[49] The post-irradiation diffraction pattern was suggested to represent the [001] zone axis of κ-Ga_2O_3 as a deviation from the unirradiated pattern for the β-Ga_2O_3 [101] zone axis. Similar observations were also made by Azarov *et al.*, though the appearance of extra diffraction spots in the post-irradiation patterns remained unexplained in both publications.[50] Confirming a polymorph transition resulting from irradiation would be important for potential devices as it has been shown that different polymorphs of gallium oxide have different radiation hardness, for instance the surface damage accumulation rate being an order of magnitude larger for the β than for the α polymorph.[52]

The work presented here is of in situ transmission electron microscope (TEM) studies of β-Ga$_2$O$_3$ material under real time Ar ion irradiation. We demonstrate that, rather than a structural transformation, the β-Ga$_2$O$_3$ lattice remains essentially intact except for anisotropic changes in lattice dimensions during irradiation. The appearance of extra diffraction spots at high levels of irradiation are explained.

5.2 Methodology

5.2.1 Quantifying irradiation dose

Here we'll be relying on the Norgett-Robinson-Torrens displacements per atom (NRT-dpa) model to quantify ion damage in β-Ga$_2$O$_3$.[140] This model is primarily based on kinetic energy transfers above a "displacement energy" E_d threshold. This energy threshold is material specific, and in the case of β-Ga$_2$O$_3$ has been estimated as 25 eV for Ga-ions and 28 eV for O-ions.[141] The number of predicted atomic displacements N_d in the NRT-dpa model can be expressed as

$$N_d(T_d) = \begin{bmatrix} 0, & T_d < E_d \\ 1, & E_d < T_d < \frac{2E_d}{0.8} \\ \frac{0.8T_d}{2E_d}, & \frac{2E_d}{0.8} < T_d < \infty \end{bmatrix}, \tag{5.1}$$

where T_d is the available kinetic energy of incident radiation for producing atomic displacements. This model does have limitations - it is known to underestimates the damage in metals due to not fully accounting for collision cascades.[142] However, it does provide a valuable formalism for quantitative comparison of radiation damage across different materials and radiation sources by means of a common radiation damage exposure unit - displacements per atom (dpa). The unit indicates the average number of times an atom within a certain material has been displaced by incident radiation. The NRT-dpa model is particularly useful when paired with SRIM calculations, which are partially based on first principles and partially on empirical data, and are used to simulate the propagation of different species and energies of ion through materials.[139] This way N_d for a single ion event can be equated to the number of vacancies per ion introduced in a certain material as output by SRIM. Then, for an ion irradiation of fluence $\Phi_i[\frac{\text{ions}}{\text{cm}^2}]$ incident on a material with density of $\rho_A[\frac{\text{atoms}}{\text{cm}^2}]$, we can say that the total ion damage to the material dpa=$\frac{N_d}{\text{ion}} \times \rho_A \times \Phi_i$.[143] This gives us a way of converting ion fluence into a measure of damage in the irradiated material, and is the source for all dpa values appearing here.

For the TEM study a thin film sample of single crystal β-Ga$_2$O$_3$ was prepared by focused ion beam (FIB) milling,[144] from a semi-insulating Fe-doped (3.8×10^{18} cm^{-3} concentration) bulk sample with (020) surface orientation grown from the melt by Northrop-Grumman SYNOPTICS.[55] In situ ion irradiation with 400 keV Ar ions at 100° C was carried out within a Hitachi

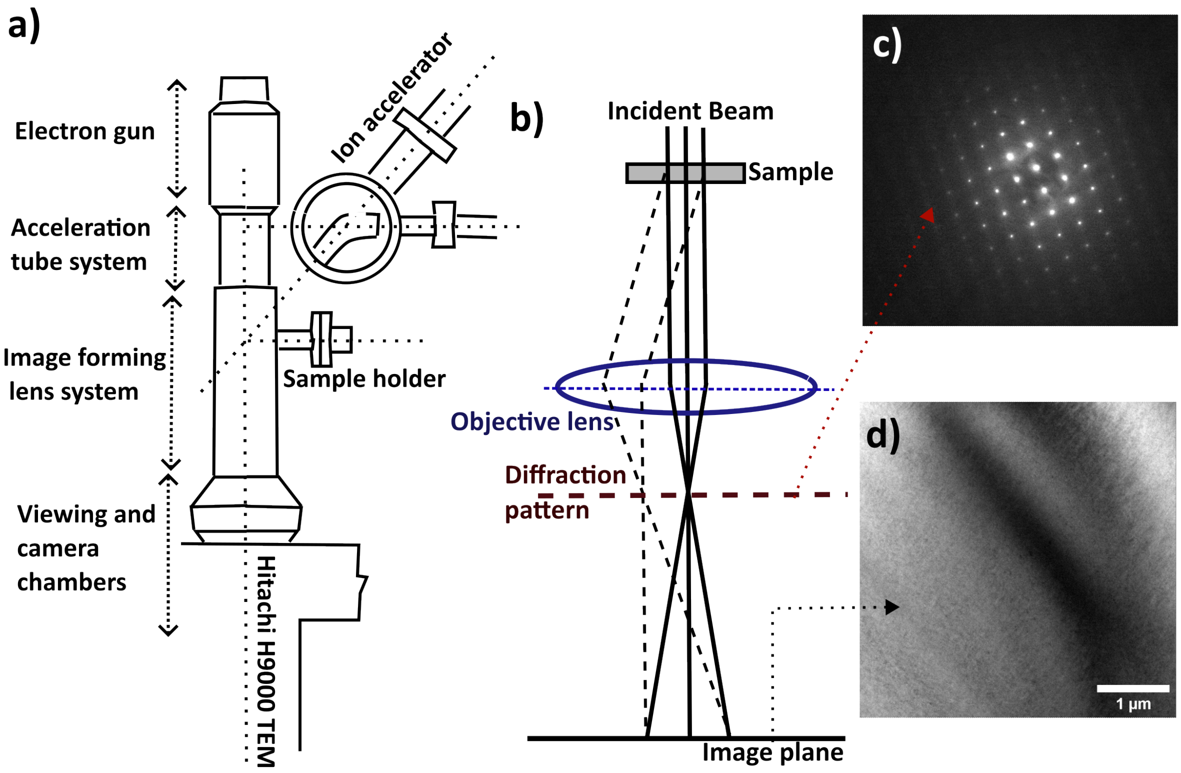
a)
Electron gun
Acceleration tube system
Image forming lens system
Viewing and camera chambers
Ion accelerator
Sample holder
Hitachi H9000 TEM
b)
Incident Beam
Sample
Objective lens
Diffraction pattern
Image plane
c)
d)
1 µm

FIGURE 5.1. **a)**Diagram of the Hitachi H9000 TEM at the IVEM-Tandem facility, equipped with 2 separate ion beam lines for in situ irradiation; **b)** A basic diagram of image formation inside a TEM, with examples of the images formed **c)** in the back focal plane - a diffraction pattern, and **d)** in the image plane - a bright field image of the sample.

9000 NAR TEM at the Intermediate Voltage Electron Microscope (IVEM) - Tandem Facility, US Argonne National Laboratory. The TEM data was recorded by Dr Dong Liu. A simple diagram of the equipment can be seen in Figure 5.1 **a)**. IVEM-Tandem is equipped with two separate ion acceleration lines with the possibility of double beam in-situ irradiation.[145] Only one ion beam line was used for the purposes of the present experiment. Ar ions were chosen as structural damage rather than doping/implantation is the main focus of this work. TEM diffraction patterns and images were collected at various stages of the irradiation process, including the unirradiated reference condition. In particular, diffraction patterns were recorded at 0.1, 0.25, 0.5, 0.75, 1, 2 and 4 dpa (displacements per atom). These values correspond to ion fluences varying from 2×10^{14}cm^{-2} (for 0.1 dpa) to 8×10^{15}cm^{-2} for 4 dpa.

5.2.2 Analysing TEM images and diffraction patterns

Here we discuss how the analysis for the obtained TEM images was performed. In a TEM, a focused and collimated electron beam is incident on a detector after passing through a specimen. Bright field (BF) imaging mainly relies on electrons from the incident beam being scattered away by the material, with the image built from the unscattered electrons in the imaging plane. A simple diagram of the image formation can be seen in Figure 5.1 **b)**, with an example bright field image in **d)**. In a crystalline sample Bragg scattering from the (hkl) plane will be occur at angles $\pm\theta_{hkl}$ that satisfy $\lambda = 2d_{hkl}\sin\theta_{hkl}$, where λ is the wavelength of the electron beam and d_{hkl} is the interplanar separation for (hkl) planes. This would cause pairs of dark Bragg contours across the bright field image, as seen in Figure 5.2 **a)**. In a perfect crystal, image contrast can be expressed from the variation in intensity I as

$$I \propto \frac{\sin^2(\pi t s)}{(\pi s)^2}, \tag{5.2}$$

where t is the sample thickness and s is the effective excitation error for the Bragg condition.[146] This provides a quick way to roughly estimate the local thickness of a sample by measuring the width of bright field Bragg contours w, where $w \approx t$. A contrast profile across a Bragg contour pair is taken and presented in Figure 5.2 **b)**, where the width of the contours can be measured. This gives an approximate sample thickness in the investigated area of about 160 nm.

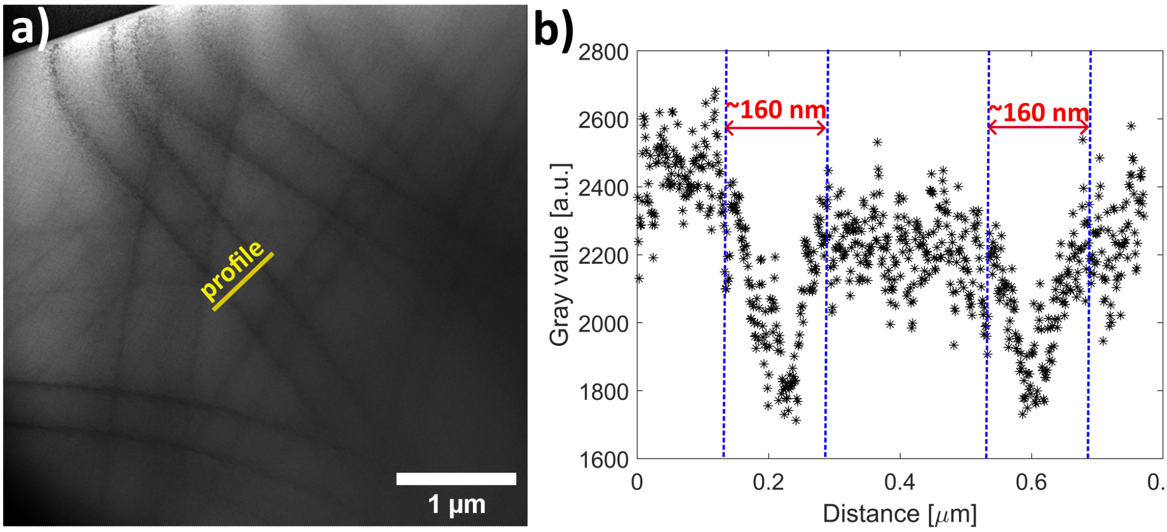

FIGURE 5.2. **a)** A Bright Field image taken at 1 dpa irradiation. Pairs of parallel Bragg contours with low intensity are visible; A contrast profile along the yellow line is taken and presented in **b)**, where the approximate sample thickness may be estimated from the width of the Bragg contours' brightness troughs.

In Figure 5.1 **b)** we can also see how the beams diffracted from an (hkl) plane in the crystal sample pass through an objective lens and intersect in its back focal plane, where a diffraction pattern image is formed. Due to constructive interference, a bright spot may be seen in said image due to the beam's diffraction off the (hkl) plane. A full diffraction pattern is then formed, as seen in Figure 5.1 **c)** from the bright spots corresponding to all possible (hkl) reflections along the particular sample axis examined. While the diffraction pattern is a reciprocal space representation of the investigated sample, from it a lot of real space information is also readily accessible. The inter plane separation d_{hkl} can be estimated using the projected distance R_{hkl} between the central beam spot and (hkl) reflection on the diffraction pattern as

$$R_{hkl} d_{hkl} = \lambda L = \text{const}, \tag{5.3}$$

where L is the focal length and $L\lambda$ the camera constant for the electron diffraction. This is also illustrated in Figure 5.3 **a)**. This means that so long as the focal length is kept consistent, inter plane separations can be estimated and compared across different sets of diffraction data from the same sample. While the diffraction patterns are 2D snapshots along a particular axis, some spatial information along the axis of observation may be retained. In reciprocal space we know that the lattice points for which Bragg diffraction occurs lie on the surface of an Ewald sphere. As is seen in Figure 5.3 **b)** The Ewald sphere can intersect the reciprocal lattice at different layers, called Laue zones. Diffraction from higher order Laue zones (HOLZ) may be seen as bright rings concentric to the central beam. Their visible radius would be dependant on the inter-planar separation in the crystal along the axis of observation. The reciprocal lattice spacing H_{hkl} can be expressed as

$$\frac{1}{H_{hkl}} = \frac{2n}{\lambda} \left(\frac{\lambda L}{r_n} \right)^2, \tag{5.4}$$

where r_n is the measured radius of the n^{th} order HOLZ ring in real space on the diffraction image taken along the $[hkl]$ zone axis.[147] HOLZ rings may be observed in any diffraction pattern, but are more prominent under convergent beam electron diffraction (CBED), where due to the introduced angle error in the direct beam, there is an extra effective thickness to the Ewald sphere surface.

In order to analyse the diffraction pattern images obtained, we use structure factor data for β-Ga_2O_3 calculated via the Visualisation for Electronic and Structural Analysis (VESTA) software, giving a list of allowed reflections for the crystal.[126] To help identify the major (hkl) reflections in a diffraction pattern using equation (5.3), we also use the following expression for the interplanar distance for a monoclinic crystal:

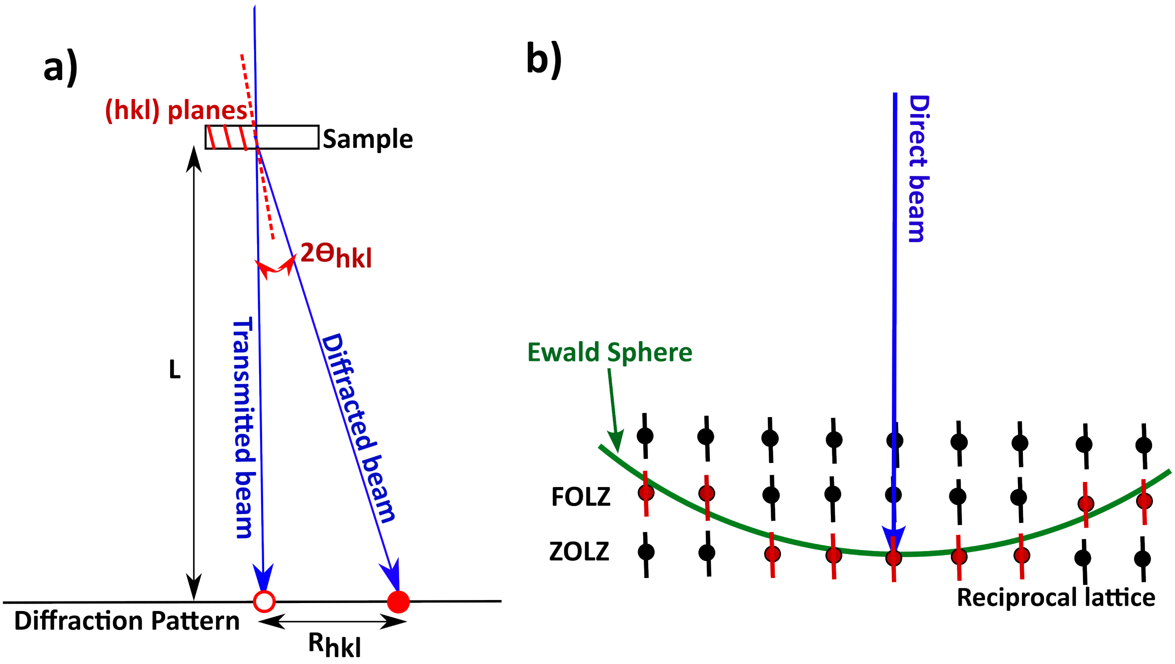
a)
(hkl) planes
Sample
L
2θhkl
Transmitted beam
Diffracted beam
Diffraction Pattern
Rhkl
b)
Direct beam
Ewald Sphere
FOLZ
ZOLZ
Reciprocal lattice

FIGURE 5.3. **a)** Diagram of diffraction pattern image formation for the (hkl) reflection; **b)** Diagram of Ewald sphere intersecting the reciprocal lattice, introducing diffraction from different Laue Zones - zero order diffraction zone (ZOLZ) and first order diffraction zone (FOLZ) depicted.

$$d_{hkl} = \frac{\sin\beta}{\sqrt{\frac{h^2}{a^2} + \frac{k^2\sin^2\beta}{b^2} + \frac{l^2}{c^2} - \frac{2hl\cos\beta}{ac}}}, \tag{5.5}$$

where β is the angle between the a and c crystallographic axes. For β-Ga$_2$O$_3$ a=12.2 Å, b=3.0 Å, c=5.8 Å and β=103.7°.[26] The observed zone axis $[uvw]$ is always perpendicular to the (hkl) reflections visible in its diffraction pattern, and hence can be determined from any two reflections $(h_1k_1l_1)$ and $(h_2k_2l_2)$ as

$$\frac{u}{\begin{vmatrix} k_1 & l_1 \\ k_2 & l_2 \end{vmatrix}} = \frac{v}{\begin{vmatrix} l_1 & h_1 \\ l_2 & h_2 \end{vmatrix}} = \frac{w}{\begin{vmatrix} h_1 & k_1 \\ h_2 & k_2 \end{vmatrix}}. \tag{5.6}$$

This gives a consistent way of indexing any observed zone axis provided two separate non-colinear reflections can be identified. The chosen $(h_1k_1l_1)$ and $(h_2k_2l_2)$ can be identified by comparing the ratio of their interplanar separations d_{hkl} using Equations (5.3) and (5.5). Another bit of information about the reflections that can be extracted from the diffraction pattern is the interplanar angle, which is the angle between the bright spot reflections in the pattern, with the angle vertex being the central beam spot. For a monoclinic crystal such as β-Ga_2O_3 one can extract an expression for the angle ϕ between planes with Miller indices $(h_1k_1l_1)$ and $(h_2k_2l_2)$ as

$$\cos\phi = \frac{\frac{h_1h_2}{a^2} + \frac{k_1k_2\sin^2\beta}{b^2} + \frac{l_1l_2}{c^2} - \frac{(h_1l_2 + h_2l_1)\cos\beta}{ac}}{\sqrt{\left(\frac{h_1^2}{a^2} + \frac{k_1^2\sin^2\beta\cos\beta}{b^2} + \frac{l_1^2}{c^2} - \frac{2h_1l_1\cos\beta}{ac}\right)} \times \sqrt{\left(\frac{h_2^2}{a^2} + \frac{k_2^2\sin^2\beta\cos\beta}{b^2} + \frac{l_2^2}{c^2} - \frac{2h_2l_2\cos\beta}{ac}\right)}}, \tag{5.7}$$

which only uses real space cell constants.[148] Finally, the indexing done can be compared to the automated β-Ga_2O_3 indexing attempt using Crystallographic ToolBox (CrysTBox).[149]

5.3 Results

5.3.1 Low irradiation doses (below 1 dpa)

The pattern prior to irradiation can be seen in Figure 5.4 **b)**. The marked reflections were measured to have an interplanar separation ratio of 2.04 (using Equation (5.3)) and interplanar angle ϕ of 28.3°. Checking against the β-Ga_2O_3 structure factor data and using Equations (5.5) and (5.7), these reflections were assigned as $(\bar{4}01)$ and $(\overline{71}2)$. Hence the zone axis in the unirradiated diffraction pattern image was identified as the [114] zone axis of β-Ga_2O_3 (using (5.6)). As camera settings were unchanged during the experiment, the [114] pattern prior to irradiation was used to calibrate observed diffraction and real-space spacings throughout the irradiation - using equation (5.3). During irradiation the sample remained crystalline, showing single crystal diffraction patterns throughout. Despite considerable lattice distortion that will be further discussed below, diffraction patterns below 1 dpa were consistent with an unchanged β-Ga_2O_3 structure. This is illustrated in Figure 5.4 **b)-d)**, which show the [114], [001] and $[1\bar{1}4]$ diffraction patterns at 0, 0.25 and 0.75 dpa respectively. A stereographic projection map of these and some other notable or major poles (zone axes) can be seen in Figure 5.4 **a)**. There one can appreciate the relative angular positions if the different poles. For example, [114] is 31° from [001] and 14.5° away from $[1\bar{1}4]$. Green lines correspond to the major Bragg contours diffracting from (hkl) planes. Such a stereographic projection image is also commonly referred to as a Kikuchi map.

The [114] zone axis pattern was also recorded at 0.1 and 0.25 dpa, though some increase in the inter-spot spacing was observed. $R_{40\bar{1}}$ at 0.1 dpa was measured to be 2.8% higher than in the unirradiated pattern, while $R_{40\bar{1}}$ at 0.25 dpa was 4.2% larger. From Equation (5.3), we know that this corresponds to a shrinkage of dimensions in real space. In Figure 5.5 the shrinkage along the $<\overline{71}2>$ and $<0\bar{2}0>$ directions with irradiation was tracked. The data point for $d_{(020)}$ at 0 dpa is

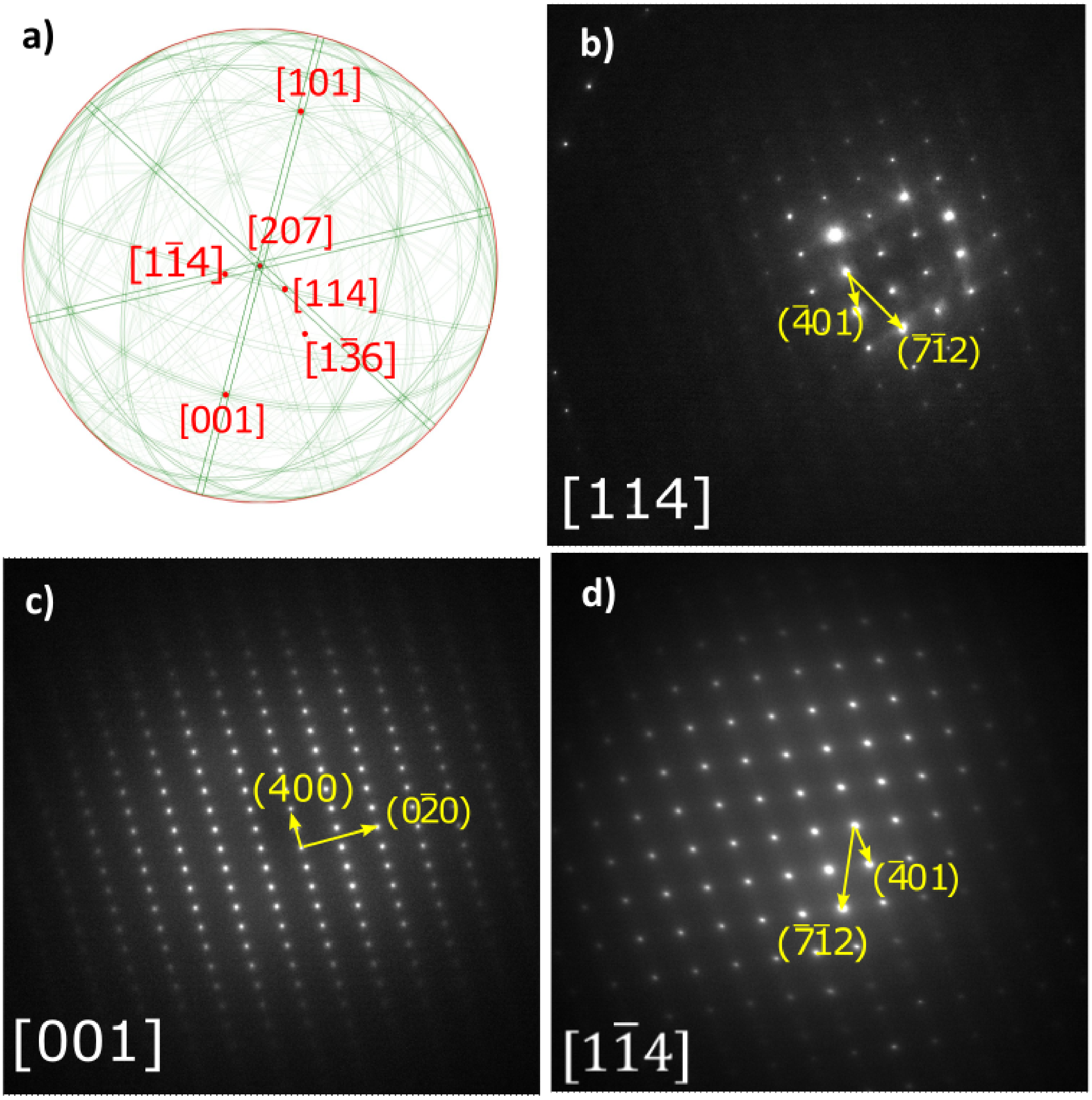

FIGURE 5.4. **a)** Stereographic projection (Kikuchi) map of β-Ga$_2$O$_3$ centred on [207]; Indexed diffraction pattern data: **b)** unirradiated [114] β-Ga$_2$O$_3$ zone axis; **c)** [001] zone axis at 0.25 dpa (also seen at 0.75 dpa); **d)** [1$\bar{1}$4] zone axis at 0.75 dpa;

taken to be the theoretical value of the (020) inter-plane separation (from Equation (5.5)) as it was not directly measured. The data above 2 dpa will be discussed in the following subsection. It is clear the main change in inter-plane separation is happening at low dpa (most significant between 0 and 0.25 dpa). To guide the eye, exponential fits are included in the figure. We can confirm that the sample has retained its single crystal nature after irradiation as Bragg contours

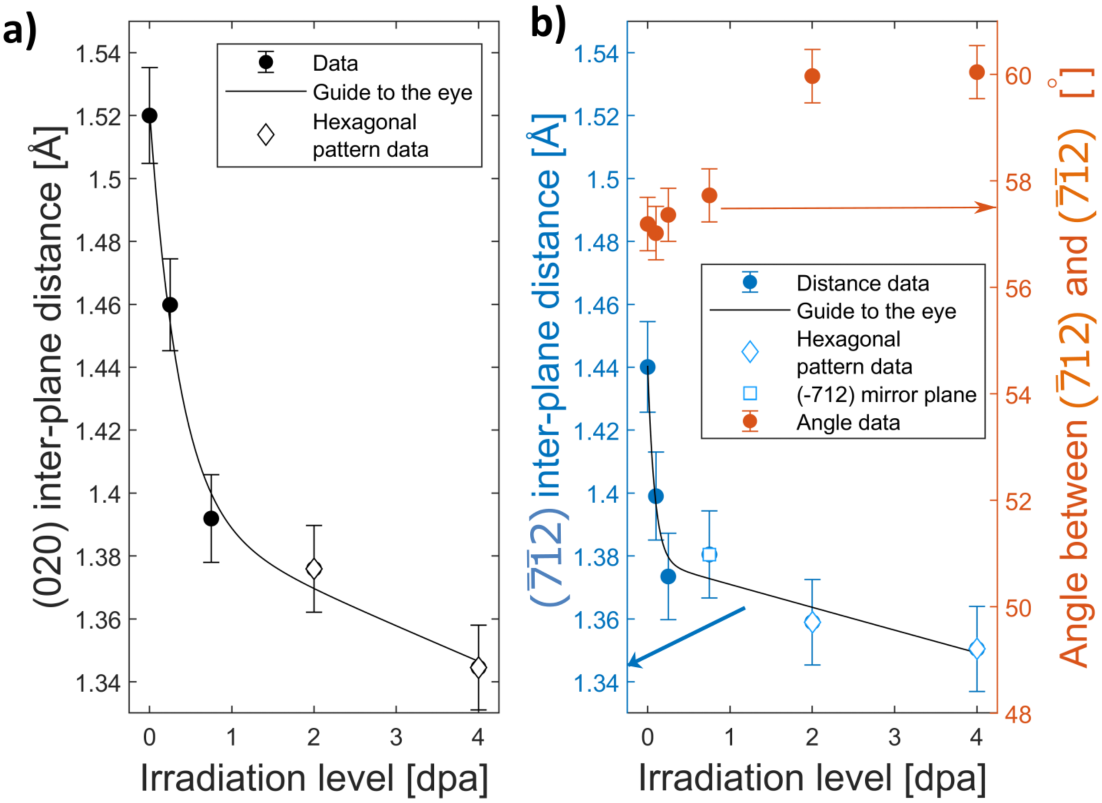

FIGURE 5.5. Changes with irradiation to **a)** the estimated $d_{(020)}$; **b)** the estimated $d_{(\overline{71}2)}$ (data point at 0.75 dpa is for the mirror-related $d_{(7\overline{12})}$ plane) on the left y-axis, and the estimated angle between $(\overline{71}2)$ and $(\bar{7}12)$ reflections on the right y-axis; Exponential fits are plotted as guides to the eye.

are clearly visible in Figure 5.2 **a)**, which shows a bright field image of the sample after 1 dpa of irradiation damage. However, graininess along prominent Bragg contours in the bright field image (especially in the upper left corner) suggests a high density of defects.

5.3.2 Higher irradiation doses (above 1 dpa)

At irradiation doses above 1 dpa, there are some further changes in the diffraction patterns. A seemingly hexagonal diffraction pattern was recorded at 2 and 4 dpa, shown in Figure 5.6 **a)**. This pattern is closely similar to that observed by Anber *et al.*. In the present case we can see that the pattern originates from the [207] zone axis of β-Ga_2O_3, due to the appearance of the $(0\bar{2}0)$ reflection (marked as **a2)**) common with [001] and $(\overline{71}2)$ (marked as **a1)**) common with $[1\bar{1}4]$ - zone axes that have both been already recorded here. The [207] zone axis views lines of Ga_2O_3 tetrahedra (T) and octahedra (O) end-on, as shown in Figure 5.6 **c)**. It is 8° away from the [114] and $[1\bar{1}4]$ axes (seen in Figure 5.4), which contain the common $(\overline{71}2)$ and $(\bar{7}12)$ reflections respectively, and 34° away from the [001] pole which contains the common (020) reflection . Although the [207] zone axis in unirradiated β-Ga$_2$O$_3$ is not hexagonal, Figure 5.5 shows that the irradiation causes the $(\overline{71}2)$ and $(0\overline{2}0)$ spacings, initially a difference of 5.6%, converge to 3.6% at 0.75 dpa, and to about 0.7% at 4 dpa. Further, the angle between the $(\overline{71}2)$ and $(\overline{7}12)$ reflections was estimated at different levels of irradiation and is shown in Figure 5.5 **b)**. It should be noted that only the data points at 2 and 4 dpa were measured directly. The values between 0 and 0.75 dpa were estimated from the measured angle between the $(\overline{71}2)$ (or $(\overline{7}12)$) and $(\overline{4}01)$ reflections (the latter of which projects on a bisecting axis between $(\overline{71}2)$ and $(\overline{7}12)$). Since these three spots are not co-planar, a small correction of +0.2° was applied, based on the angular relationship for the unirradiated material. While this ignores any anisotropic distortion in the material due to irradiation, it does demonstrate the trend for that angle to increase from 57.5° for the unirradiated reference towards 60° for the irradiated condition. Thus both the diffraction spacings and angles in the [207] diffraction pattern are seen to converge during irradiation to the limit for a hexagonal projection. It should be noted that we refer to the diffraction pattern in Figure 5.6 **a)** as "seemingly hexagonal" or "near-hexagonal". The symmetry exhibited by that diffraction pattern is similar to that of a perfect hexagonal crystal (with difference is spacing between reflections **a1** and **a2** of only 0.7% at 4 dpa and an angle between them ~60°). We opt in for categorising the diffraction pattern in this way because while β-Ga$_2$O$_3$ is not a hexagonal crystal (and does not posses a hexagonal zone axis), we observe a tendency with increasing irradiation for the aforementioned diffraction pattern (and the structure of the investigated sample) to approach (tend) closer to that of a perfect hexagonal crystal along the [207] zone axis.

It is assumed that any changes in camera length caused by significant sample buckling[150] and height shifts during irradiation have a negligible contribution to the total shrinkages in lattice spacings recorded in Figure 5.5. Thus the inter-plane separations corresponding to the spots labelled **a1** and **a2** in Figure 5.6 **a)** are estimated as 1.38 and 1.36 Å, respectively. Under the [207] zone axes these are indexed as $(0\overline{2}0)$ and $(7\overline{12})$, respectively. These spacings are less than unirradiated values by 11% and 5%, respectively, due to the anisotropic lattice deformation discussed above. Of course, it should be noted that these are extreme levels of strain observed in the material, and may seem quite surprising. In fact, strain of approximately 4% was found to cause fractures in β-Ga$_2$O$_3$ micropillars.[151] However, another recent work by Yuequin Wu *et al.,* suggests that what we're observing here may be within expectations. The researchers found that while bulk single crystal β-Ga$_2$O$_3$ can be quite brittle, fracturing at relatively low compressive strain, sub-micron single crystal pillars may exhibit plastic strain of up to 22% under compression.[152] It is quite possible that the lattice deformation we are observing here is only possible because we are specifically investigating a thin film lamella.

Type **b1** spots are positioned at the corners of diffuse hexagons surrounding the main reflections. They also maintain a relatively high intensity moving farther away from the central beam, which suggests they might originate from a higher-order Laue zone (HOLZ). For the β [207]

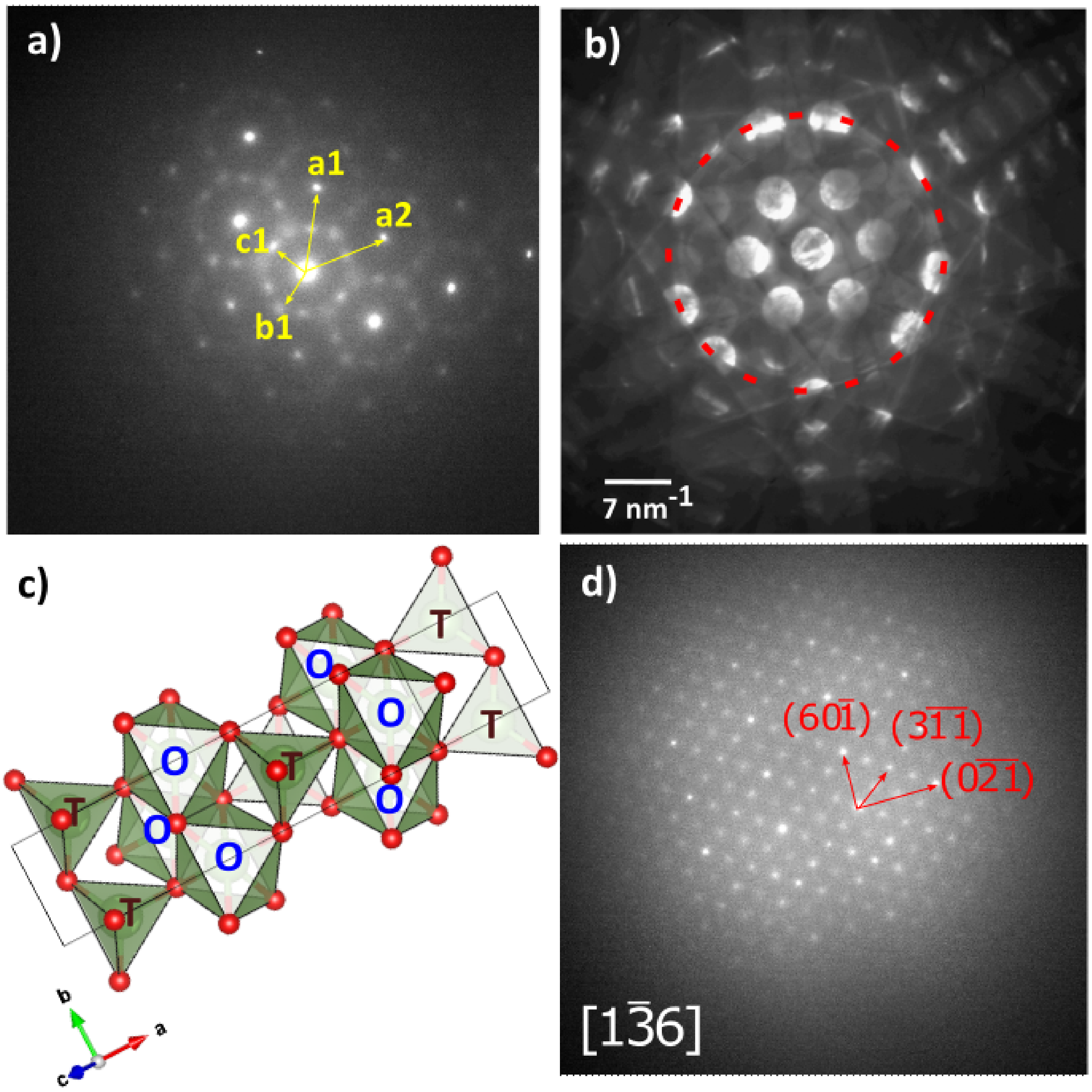

FIGURE 5.6. **a)** Near-hexagonal diffraction pattern at 2 dpa; **b)** convergent beam electron diffraction (CBED) pattern along unirradiated [207], showing higher-order Laue zone (HOLZ) rings, the first of which is marked by red circle with dotted line; **c)** β-Ga_2O_3 unit cell polyhedral view down the $< 207 >$ direction. Tetrahedral (GaO_4) and octahedral (GaO_6) sites are marked with **T** and **O** respectively; **d)** diffraction pattern at 4 dpa indexed to β-Ga_2O_3 $[1\bar{3}6]$.

diffraction pattern, this can be explained by the convergent beam electron diffraction (CBED) pattern seen in Figure 5.6 **b)**, which shows rings of strongly excited reflections where the Ewald sphere cuts through upper layer planes of the reciprocal lattice in an unirradiated sample. For the [207] CBED pattern using equation (5.4), we estimate a value for $\frac{1}{H_{[207]}}$ - the real space symmetry spacing along the $< 207 >$ direction close to 43 Å. In addition, a close examination shows that the reflections excited in the first and second HOLZ rings are relatively displaced from the zero order Laue zone (ZOLZ) reflections, such that they centre on the lattice of **b1** spots. This suggests the fainter reflections **b1** likely result from the intersection of the Ewald sphere with the tails of the upper layer reciprocal lattice spots, with higher order reflections in the upper layer becoming more intense as the first HOLZ ring is approached.[153] This includes reflections such as $(\bar{3}11)$ or $(\bar{4}01)$ that are major reflections for the [114] and $[1\bar{1}4]$ zone axes.

When indexing the pattern in Figure 5.6 **a)** to κ [001], **a1** and **a2** are closest to (330) with d_{330} = 1.46 Å, and (060), with d_{060} = 1.45Å respectively. The angle between the two reflections is 60°, in line with the angle in the pattern. The spacings for these κ [001] reflections are higher than the ones estimated from the diffraction pattern for **a1** and **a2** by 6% and 7% correspondingly. However, the absence of intensity at one-thirds and two-thirds of **a1** and **a2**, which would correspond to allowed κ reflections, suggests the emergence of κ-Ga$_2$O$_3$ [001] does not fit the results.

However, spots of type **c1** that appear at mid-points between bright reflections such as **a1** or **a2** still cannot be reliably indexed for either of the considered zone axes. These spots could be indicative of a real space period doubling. It is also observed that extra reflections were present at poles other than [207] at high irradiation levels, such as in Figure 5.6 **d)**. This diffraction pattern cannot be attributed to the κ phase of gallium oxide. This contrasts previous works, in which a radiation-induced phase transition to κ-Ga$_2$O$_3$ was proposed. It should be noted that the present study implies that a change of lattice dimensions during irradiation, up to 13% as seen in Figure 5.5, would cause stress and extensive plastic deformation in a bulk sample, such as the ones used by Anber *et al.* and Azarov *et al.*.[49][50] Whether such plastic deformation in bulk β-Ga$_2$O$_3$ could cause a phase transition, however, requires further exploration.

An indexing of the pattern in Figure 5.6 **d)** to the $[1\bar{3}6]$ β-Ga$_2$O$_3$ zone axis is proposed in the present work. This indexing matches the estimated via Equation (5.7) angular dependence between the spots indexed as $(3\bar{1}\bar{1})$ and $(0\bar{2}\bar{1})$ to be 35°, and between the spots labelled $(3\bar{1}\bar{1})$ and $(60\bar{1})$ to be 54°, as measured. The spacings ratio is also consistent with the estimate from Equation (5.5), and the estimated $d_{(0\bar{2}\bar{1})}$=1.41 Å is 4% lower than the expected pre-irradiation value. Zone axis candidates were also sought amid the different phases of Ga$_2$O$_3$: α, γ and κ. For the κ phase, for example, this would involve setting a=5Å, b=8.7Å, c=9.28Å and β=90° in Equations (5.5) and (5.7).[27] No other zone axes, however, could be identified in κ or any other Ga$_2$O$_3$ phase that would fulfil the angular and spacing dependence outlined above. The indexing proposed here, to the $[1\bar{3}6]$ β-Ga$_2$O$_3$ zone axis, however, still does not account for the faint reflections visible at half separations. We appear to be observing an axis doubling along each direction, analogous to the doubling observed for the near-hexagonal pattern in Figure 5.6 **a)** with spots of type **c1**.

A possible source of origin for the emerging diffraction spots of type **c1** within irradiated β-Ga$_2$O$_3$ could be due to ordering of ions within the interstitial site sublattice. These sites usually are determined from the symmetry of the examined material as equivalent sites within

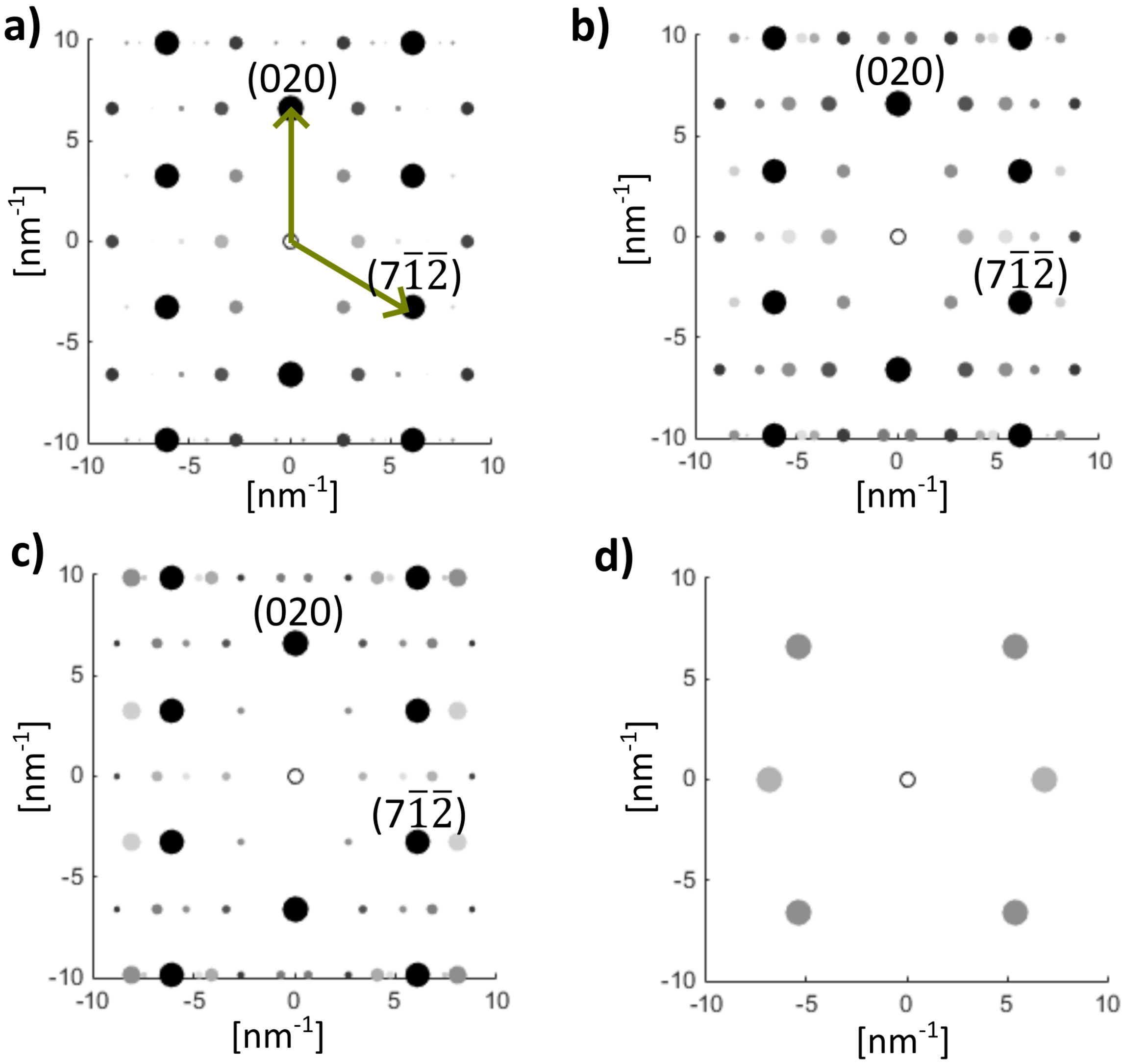

FIGURE 5.7. Simulated diffraction pattern along the [207] zone axis of β-Ga_2O_3 **a)** perfect crystal; **b)** with disrupted symmetry in the octahedral Ga-sublattice; **c)** with disrupted symmetry in the tetrahedral Ga-sublattice; **d)** with disrupted symmetry apart from the interstitial sublattice.

the material's space group, referred to as Wyckoff positions.[154] However, when dealing with a low symmetry unit cell, such as β-Ga_2O_3, that may not necessarily be the case. Blanco *et al.* identify the gallium and oxygen ion interstitial positions by looking for extremal points in β-Ga_2O_3's electron density.[113] This means that cations (Ga-ions) should be confined to electron density minima and saddle points, while anions (O-ions) - to maxima and saddle points. The researchers found that all the stable minima/maxima were already occupied in β-Ga_2O_3, leaving all interstitial positions to be the saddle points of the electron density function. Some of the consequences of this are discussed in more detail in Chapter 6. Here we consider whether a net shift of ions into a particular sublattice (the tetrahedral (GaO$_4$), octahedral (GaO$_6$) or interstitial Ga-sublattice) could produce the experimentally observed spot doubling. Figure 5.7 shows simulated diffraction patterns along the [207] zone axis in different conditions. Plot **a)** shows the diffraction pattern from a perfect β-Ga$_2$O$_3$ crystal. Plots **b)** and **c)** show pattern simulations where the symmetry has been disrupted within the octahedral and tetrahedral sublattices respectively. This means that the symmetry of the tetrahedral Ga-sublattice is retained in the former case, and the symmetry of the octahedral a-sublattice is retained in the latter. Finally, Figure 5.7 **d)** shows a diffraction pattern from a β-Ga$_2$O$_3$ material, where all symmetry has been disrupted apart from that in the interstitial site sublattice. We can clearly see that in neither of the considered cases do extra diffraction spots appear at half positions. This implies that the experimentally observed extra spots are not a result of disparity in ion ordering between the different sublattices in Simulating diffraction patterns from the interstitial-site, tetrahedral and octahedral Ga-ion sublattices in β-Ga$_2$O$_3$.

An alternative explanation for the axis doubling could be that the extra spots result from irradiation-induced defects in the crystalline structure, similar to what was observed in Al$_2$O$_3$. Apart from the equivalent stoichiometry, the polymorphs of Al$_2$O$_3$ also share the same space groups as Ga$_2$O$_3$ - both α phases belong to the $R\bar{3}c$ group, κ to $Pna2_1$ and β to $C12/m1$.[155] Tomokiyo *et al.* studied structural changes in α-Al$_2$O$_3$ as a result of electron irradiation and also reported emerging spots at half reflection distance within the [001] hexagonal diffraction pattern. The researchers observed planar faults parallel to the (001) plane, which produced extra diffraction spots within the [001] and [110] zone axes. This was attributed to rearrangement in the cation-sublattice vacancies, resulting in local changes to the stoichiometry.[156] Defects such as anti-phase boundaries, which are discontinuities within a single ordered phase, can result in such local stoichiometric deviations. Similar observations have also been made in γ-Al$_2$O$_3$,[157] with superlattice reflections attributed to periodic ordering of such planar faults.[158] Defects of this type could therefore be responsible for the observed spot doubling in the [207] and [1$\bar{3}$6] zone axis patterns of β-Ga$_2$O$_3$. A more detailed analysis of these defects in β-Ga$_2$O$_3$ are subject to further study.

5.4 Conclusion

In situ studies of β-Ga$_2$O$_3$ thin films have shown that ion irradiation up to 4 dpa causes a progressive and anisotropic reduction in lattice dimensions, but no change in crystal structure. This contrasts with previous work on ion-irradiated bulk crystals where a transition to the κ polymorph was proposed.[49][50] Above 2 dpa apparent axis doubling along each direction for multiple β-Ga$_2$O$_3$ zone axes was observed. This cannot be explained by disparity in ordering between the octahedral and tetrahedral Ga-ion sublattices with increasing irradiation, and is more likely due to localised defects.

CHAPTER 6

MODELLING OF DEFECT EVOLUTION IN β-Ga_2O_3 FROM ION RADIATION

We take a closer look at the types of defects forming in β-Ga_2O_3 under ion irradiation in this chapter. So far, we have shown β-Ga_2O_3 does not spontaneously change phase under ion irradiation, although the structure is affected by complex planar faults at high levels of irradiation. Here we consider the effects of ion beam energy on an irradiated β-Ga_2O_3 layer and the formation of defects. We also propose a cellular automaton model to track changes in β-Ga_2O_3 as a function of irradiation dose. The cellular automaton work detailed here has been presented by the author at the 5th U.S. Gallium Oxide Workshop (GOX 2022) in Washington D.C.

6.1 Introduction

Fast ions incident on a material lose energy as they travel. Ion energy may be transferred to the atomic nuclei of a material, or to the electrons. The energy loss that dominates at lower ion energies (usually up to about 0.5 MeV) is to the nuclei, and commonly leads to atoms being displaced via elastic scattering collisions, causing collision cascades.[159] The contribution of electronic energy loss, on the other hand, becomes more significant the higher the incident ion energy. It tends to cause intense local ionization damage, but may also lead to defect recovery.[160] What type of damage a certain material incurs under irradiation largely depends on the interplay between those two modes for ion energy loss.

A 2019 study by Hanson *et al.,* investigated the competing and synergistic effects of nuclear and electronic energy loss on Ti_3SiC_2 under a combination of 4 MeV Au, 17 MeV Pt, and 14 MeV Cl ion irradiations, examined via x-ray diffraction and TEM. They found nuclear energy loss to be primarily responsible for structural changes, such as anti-phase defects, while electronic energy loss was found to increase lattice strain.[161] How different energy ion irradiation may affect β-Ga$_2$O$_3$, and what is the interplay of the two ion energy loss modes for the material, however, are still open questions. This information would be relevant for potential Ga$_2$O$_3$ devices for space applications, since heavy ion irradiation originating from solar flares may reach up to 10 MeV.[10]

In this Chapter we consider the observed damage from 200 keV Ar ions on β-Ga$_2$O$_3$ (as detailed in Chapter 5) and compare with observations on a gallium oxide sample after 2 MeV Ar ion irradiation. We further explore the competing nature of nuclear and electronic ion energy loss in β-Ga$_2$O$_3$ by means of SRIM simulations. We also explore the evolution of simple defects (such as vacancies) in the material as a function of ion damage by means of a cellular automaton model.

6.2 Methodology

We prepared a sample for study under TEM, similar to the one described in Section 5.2. A bulk single crystal β-Ga$_2$O$_3$ sample with (020) surface orientation grown from the melt by Northrop-Grumman SYNOPTICS[55] was irradiated with 2 MeV Ar+ ions by Dr Luke Antwis at the University of Surrey Ion Beam Centre with a fluence of 6×10^{15} cm^{-2} at 100° C, corresponding to a damage level over 2 dpa across 1.3 Å of ion penetration depth. A TEM-ready sample was then prepared by Dr Junliang Liu at the University of Oxford by focused ion beam (FIB) milling. This allows for a direct comparison of irradiated and unirradiated regions of the sample under TEM.

To accompany the experimental work, some modelling of the expected β-Ga$_2$O$_3$ behaviour under ion irradiation are also undertaken. Stopping range of ions in matter (SRIM) simulations of Ar-ion irradiation of β-Ga$_2$O$_3$ are used to provide a direct comparison with the experimental work detailed here and in Chapter 5. A cellular automaton model was also prepared in an attempt to capture the full dynamics of the irradiation process.

6.2.1 SRIM simulations

SRIM calculations are partially based on first principles and partially on experimental data. For estimating the stopping power of light radiation in materials, the calculations rely on the so called "Core and bond" (CAB) approach. CAB goes beyond the general Bragg's rule, according to which stopping power in a compound can be expressed in a linear combination of the stopping powers of the individual elements making it up[162]. Instead, CAB suggests a superposition of radiation stopping by atomic cores with radiation stopping from bonding electrons.[163] The CAB correction has helped the SRIM prediction accuracy of H and He ion stopping in compounds to reach over 98%.[139]

For the stopping range of heavier ions, the charge state of the incident radiation needs to be further considered. SRIM here relies on Brandt-Kitagawa theory, according to which an incident ion loses any electrons with velocity below the relative velocity of the ion with respect to the target material.[164] When also considering fast ions (with energy over 1 MeV), high velocity effects are accounted for using Bette-Bloch theory, which primarily deals with electronic ion energy loss. According to it, the energy transfer, ΔE, between an ion of charge Ze travelling at velocity v and an electron within the material (charge e and mass m) can be expressed as

$$\Delta E = \frac{2Z^2e^4}{mv^2b^2}, \tag{6.1}$$

where b is an impact parameter. The stopping power is then obtained by integrating the transferred energy over all possible impact parameters b.[165]

SRIM works by simulating a large number (usually 100,000) of single ion collision events and taking a statistical average of the estimated quantities, such as number of vacancies per ion, energy loss per ion, and more. We perform multiple SRIM calculations on β-Ga_2O_3 under Ar ion irradiation of varying energy - 100 keV, 200 keV, 500 keV, 1 MeV, 1.5 MeV and 2 MeV. For each of them energy loss curves with respect to depth of ion penetration are extracted.

6.2.2 Cellular automaton model

Cellular automata are discrete models that consist of an N-dimentional grid of cells, where N is finite, and each cell may be in one out of a finite number of states, n. An initial state at irradiation t=0 dpa is specified for each cell, and then for each subsequent step, t=t+Δt, a rule is followed to determine the new state. The rule is usually a mathematical function that involves the states of the neighbouring cells.[166] Cellular automata have found numerous applications in modelling physical, chemical and even biological systems.[167]

Here we propose a cellular automaton (CA) model for the atomic displacements in β-Ga_2O_3 under ion irradiation. In this case, we are working with an N = 3-dimensional grid, where each cell corresponds to a gallium, oxygen or interstitial site that may be occupied. As briefly discussed in Chapter 5, the 2005 ab initio theoretical work by Blanco *et al.,* identifies the interstitial positions in β-Ga_2O_3, where ions may be displaced to, as the saddle points of the material's electron density function.[113] As such, these interstitial sites may be occupied by both anions and cations. The positions of these interstitial sites within the β-Ga_2O_3 unit cell can be seen in Figure 6.1 as they form channels along the $< 010 >$ direction. The fractional coordinates of all sites in the β-Ga_2O_3 unit cell are given in Table 6.1, together with their occupation energies and nearest neighbouring sites, to which they may displace to.

The CA grid is spanned by all sites within a dim^3 stack of β-Ga_2O_3 unit cells, where dim may be user-defined. For each site (cell within the model), the following information is recorded: a unique site ID, Cartesian coordinates, the site's type (Ga-site, O-site or interstitial), a list of nearest neighbour IDs, and a list of the nearest neighbour site types. Nearest neighbours are taken as sites at a maximum distance of 2.5 Å, which is about 20% above the average bond length

Table 6.1: Table of β-Ga$_2$O$_3$ unit cell base and interstitial sites, including fractional coordinates, occupation energies, and nearest neighbours for displacement.

Site number	Site type	Fractional coordinates	Ga-ion energy [eV][113]	O-ion energy [eV][113]	Displacement Neighbours
1	Interstitial	(0,0,0)	-39.5	-11.8	2, 17, 18, 25, 26, 33, 34
2	Interstitial	(0,0.5,0)	-37.8	-11.5	1, 17, 18, 21, 22, 33, 34
3	Interstitial	(0,0,0.5)	-40.2	-12.2	4, 17, 18, 29, 30, 33, 34
4	Interstitial	(0,0.5,0.5)	-37.2	-11.7	3, 17, 18, 21, 22, 33, 34
5	Interstitial	(0.5,0,0)	-39.5	-11.8	6, 19, 20, 23, 24, 35, 36
6	Interstitial	(0.5,0.5,0)	-37.8	-11.5	5, 19, 20, 27, 28, 35, 36
7	Interstitial	(0.5,0,0.5)	-40.2	-12.2	8, 19, 20, 23, 24, 35, 36
8	Interstitial	(0.5,0.5,0.5)	-37.2	-11.7	7, 19, 20, 31, 32, 35, 36
9	Interstitial	(0.25,0.25,0)	-39.4	-14.4	13, 17, 20, 21, 24, 25, 28
10	Interstitial	(0.25,0.25,0.5)	-36.1	-12.0	14, 21, 24, 25, 28, 29, 32,
11	Interstitial	(0.75,0.25,0)	-39.4	-14.5	15, 18, 19, 22, 23, 26, 27
12	Interstitial	(0.75,0.25,0.5)	-36.1	-12.0	16, 22, 23, 26, 27, 30 ,31
13	Interstitial	(0.25,0.75,0)	-39.4	-14.4	9, 17, 20, 21, 24, 25, 28
14	Interstitial	(0.25,0.75,0.5)	-36.1	-12.0	10, 21, 24, 25, 28, 29, 32
15	Interstitial	(0.75,0.75,0)	-39.4	-14.4	11, 18, 19, 22, 23, 26, 27
16	Interstitial	(0.75,0.75,0.5)	-36.1	-12.0	12, 22, 23, 26, 27, 30, 31
17	Base Gallium	(0.09,0.00,0.79)	-53.3	N/A	1, 2, 3, 4, 9, 13
18	Base Gallium	(0.91,0,0.21)	-53.3	N/A	1, 2, 3, 4, 11, 15
19	Base Gallium	(0.59,0.5,0.79)	-53.3	N/A	5, 6, 7, 8, 11, 15
20	Base Gallium	(0.41,0.5,0.21)	-53.3	N/A	5, 6, 7, 8, 9, 13
21	Base Gallium	(0.16,0.5,0.31)	-52.2	N/A	2, 4, 9, 10, 13, 14
22	Base Gallium	(0.84,0.5,0.69)	-52.2	N/A	2, 4, 11, 12, 15, 16
23	Base Gallium	(0.66,0,0.31)	-52.2	N/A	5, 7, 11, 12, 15, 16
24	Base Gallium	(0.34,0,0.69)	-52.2	N/A	5, 7, 9, 10, 13, 14
25	Base Oxygen	(0.16,0,0.11)	N/A	-21.4	1, 9, 10, 13, 14
26	Base Oxygen	(0.84,0,0.89)	N/A	-21.4	1, 11, 12, 15, 16
27	Base Oxygen	(0.66,0.5,0.11)	N/A	-21.4	6, 11, 12, 15, 16
28	Base Oxygen	(0.34,0.5,0.89)	N/A	-21.4	6, 9, 10, 13, 14
29	Base Oxygen	(0.17,0,0.56)	N/A	-21.1	3, 10, 14
30	Base Oxygen	(0.83,0,0.44)	N/A	-21.1	3, 12, 16
31	Base Oxygen	(0.67,0.5,0.56)	N/A	-21.1	8, 12, 16
32	Base Oxygen	(0.33,0.5,0.44)	N/A	-21.1	8, 10, 14
33	Base Oxygen	(0,0.5,0.26)	N/A	-22.1	1, 2, 3, 4
34	Base Oxygen	(0,0.5,0.74)	N/A	-22.1	1, 2, 3, 4
35	Base Oxygen	(0.5,0,0.26)	N/A	-22.1	5, 6, 7, 8
36	Base Oxygen	(0.5,0,0.74)	N/A	-22.1	5, 6, 7, 8

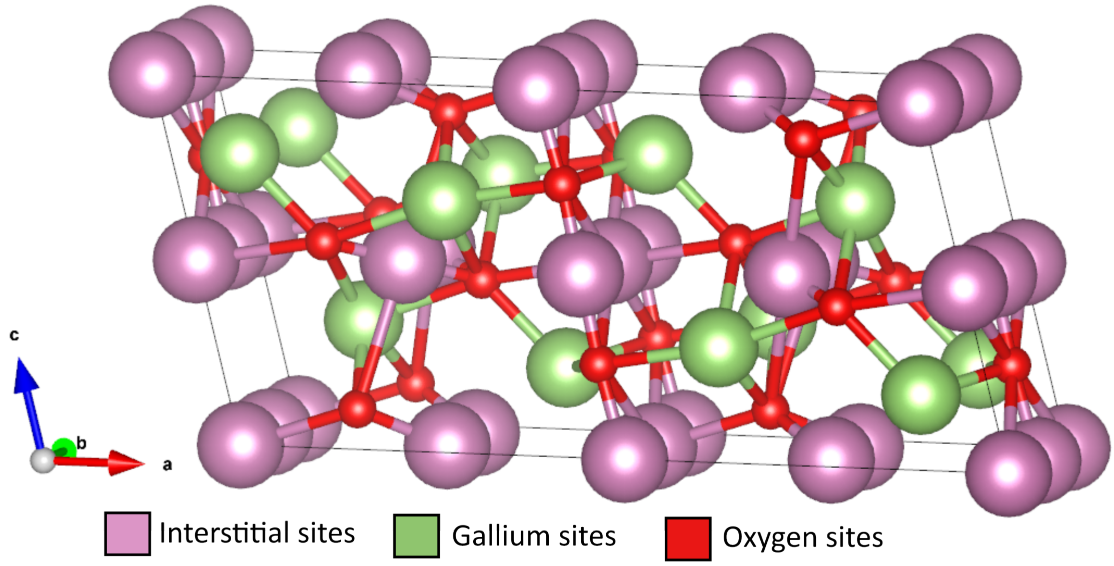

FIGURE 6.1. β-Ga_2O_3 unit cell with included interstitial sites in purple.

in β-Ga_2O_3.[168] As only a finite volume may be simulated, boundary conditions are considered. When extracting data from the model, the information from the outermost unit cells in the dim^3 stack is ignored. This is done as the atoms at the edge of the simulation do not have their full set of nearest neighbours. Because of this, the simulated volume that gives useful information within the model consists of $(dim-2)^3$ unit cells.

At each simulation step, for each site with unique ID, we record its occupancy (whether occupied by a Ga-ion, O-ion or is empty). If occupied, we also record the site's energy, which is ion type-dependent and can be seen in Table 6.1. Since we are modelling the effects of irradiation, we thus equate each subsequent step of the simulation as a state of further irradiation, measured in dpa. The concept of dpa is expanded on in Section 5.2. We set Δt =0.1 dpa, which means that for each subsequent simulation step, any occupied cell has a probability $P = 0.1$ to displace its occupying ion to the empty neighbouring site with the minimum potential energy. At each step for an occupied cell thus we can also record a list of IDs for each other cell where the occupying atom has passed through. This way the CA model provides a unique possibility to track the full dynamics of the system under irradiation. Because of the way the model is defined, it does allow for subsequent displacements of the same ion within the same simulation step, and hence allows for collision cascades to occur. The main limitation of the model is that it is based on a rigid grid of cells simulating a finite volume of β-Ga_2O_3. Because of this, it cannot account for more complex planar defects, such as anti-phase boundaries. The information that may be extracted from this model includes the change in total energy within the material, the change in average coordination number of atomic species, the number of vacancies, and more. Its strength is primarily in its predictive power of general trends and their evolution with increased irradiation. The code for the CA model can be found in Appendix A.2.

6.3 Results

6.3.1 Coordination number and vacancy evolution

A simulation of size dim=10 was run over 25 steps, with boundary conditions taken into account. This corresponds to data extracted from a volume containing 10,240 atoms (18,432 sites including the initially empty interstitial positions) up to an irradiation level of 2.5 dpa. To put this into perspective, a $dim = 4$ CA grid is visualised in Figure 6.2 **a)**, which when boundary conditions are accounted for would only extract data from simulation over 160 atoms. From the dim=10 simulation, data is extracted concerning the change in coordination number of the gallium ions, the change in internal energy per atom of the system (with regards to which sites are occupied), and finally the change in number of vacancies as a function of irradiation dose.

As touched on in Chapter 1, changes in the Ga-ion coordination number have an effect on Ga_2O_3 electronic states. Specifically, this contributes to varying band gap values for the different Ga_2O_3 polymorphs - estimated to range between 4.7 eV for ϵ-Ga_2O_3 and 5.6 eV for α-Ga_2O_3 as predicted by DFT. Valence band maxima have also been estimated to vary by as much as 0.8 eV between the κ and ϵ phases.[31] While in Chapter 5 we confirmed that the general structure of β-Ga_2O_3 under ion irradiation does not switch to a different polymorph, that does not mean that local changes to the material's stoichiometry and bonds do not occur. From Figure 6.2 **b)** we see that the average coordination number of Ga-ions sharply decreases with increasing irradiation level up to 1 dpa, after which it remains relatively constant. It starts off at 5 (with an equal number of octahedral and tetrahedral sites) and finally fluctuates around 4.25 at high levels of irradiation. This decrease is due to the fact that no interstitial sites in β-Ga_2O_3 are octahedral with respect to oxygen - half of them are tetrahedral, while the other half have a local coordination number of 2 with respect to oxygen. This is significant as the only known Ga_2O_3 polymorph with an average Ga-ion coordination number lower than 5 is γ-Ga_2O_3, with 4.85. Ignoring the fractional occupancy in the different Ga-sites, the coordination number for all available Ga-sites would be reduced down to about 4.44.[29] This implies some similarity between irradiated β-Ga_2O_3 and γ-Ga_2O_3 with regards to local coordination environments. This may relate to the γ phase-like defects Kjeldby *et al.,* observed in Si-implanted β-Ga_2O_3 after annealing.[51] Furthermore, γ-Ga_2O_3 has been identified to form locally at the boundaries between different Ga_2O_3 phases,[41] which is another connection between structural changes in Ga_2O_3 and a reduction in local Ga-ion coordination number.

The change in internal energy per atom in the system is shown in Figure 6.2 **c)**. This is calculated from the occupation energies (listed in Table 6.1) for all non-vacant sites at each stage of irradiation modelling. Similarly to the plot of Ga-ion coordination number, the energy per

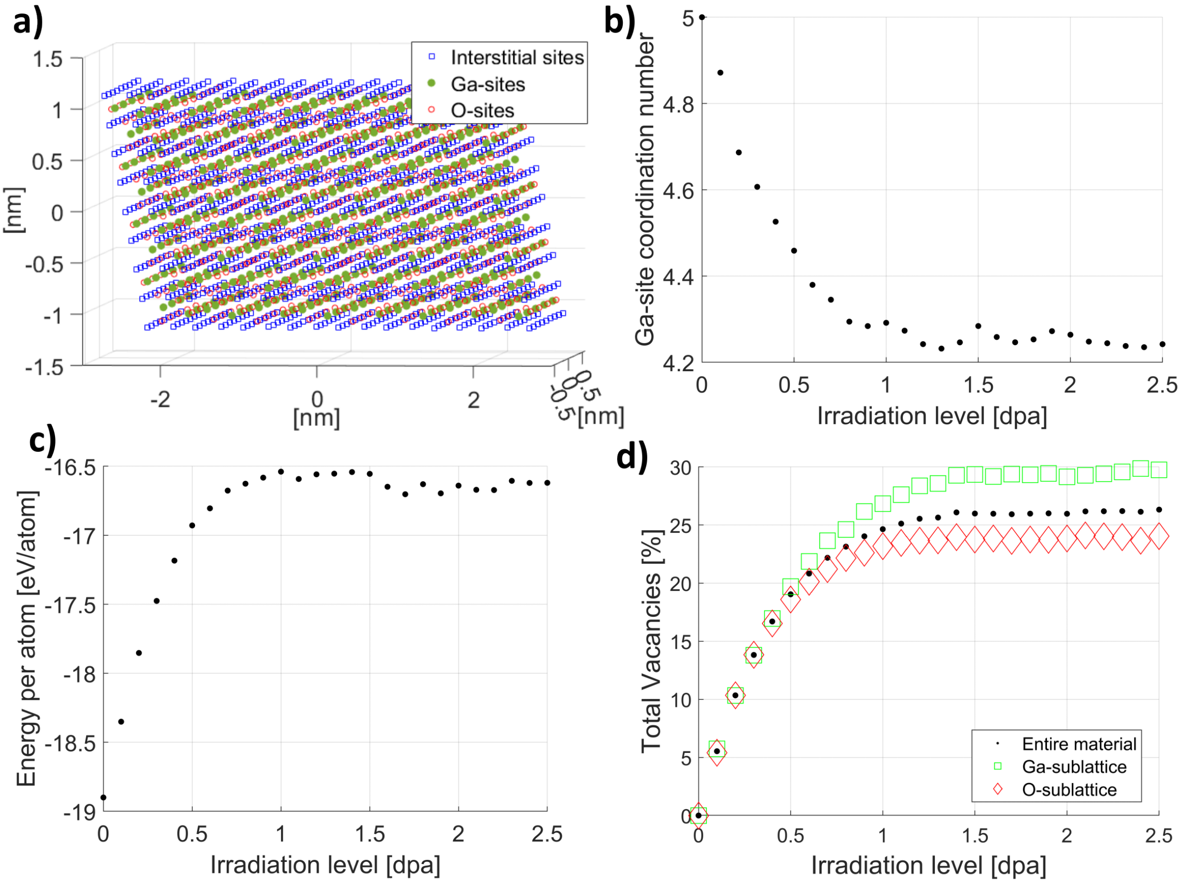

FIGURE 6.2. **a)** *dim*=4 CA grid with different site types labelled; CA model results for ion irradiation on β-Ga_2O_3. Evolution as a function of irradiation damage for the **b)** Ga-ion coordination number, **c)** average energy per atom for all occupied sites in the system, and **d)** total number of all vacancies (in percent), by atomic species.

atom changes most significantly at low levels of irradiation, tending to a constant value above 1 dpa. This is consistent with observations by Titov *et al.*, that bulk disorder peaks in β-Ga_2O_3 around 1 dpa irradiation dose.[52] We note that the while the modelled internal energy gain is significant, it does not account for any energy minimisation due to formation of planar defects such as dislocation loops or antiphase boundaries, which our CA model cannot predict. A similar trend of increasing disorder at low dpa that levels off above the 1 dpa threshold can be seen for the β-Ga_2O_3 vacancy evolution shown in Figure 6.2 **d)**. At each level of irradiation the total percentage of all core Ga-sites and O-sites that are left vacant are calculated, showing that an average of 25% of all atoms have been displaced to interstitial positions at high radiation doses. Our model also predicts a slightly larger percentage of Ga-sites being vacated during the irradiation process.

6.3.2 TEM analysis

Unlike the sample from Chapter 5, the lamella here was removed from a (020) bulk sample after the irradiation, rather than irradiating a TEM lamella. An SRIM simulation of the irradiation dose from 6×10^{15} cm^{-2} 2 MeV Ar ions to the bulk β-Ga$_2$O$_3$ sample is seen in Figure 6.3 **a)**. We can see that the estimated penetration depth for the ions is about 1.3 μm, and that the irradiation dose is not constant with respect to sample depth - reaching a peak close to the maximum ion penetration depth (at about 1 μm). Regardless, an irradiation dose of over 2 dpa is maintained throughout the irradiated layer, which is also the irradiation dose above which we observed deviations in the β-Ga$_2$O$_3$ diffraction pattern under 200 keV Ar ion irradiation in Chapter 5.

Because of the ion penetration depth, when removing the lamella from the bulk, the irradiation would be contained within a thin band of about 1.3 μm thickness next to the lamella's edge (which corresponds to the bulk sample's surface). This irradiated band is clearly visible under a TEM, distinct from the unirradiated β-Ga$_2$O$_3$, as shown in the dark field TEM image in Figure 6.3 **b)**. We can also confirm that the width of the band is about 1.3 μm as expected. Because of the bulk sample's orientation, the crystallographic direction perpendicular to the lamella edge would be $< 020 >$. Unlike a regular bright field image (formed as shown in Figure 5.1), a dark field TEM image is formed from the beam diffracted off a specific plane in the sample. As shown in the diagram in Figure 6.3 **c)**, inserting an objective aperture in the back-focal plane of the objective lens restricts all beams apart from the ones diffracted off of the (hkl) crystallographic plane in the sample (at angle $2\theta_{hkl}$). Therefore, the brightness in the image is higher closer to the Bragg condition. The dark field image in Figure 6.3 **b)** was taken at a reciprocal space vector $\mathbf{g}_{020}$, which means the image is formed from the beam diffracted off the (020) crystal plane in the β-Ga$_2$O$_3$ sample. In the image we see some lines/spots of high brightness within the unirradiated material, representing defect structures intrinsic to the bulk sample. A very high density of defects is visible in the irradiated band, with brighter spots closer to the surface (at low material depth). This could imply a higher density of planar defects such as dislocation loops close to the irradiated surface, however, individual defects are difficult to distinguish. A further exploration of possible defects, such as voids or precipitates may be necessary for a clear conclusion.

It is also notable, however, that unlike the sample examined in Chapter 5, here we do not observe any axis or reflection doubling between diffraction patterns taken within the irradiated band, compared to the unirradiated material. An example diffraction pattern taken from the irradiated band is shown in Figure 6.2 **d)**. The two marked reflections have an interplanar separation ratio of 0.56 and are at an angle of ϕ=90°. Using Equations (5.3) and (5.7), the reflections were identified as from the (020) and $(\bar{2}0\bar{2})$ planes respectively - within the $[10\bar{1}]$ zone axis of β-Ga$_2$O$_3$. There was also no discrepancy noted between the interplanar separations between diffraction patterns taken from irradiated and unirradiated areas of the sample (as would be indicated from Equation (5.3)). This is likely due to lattice relaxation after the irradiation process. Such relaxation could not have been observed in the sample examined in Chapter 5, due

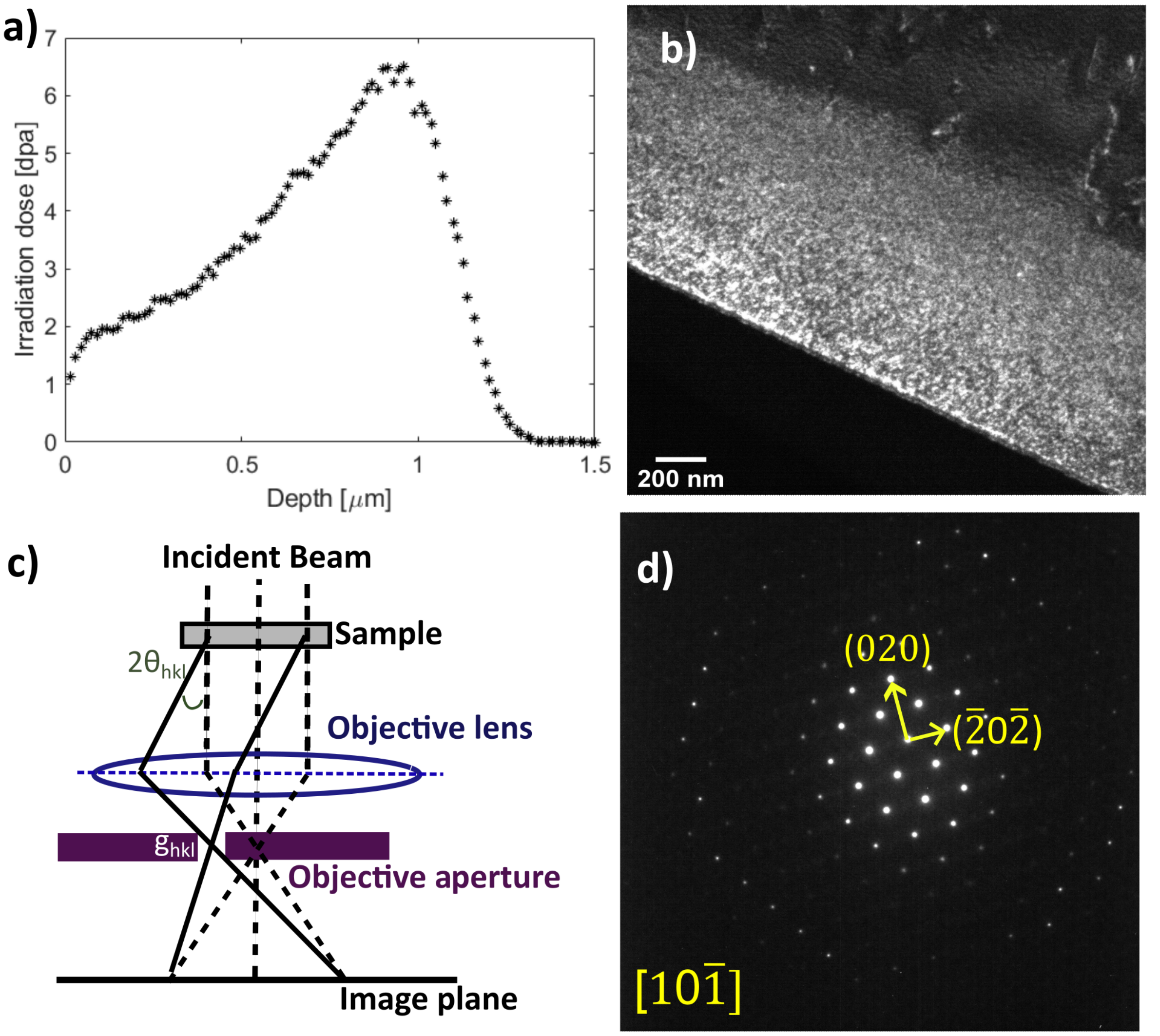

FIGURE 6.3. **a)** SRIM simulation of the irradiation dose with respect to sample depth from 6× 10^{15} cm^{-2} 2 MeV Ar ions; **b)** TEM dark field ($\mathbf{g}_{020}$) image of sample, irradiation band clearly visible; **c)** Diagram of dark field image formation in TEM; **d)** [$10\bar{1}$] zone axis diffraction pattern taken from irradiated band.

to the irradiation being carried out in situ. There is, in fact, a significant difference in geometry between the two samples. Since the sample discussed in this Chapter was irradiated as part of a bulk crystal, any lattice deformation in the irradiated layer would be difficult to maintain without the formation of a defective interlayer separating it from the unirradiated bulk. This was naturally not the case for the sample in Chapter 5, where defects were formed through the entirety of the lamella. This is another indication that the strain discussed in Chapter 5 is intrinsically connected to ion damage in a thin film.

Another major difference between the two samples remains the energy of the Ar ions used.

We can say that both during irradiation with 200 keV and 2 MeV Ar ions, β-Ga$_2$O$_3$ retains its crystalline nature and does not undergo polymorph transformation. However, the expected array of planar defects causing doubling within the diffraction pattern under irradiation with 200 keV, is not present when the ion energy is increased up to 2 MeV. It is important to clarify whether this discrepancy can be attributed at all to the difference in ion energies used, or if it may be fully due to the different sample geometries.

6.3.3 Effects of ion energy on defect production

We look to SRIM to explain this possible discrepancy in defect formation from irradiation with higher versus lower ion energies. Specifically, we consider the calculated energy lost per ion to ionisation (electronic energy loss) and to recoils within the material (nuclear energy loss). In Figure 6.4 **a)** we see a plot of the energy loss for 200 keV Ar ions incident on β-Ga$_2$O$_3$ as a function of material depth. As expected, we see that the contribution to nuclear energy loss dominates. As discussed by Hanson *et al.*,, this implies the formation of structural defects.[161] This is consistent with the experimental diffraction patterns from irradiated β-Ga$_2$O$_3$ under 200 keV Ar ions (discussed in Chapter 5), where such defects are the likely cause of reflection doubling.

In Figure 6.4 **b)**, the energy loss from an equivalent simulation is shown, using 500 keV Ar ion irradiation. At this ion energy the contributions from electronic and nuclear energy loss are in competition, with energy loss to ionisation dominating at low material depths, while energy loss to recoils being the larger contribution closer to the maximum ion penetration depth. We can already clearly see, however, that the loss contribution from ionisation is growing quicker with increasing ion energy than the contribution from atomic recoils. This is further illustrated by Figure 6.4 **c)**, where the energy loss from 2 MeV Ar ions is simulated. Electronic ion energy loss, which dominates for 2 MeV Ar ion irradiation of β-Ga$_2$O$_3$, we expect to be responsible for more localised defects.[160] This is also consistent with the TEM images of the irradiated band in Figure 6.3. From the figures we can also extract information about the spatial dependence of the two energy loss components. We see that electronic energy loss for Ar ions incident on β-Ga$_2$O$_3$ is highest near the surface, and progressively decreases with increased material depth. On the other hand, nuclear energy loss for Ar ions incident on β-Ga$_2$O$_3$ increases with material depth up to a peak close to the maximum ion penetration depth, after which it sharply decreases. From this one could assume the structural defects formed in β-Ga$_2$O$_3$ should form in highest quantities farther from the surface. However, such assertion does not account for the potential interplay between the two energy loss types in defect formation, and should be experimentally confirmed.

From our data, it is clear that 200 keV and 2 MeV Ar ions represent two distinct modes of defect formation in irradiated β-Ga$_2$O$_3$ - each governed by a different type of ion energetic loss. While Figure 6.5 **a)** relates to the expected damage formation in the sample from Chapter 5, Figure 6.5 **c)** corresponds to the expected damage formation for the sample investigated in

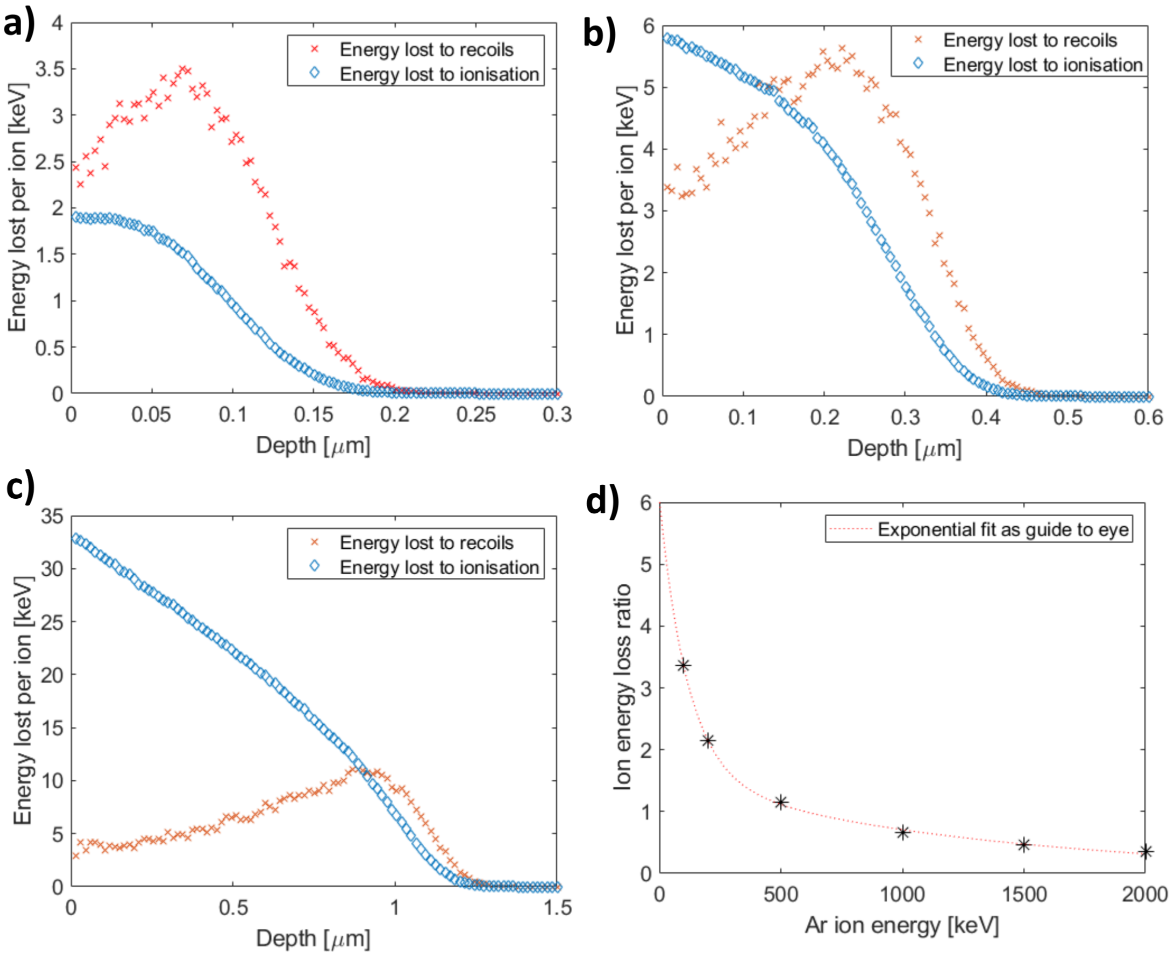

FIGURE 6.4. SRIM simulations of electronic and nuclear ion energy loss from **a)** 200 keV, **b)** 500 keV and **c)** 2 MeV Ar ions irradiating β-Ga_2O_3; **d)** Total ion energy loss ratio (nuclear/electronic) for different Ar ion energies used in β-Ga_2O_3 irradiation.

this Chapter. A clear difference can be seen in the types of damage formation that dominate in each case. For the in situ irradaited sample from Chapter 5 - energy loss to recoils dominates, which corresponds to the observed structural deformation. On the other hand, for the sample investigated in this Chapter, ionic energy loss dominates, relating to an expected high density of point-defects. From our SRIM calculations, we see how the interplay between nuclear and electronic energy loss evolves with the increase of incident ion energy.

For each SRIM simulation, the total energy loss for the two types (electronic and nuclear) was calculated as the area under each curve integrated via the trapezium rule. Then the ratio of total energy lost (nuclear loss against electronic loss) is plotted for 100 keV, 200 keV, 500 keV, 1 MeV, 1.5 MeV and 2 MeV Ar ion energies, shown in Figure 6.4 **d)**. The trend with increasing ion energy can be fitted to an exponential decay function. This tells us that larger structural damage

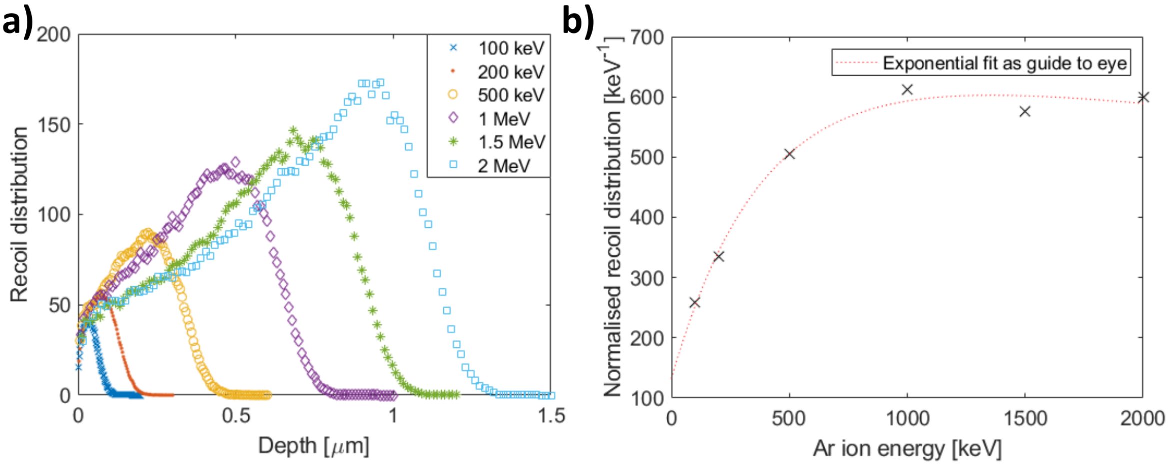

FIGURE 6.5. **a)** SRIM distribution of radiation-induced atomic recoils in β-Ga$_2$O$_3$ from varying energies of Ar ions; **b)** Recoils in β-Ga$_2$O$_3$ per keV of radiation for varying energies of incident Ar ions.

should be expected for lower ion energies. However, low ion energies also mean a significantly reduced ion penetration depth in the material (estimated to be around 90 nm for 100 keV Ar ions irradiating β-Ga$_2$O$_3$).

Another way to estimate the competing nature of electronic and nuclear ion energy loss from Ar ions irradiation of β-Ga$_2$O$_3$ is to consider the distribution of atomic recoils caused by the radiation, as calculated through SRIM. In Figure 6.5 **a)** we see the recoil distributions for all considered Ar ion energies. Since the total number of recoils as well as the penetration depth scale approximately linearly with increasing ion energy, a reasonable way to compare the number of produced recoils is to normalise them by the irradiating ion energy. A plot of the total recoils (each distribution integrated via the trapezium rule) normalised by the ion energy can be seen in Figure 6.5 **b)**, once again showing an exponential-type dependence on Ar ion energy. While from these plots the exact ion energy at which a switch occurs between the two modes of defect formation in β-Ga$_2$O$_3$ cannot be ascertained, they give a clear indication of the overall trend for damage depending on ion radiation energy. They may also serve comparatively, when used alongside irradiation experiments.

6.4 Conclusion

In this chapter we confirm peak disorder in β-Ga$_2$O$_3$ occurs at 1 dpa ion irradiation by means of a cellular automaton model. The model cannot account for planar defects disrupting the single-crystal nature of the examined material, however, can fully recreate the dynamics of the irradiation process. Our findings also suggest that irradiation causes significant reduction in the Ga-ion coordination number, which is likely to affect the material's electronic properties, such as core and valence states.[31] We further examine the defect formation in β-Ga_2O_3 from Ar ion irradiation depending on the ion energy. By means of a 2 MeV Ar ion irradiation and TEM experiment, we confirm a large density of defects in β-Ga_2O_3, but no reflection doubling in the diffraction patterns, as seen in a β-Ga_2O_3 sample irradiated under 200 keV Ar ions. This points to two different modes of defect formation in β-Ga_2O_3 for lower and higher energy incident ions. We further examine defect production in irradiated β-Ga_2O_3 through SRIM simulations by comparing the contributions of electronic and nuclear ion energy loss.

CHAPTER 7

CONCLUSIONS AND FUTURE WORK

Gallium oxide (Ga_2O_3) is an ultra-wide band gap material that is a promising candidate for power electronics applications. While its predicted breakdown field is superior to materials such as SiC or GaN, it has a significant drawback in its low anisotropic thermal conductivity, which can be a limiting factor for thermal management in potential devices. Ga_2O_3 is also notable for its polymorphism. While the β polymorph is the most stable and most well-known, interest in some of the other phases has also grown in recent years. It has been shown that changes in the local coordination environments for Ga-atoms are responsible for some of the differences in electronic properties between the different Ga_2O_3 polymorphs.

Bulk β-Ga_2O_3 substrates can be grown from the melt, producing commercial substrates as large as 2 inch wafers using the Czochralski method, and up to 6 inches in diameter using edge-defined film-fed growth. Whilst usually grown along the $< 010 >$ crystallographic direction, substrates are commercially available, sawed to have (100), (001) and ($\bar{2}01$) orientations. Due to the anisotropy of Ga_2O_3's thermal transport, the choice of orientation for a β-Ga_2O_3 substrate is significant. Commercially available β-Ga_2O_3 substrates can be n-type doped (both intentionally and unintentionally) or semi-insulating (implanted with deep acceptors). Polycrystalline β-Ga_2O_3 films, as well as other Ga_2O_3 polymorphs can be epitaxially grown, but are still not available as bulk substrates.

Various methods exist for incorporating β-Ga_2O_3 with higher thermal conductivity materials for the purpose of better thermal management in potential devices. Another benefit of using β-Ga_2O_3 in tandem with other materials is the possibility of making a p-n junction. This is because p-type β-Ga_2O_3 is impractical due to the material's poor hole mobility. In this thesis we discussed some of the main methods for adhesion of Ga_2O_3 to other substrates, outlining their pros and cons.

One possible method is the direct delamination of β-Ga_2O_3 along easy cleave planes such as (100) and (001), followed by direct dry transfer to a chosen substrate (forming a Van der Waals bonded interface). We have confirmed this also works along the (010) face of β-Ga_2O_3. The downsides of this method include limited area of the transferred flake (with width usually up to 20 microns), as well as a relatively high thermal boundary resistance (TBR). Our molecular dynamics simulations of β-Ga_2O_3 to (100) diamond Van der Waals heterojunctions indicated that the TBR may vary by up to 70%, depending on the β-Ga_2O_3 crystallographic orientation. The lowest TBR value for such a heterojunction was estimated as 48.6 ± 0.3 m^2KGW^{-1}, when the interface to (100) diamond was realised with the (100) face of 48.6 ± 0.3 m^2KGW^{-1}. Another issue with Van der Waals delamination of β-Ga_2O_3 flakes is the lack of control on the flake thickness, which may require further etching to achieve a layer under 200 nm.

Hydrophilic bonding is realised when both surfaces are functionalised with OH-grups, then brought into contact under ambient conditions, then finally annealed. Thermal dehydration causes the two materials to adhere through shared bonds with atomic oxygen. While such bonding of β-Ga_2O_3 to (100) diamond has been demonstrated, this method relies on both materials having ultra flat surfaces (with root mean squared (RMS) surface roughness below 0.5 nm). This affects the scaleability of this adhesion method. We have demonstrated hydrophilic bonding between (010) β-Ga_2O_3 (with 20 nm amorphous Al_2O_3 deposited on top via atomic layer deposition (ALD)) and Si (also with a 20 nm Al_2O_3 deposition). Having the hydrophilic bond be established between two amorphous layers reduces the risk of lattice mismatch affecting the bonding. We have further demonstrated that applying pressure during the bonding process can alleviate some of the requirements on surface roughness on the materials used - with the RMS surface roughness of the β-Ga_2O_3 used being as high as 1.7 nm.

Because of this, hydrophilic bonding has the potential to be a very beneficial adhesion method when only small-area bonding is required. Further study, however, may be required to confirm how good the thermal transport is across such an interface. We expect it to be significantly better than in the Van der Waals case due to the bond formation through the atomic oxygen. It also may be interesting to investigate whether the bonding strength or thermal boundary resistance depends on β-Ga_2O_3 crystallographic orientation (like we demonstrated it does in the Van der Waals case). There are certain barriers to simulating such a system using molecular dynamics, however. These are primarily related to the quality of gallium oxide potentials available. For example, reactive force potentials, which are commonly used to simulate the bonds between carbon and oxygen, are not compatible with any other potential type. Because of this, including gallium oxide in such a simulation is thus far not possible. Further first principles simulations of gallium oxide are needed for the construction of better, more robust and cross-compatible Ga_2O_3 potentials. We believe this to be a vital step to pushing this line of research forward.

Other notable methods for adhesion of β-Ga_2O_3 to high thermal conductivity include surface activated bonding, and usually involve an interlayer, such as amorphous Al_2O_3. Our molecular dynamics simulations of the TBR between β-Ga_2O_3 and amorphous Al_2O_3 were all within the range 0.9±0.3 m^2KGW^{-1} regardless of the Ga_2O_3 crystal orientation. This implies that a heterojunction between β-Ga_2O_3 and (100) diamond could have a TBR at least 3.6 times lower, if the interface was to be realised through a 10 nm amorphous Al_2O_3 interlayer, compared to a direct Van der Waals interface between the β-Ga_2O_3 and diamond. Another benefit to this type of surface activated bonding is that it can be carried out on an entire wafer. There's also a way to control the thickness of β-Ga_2O_3 one wishes to bond. This can be done via Smartcut - implantation of the β-Ga_2O_3 substrate with H-ions. The substrate can finally be cleaved along the plane of highest implanted ion density after annealing at 450°.

We also briefly discussed the possibility of growing diamond onto β-Ga_2O_3. Successful growth has been demonstrated on ($\bar{2}$01) β-Ga_2O_3, using 90 nm SiO_2 as interlayer to protect the substrate from damage during the growth process. We have observed spontaneous delamination of the grown diamond film and investigated the elemental makeup of the delamination using energy-dispersive x-ray spectroscopy (EDX). This was done to confirm whether or not β-Ga_2O_3 is being lifted off together with the diamond film during delamination. We observed negligible gallium signal from the EDX, which implies the diamond film is lifting on its own, and that this type of growth is not a suitable method for adhesion between β-Ga_2O_3 and diamond for the purpose of devices.

Based on the research we presented, large area (wafer-scale) bonding of gallium oxide to a higher thermal conductivity substrate is best accomplished using a thin interlayer (notably amorphous Al_2O_3). Extra care, however, needs to be taken when performing Smartcut, as H^+ ion irradiation could affect the electronic and structural properties of the gallium oxide. Our molecular dynamics simulations confirmed that the (010) is optimal for thermal transport in this type of adhesion - primarily due to it being the crystallographic orientation with the largest thermal conductivity regardless of sample thickness.

It should be noted that our molecular dynamics simulations on the thermal conductivity across β-Ga_2O_3 slabs of varying thickness confirmed that the way thermal conductivity varies with material thickness is dependent on β-Ga_2O_3's crystallographic orientation. This finding can help with the design of new device concepts for better thermal management. Both crystallographic orientation and sample thickness for Ga_2O_3 slabs used in potential devices should be considered.

There are still, however, significant ways this line of research can be taken further. While we established that TBR between β-Ga_2O_3 and other materials may vary significantly depending on the gallium oxide's crystallographic orientation, there are still many questions left unanswered. Our results do not seem to suggest there is a single crystallographic orientation in β-Ga_2O_3 that provides the lowest TBR in all cases. Thus, one may ask the following questions. What are the main factors which determine the TBR value for β-Ga_2O_3 to other materials? Is the type of bonding/adhesion the most important factor? What are the unique emerging interfacial phonon modes between β-Ga_2O_3 and other materials? What is their relative importance compared to the general phonon overlap between the two materials? We believe that in order to extract the most benefit from the anisotropic thermal properties of β-Ga_2O_3 for future practical devices, further research is required. In the author's opinion, ab initio investigation into the different interfacial phonon modes between β-Ga_2O_3 and other materials would be a highly impactful work in the field.

Of course, such work can also be extended beyond the β phase of Ga_2O_3. So far, reports on the thermal properties of Ga_2O_3 polymorphs have been confined to the β phase (with the exception of one recent work simulating the thermal conductivity of α-Ga_2O_3, showing it to also be anisotropic. Future work on the topic should include molecular dynamics simulations of other Ga_2O_3 polymorphs. We believe the study of other polymorphs to become increasingly important in the future - due to the interesting properties of some polymorphs (such as κ), as well as the ability to grow thin films of them for the purpose of potential devices.

Some potential research into other Ga_2O_3 polymorphs includes thermal conductivity measurements for different crystallographic orientations and material thicknesses, as well as simulated TBRs across material interfaces. In order for this to be accomplished, the lack of suitable and well-tested interatomic potentials for gallium oxides should be addressed. While potentials for the β phase are now available, this is still not the case for the other Ga_2O_3 polymorphs. Such potentials, however, could be extracted from density functional theory (DFT) simulations of the individual polymorphs. We propose that DFT would be a good auxiliary tool in the advancement of research in the field of gallium oxides. Despite our limitations, we were able to simulate interfaces between β-Ga_2O_3 and amorphous Ga_2O_3. We found the TBR across such interfaces did vary depending on the orientation of the β-Ga_2O_3 - estimated as 0.9 ± 0.3 m^2KGW^{-1} along the $<001>$ direction of β-Ga_2O_3, and 0.5 ± 0.3 m^2KGW^{-1} along the $<010>$ direction of β-Ga_2O_3.

The study of polymorphism in Ga_2O_3 is also especially important considering the growth and deposition of thin films, where the effects of defects and polycrystallinity are likely to have significant effects on the film's properties. A notable example of this is the method for thin film Ga_2O_3 deposition, that was explored in this thesis, relying on the spontaneous oxidisation of liquid gallium in air, forming an outer layer of Ga_2O_3. This passivation layer can then be delaminated onto a substrate, providing a large area oxide skin. We demonstrated such deposition on a Si substrate with thermal oxide (SiO_2). The deposition was finally annealed at 250° in oxygen, which has been suggested to help the film crystallise. We measured the valence band offset between the film and the SiO_2 substrate as 0.1 eV. This implies a -4.3 eV valence band offset of our deposited Ga_2O_3 with respect to Si, differing by 0.8 eV from the offset value measured between PLD-grown β-Ga_2O_3 and Si. This implies that our Ga_2O_3 is forming a type II alignment with silicon (whereas PLD-grown β-Ga_2O_3 has type I alignment to Si). We also estimated our thin film Ga_2O_3 to form a blocking interface with diamond, providing an energetic barrier for minority carriers across a potential p-n heterojunction.

The reason behind this significant difference between our deposited film and PLD-grown

β-Ga_2O_3 is still unconfirmed. While it is likely due to specific features in the deposited film's structure, we have yet to obtain conclusive information about what that structure might be. Due to the film's thin film (and likely defective) nature, no signal was observed when probing the prepared sample using XRD, GIXRD and EBSD. We suspect the energetic differences are caused by local changes in stoichiometry at the boundaries between individual grains, or possibly due to the presence of γ-like defects. Further study (possibly using HRTEM), however, would be needed to confirm this.

The thermal properties of our deposited film were also investigated. We performed transient thermoreflectance on a sample with and without the Ga_2O_3 deposition. We estimated the out-of-plane thermal conductivity of our deposited Ga_2O_3 as 3 $Wm^{-1}K^{-1}$, which is double the reported thermal conductivity of a pollycrystalline ALD β-Ga_2O_3 of comparable thickness. While no reports have been made on the thermal conductivity of isolated κ-Ga_2O_3, our result may be an indication that the thermal conductivity of the κ phase is higher than that of the conventional β.

The study of structural defects in Ga_2O_3 and the changes in properties they may induce, is also very important when considering possible irradiation effects in the material. For β-Ga_2O_3, radiation effects are important for some potential device applications, including for telecommunication satellites. Ion irradiation effects, specifically, are also relevant when considering ion implantation or doping of β-Ga_2O_3. There is also an interesting intersection of ion irradiation on Ga_2O_3 and the material's polymorphism. Research has shown, for example, that α-Ga_2O_3 is significantly more resistant to damage accumulation from ion irradiation than the β polymorph. Also, as discussed above, a primary difference between the different Ga_2O_3 polymorphs, as well as their properties, is related to the local coordination environments of Ga-atoms. Thus, structural changes to the material from ion irradiation could have significant consequences on its electronic and other properties.

We investigated and discussed the structural changes in thin film (~160 nm thick) β-Ga_2O_3 occurring due to in situ ion irradiation from 200 keV Ar ions inside a transmission electron microscope (TEM). We observed that while the structure of the irradiated sample remained unmistakably that of crystalline β-Ga_2O_3, there was a distinct progressive anisotropic shrinkage of lattice dimensions throughout the irradiation process, most significant at lower levels of irradiation.

Above an irradiation dose of 2 displacements per atom (dpa), we observed extra reflections in the material's diffraction patterns for two separate zone axes. These reflections could not be explained by retained order within different β-Ga_2O_3 sublattices, nor did they indicate an emerging polymorph transition. We concluded that their presence is due to ordering of complex planar defects. It is notable, however, that neither such extra reflections, nor progressive lattice shrinkage were observed even at higher irradiation doses (up to 6 dpa at the base of the irradiation layer) during a follow up irradiation experiment on β-Ga_2O_3 using 2 MeV Ar ion radiation. The reasons for this are likely twofold. On the one hand, the follow up irradiation was carried out on a bulk sample, where the same types of deformation as in a thin film are not possible. On the other hand, despite the visibly large density of defects in the sample irradiated with 2 MeV Ar ions, we expect that the higher ion energy corresponds to a different mode of defect formation from the initial in situ experiment. In the end, the exact cause of the extra reflections observed under in situ irradiation of thin film β-Ga_2O_3 still need to be confirmed. Future work should aim to recreate the in situ experiment, focusing on performing Dark Field analysis on any emerging reflections in order to clarify their exact origin, thus bringing further understanding of how defect formation in β-Ga_2O_3 works.

We discussed the mechanisms for defect production from ion irradiation, focusing on the interplay between nuclear and electronic ion energy loss. Ion energy absorbed by the lattice (nuclei) leads to atomic displacements from elastic scattering, whereas ion energy absorbed by the electrons (which is usually more significant at higher ion energies) is mostly responsible for localised ionisation damage. In some cases, electronic ion energy loss has also been connected to defect recovery. We used stopping range of ions in matter (SRIM) simulations to examine the changes in relative contributions from nuclear and electronic ion energy loss within β-Ga_2O_3, as incident Ar ion energy increases. Our simulations confirm two separate modes of damage formation in β-Ga_2O_3 from ion irradiation, although the exact point of crossover cannot be ascertained without further experiments. We find the largest contributions from nuclear energy loss consistently being concentrated near the base of the irradiation layer, while the largest contributions from electronic ion energy loss is always concentrated on the irradiated sample's surface. Relatively equal contributions from both energy loss types was found when simulating 500 keV Ar ion irradiation on β-Ga_2O_3.

Future research on ion irradiation in β-Ga_2O_3 should focus on identifying the relative contributions/densities of various defect types, especially in samples with high defect density, such as discussed in this thesis. This would be a great way to extend the present study as it could help link the expected defect breakdown in β-Ga_2O_3 from irradiation of a specified ion energy. Dislocation loops, for example, can be identified through image contrast analysis. However, further work related to performing this reliably on images from samples with high defect densities is necessary. A thorough classification work of defect types, including formation, induced change in properties, identification and annealing, would be highly impactful.

Finally, we proposed a cellular automaton model of the atomic displacements within β-Ga_2O_3 due to an increasing dose of ion irradiation. While our model is limited to a single-crystalline network, and hence cannot account for more complex disruptions to the crystalline structure of the material (such as the planar defects mentioned above), it serves as a valuable tool that can reconstruct the full dynamics of the irradiation process. Our model confirmed that peak bulk disorder in β-Ga_2O_3 occurs at 1 dpa irradiation dose. It also suggested a significant reduction in the average Ga-atom coordination number resulting from the ion irradiation. Because of this, similarities could be drawn between this damaged β-Ga_2O_3 phase and the γ polymorph, which is the only known phase of Ga_2O_3 with an average Ga-site coordination number lower than in pure β-Ga_2O_3. This may also be related to the γ-phase-like defects observed near the interfaces of different Ga_2O_3 polymorphs.

In conclusion, this thesis details valuable work in the fields of material integration, anisotropy and radiation effects in β-Ga_2O_3. Its main contributions to knowledge include a study of anisotropic thermal transport through bulk β-Ga_2O_3 and across interfaces, characterisation of some bonding/adhesion methods including from liquid metal thin film deposition, as well as an examination of structural changes in the material due to ion irradiation. Here we also outlined some valuable pieces of future research that can build on the work presented throughout the thesis. It is the author's opinion that the most impactful future work in the field of Ga_2O_3 for high power electronics would include extensive first principles investigations. Highly disruptive new work would include a study of interfacial phonon modes, defect formation, and the creation and testing of robust potentials that can model the full range of properties of gallium oxides (including other polymorphs).

APPENDIX A

CODE AND INPUT FILES

In this appendix, some of the code used for the simulation work done in this thesis is given. This includes the input files for key LAMMPS calculations, as presented in Chapter 4, as well as the code written for the cellular automaton model presented in Chapter 6.

A.1 LAMMPS code

Examples of the LAMMPS submission files used for thermal conductivity and across-interface thermal transport calculations are given here. The first file (shown below) was used to calculate the thermal conductivity of a (100) β-Ga_2O_3 slab of approximate thickness of 120 nm. Submission files of this type were used to estimate the change in β-Ga_2O_3 thermal conductivity with increasing material thickness along different crystallographic orientations.

```
units           metal
boundary        p p p
atom_style      charge
lattice         custom 1.0 &
          a1     12.2299995422       0.0000000000        0.0000000000 &
          a2       0.0000000000       3.0399999619        0.0000000000 &
          a3      -1.3736609922       0.0000000000        5.6349851545 &
          basis         0.090399995       0.000000000        0.794799939 &
          basis         0.909599983       0.000000000        0.205199986 &
          basis         0.590399966       0.500000000        0.794799939 &
          basis         0.409599983       0.500000000        0.205199986 &
          basis         0.341399978       0.000000000        0.685699987 &
          basis         0.658599936       0.000000000        0.314299981 &
```

```
         basis        0.841400056       0.500000000       0.685699987 &
         basis        0.158599995       0.500000000       0.314299981 &
              basis        0.167400004       0.000000000       0.101099994 &
              basis        0.832599951       0.000000000       0.898899984 &
              basis        0.667400043       0.500000000       0.101099994 &
              basis        0.332599990       0.500000000       0.898899984 &
              basis        0.495700006      -0.000000000       0.255299985 &
              basis        0.504299988       0.000000000       0.744700003 &
              basis        0.995699967       0.500000000       0.255299985 &
              basis        0.004299993       0.500000000       0.744700003 &
              basis        0.827900015       0.000000000       0.436500000 &
              basis        0.172100006       0.000000000       0.563499967 &
              basis        0.327899937       0.500000000       0.436500000 &
              basis        0.672100016       0.500000000       0.56349996
region         main block -50 50 -10 10 0 10
create_box     2 main
mass               1 69.723
mass           2 15.999
create_atoms   2 region main &
basis 1 1 &
basis 2 1 &
basis 3 1 &
basis 4 1 &
basis 5 1 &
basis 6 1 &
basis 7 1 &
basis 8 1 &
basis 9 2 &
basis 10 2 &
basis 11 2 &
basis 12 2 &
basis 13 2 &
basis 14 2 &
basis 15 2 &
basis 16 2 &
basis 17 2 &
basis 18 2 &
basis 19 2 &
basis 20 2 &

set       type 1 charge 3 #2.67
set       type 2 charge -2 #-2.51
pair_style     born/coul/dsf/cs 0.2 16.0
```

```
pair_coeff   * * 0.0 16.0 0.0 0.0 0.0
pair_coeff    1 2 907.89 0.345 0.0 10.0 0.0
pair_coeff    2 2 22764.0 0.149 0.0 0.0 0.0
region       cold1 block -50 -49 -10 10 0 10
region       cold2 block 49 50 -10 10 0 10
region       hot   block -1 1 -10 10 0 10
compute       Thot all temp/region hot
compute       Tcold2 all temp/region cold2
compute       Tcold1 all temp/region cold1
timestep      0.001
#equilibration

thermo        1
minimize     1.0e-10 1.0e-10 100000 100000
reset_timestep 0
#write_data  1.dat
velocity      all create 300.0 4928459 dist gaussian
fix           1 all nvt temp 300 300 0.002
run           100000
unfix             1
#in.heat conductivity calculation part1
fix               1 all nve
fix           hot all heat 1 20.0 region hot
fix           cold2 all heat 1 -10.0 region cold2
fix           cold1 all heat 1 -10.0 region cold1
thermo_style  custom step temp c_Tcold1 c_Thot c_Tcold2
thermo          1000
run           600000
#actual calculation
compute      ke all ke/atom
variable temp atom c_ke/1.5

compute       layers all chunk/atom bin/1d x lower 0.01 units reduced
fix               2 all ave/chunk 10 100 1000 layers v_temp temp file
    profile.heat

run           10000
```

The next example LAMMPS submission file is of a calculation of the temperature profile across a Van der Waals bonded (100) β-Ga_2O_3 to (100) diamond heterojunction. Similar files were used to estimate the thermal boundary resistance across Ga_2O_3-material interfaces for different Ga_2O_3 crystallographic orientations. The materials considered for interfaces with

β-Ga_2O_3 included (100) diamond, amorphous Al_2O_3 and amorphous Ga_2O_3.

```
units         metal
boundary      s s s
atom_style    charge
lattice       custom 1.0 &
         a1     12.2299995422       0.0000000000       0.0000000000 &
         a2        0.0000000000       3.0399999619       0.0000000000 &
         a3       -1.3736609922       0.0000000000       5.6349851545 &
         basis         0.090399995       0.000000000       0.794799939 &
         basis         0.909599983       0.000000000       0.205199986 &
         basis         0.590399966       0.500000000       0.794799939 &
         basis         0.409599983       0.500000000       0.205199986 &
         basis         0.341399978       0.000000000       0.685699987 &
         basis         0.658599936       0.000000000       0.314299981 &
         basis         0.841400056       0.500000000       0.685699987 &
         basis         0.158599995       0.500000000       0.314299981 &
             basis         0.167400004       0.000000000       0.101099994 &
             basis         0.832599951       0.000000000       0.898899984 &
             basis         0.667400043       0.500000000       0.101099994 &
             basis         0.332599990       0.500000000       0.898899984 &
             basis         0.495700006      -0.000000000       0.255299985 &
             basis         0.504299988       0.000000000       0.744700003 &
             basis         0.995699967       0.500000000       0.255299985 &
             basis         0.004299993       0.500000000       0.744700003 &
             basis         0.827900015       0.000000000       0.436500000 &
             basis         0.172100006       0.000000000       0.563499967 &
             basis         0.327899937       0.500000000       0.436500000 &
             basis         0.672100016       0.500000000       0.563499967
region       main block -9.89 9.88 -10 10 -5 5
region       gao block 0.01 9.88 -10 10 -5 5
region       dia1 block -9.89 -0.02 -10 10 -5 5
region       cold block -9.88 -9.48 -10 10 -5 5
region       hot block 9.48 9.88 -10 10 -5 5
create_box    3 main
mass              1 69.723
mass         2 15.999
mass              3 12.0107
create_atoms  2 region gao &
basis 1 1 &
basis 2 1 &
basis 3 1 &
basis 4 1 &
basis 5 1 &
basis 6 1 &
basis 7 1 &
basis 8 1 &
basis 9 2 &
basis 10 2 &
basis 11 2 &
basis 12 2 &
basis 13 2 &
basis 14 2 &
basis 15 2 &
basis 16 2 &
basis 17 2 &
basis 18 2 &
basis 19 2 &
basis 20 2
lattice       diamond 3.567
create_atoms  3 region dia1
set      type 1 charge 3 #2.67
set      type 2 charge -2 #-2.51

pair_style    hybrid meam/c born/coul/dsf/cs 0.2 10.0 lj/cut 10.0
pair_coeff   1 3 lj/cut 0.00226302317 4.10839786291
pair_coeff   2 3 lj/cut 0.00086047202 3.67130766894
pair_coeff   1 1 born/coul/dsf/cs 0.0 16.0 0.0 0.0 0.0
pair_coeff   * * meam/c library1.meam C SiC.meam NULL NULL C
pair_coeff    1 2 born/coul/dsf/cs 907.89 0.345 0.0 10.0 0.0
pair_coeff    2 2 born/coul/dsf/cs 22764.0 0.149 0.0 0.0 0.0
timestep      0.001
compute       Thot all temp/region hot
compute       Tcold all temp/region cold
#equilibration

thermo        1
minimize     1.0e-10 1.0e-10 100000 100000
reset_timestep 0
dump start all xyz 80000 start.xyz
velocity      all create 300.0 4928459 dist gaussian
fix           1 all nvt temp 300 300 0.002
run           100000
unfix             1
#in.heat conductivity calculation part1
fix               1 all nve
fix           hot all heat 1 1.0 region hot
fix            cold all heat 1 -1.0 region cold
thermo_style   custom step temp c_Tcold c_Thot
thermo           1000
run            600000
#actual calculation
compute       ke all ke/atom
variable temp atom c_ke/1.5
dump end all xyz 8000 end.xyz
compute        layers all chunk/atom bin/1d x lower 0.01 units reduced
fix                2 all ave/chunk 10 100 1000 layers v_temp temp file
    profile.heat


run            10000
```

A.2 Cellular automaton code

The Matlab code written for the cellular automaton model of ion irradiation evolution in β-Ga_2O_3 is presented here. First comes the general script that is executed in order to simulate the irradiation process. Some of the functions that it uses are expanded on further.

```
fa_BuildGlobals;
Tbl = importfile("beta_positions_table.txt", [1, Inf]);
%file includes all site positions in the unit cell

T1 = table2array(Tbl);

% -------------------------------
    T0 = T1;
    d0=[12.2139997482, 3.0371000767 5.6300086886];
% -------------------------------

mult =[0   12.2139997482     0.0000000000      0.0000000000 0.0     0.0      0.0
      0    0.0000000000      3.0371000767      0.0000000000 0.0     0.0      0.0
      0   -1.3859890746      0.0000000000      5.6300086886 0.0     0.0
          0.0];

   % build dimx+1 x dimx+1

   dimx=9;

for kkk= 1:3
```

```
    T2 = mult(kkk,:);
    sz = size(T1);
    for kk = 1:dimx
        T3 = kk*T2;
        for k=1:sz(1)
            T1(sz(1)*(kk)+k,:) = T1(k,:)+T3;
        end
    end
end

global indReduc;

cutoff=1;
% -------------------------------
m1=[0,0,0];
M1=[(12.2139997482)*(dimx+1), 3.0371000767*(dimx+1), 5.6300086886*(dimx+1)];
L=m1+cutoff*d0;  U=M1-cutoff*d0;
% -------------------------------


fa_Process_Tbl(T1);

global Cc;
global A;
global B;
global R;

% -------------------------------
AA=[[A.curNr]',[A.x]',[A.y]',[A.z]'];
AA1=AA(AA(:,2)>=L(1) & AA(:,2)<U(1) & AA(:,3)>=L(2) & AA(:,3)<U(2) &
    AA(:,4)>=L(3) & AA(:,4)<U(3),:);
indReduc = AA1(:,1);
% -------------------------------

global t;
global steps;
t = 0.1;
steps = 25;

fa_fillIn_B()

save('unit_cell4x4','T1','Cc','A','B','R','t','steps','indReduc');

%%
```

```
xx=[0:1:steps]*t;
CorN=[R.coordGaReduc]; %coordination number for Ga-ions
Enpatom=[R.SumEvReduc]./numel(indReduc); % internal energy per atom
VacGa=100*[R.VacReducGa]./(numel(indReduc)*0.4); %Ga-site vacancies
VacO=100*[R.VacReducO]./(numel(indReduc)*0.6); %O-site vacancies
Vacancies=100*([R.VacReducGa]+[R.VacReducO])./numel(indReduc);
%Total vacancies
%%
```

The following function scripts defines the global variables that are used throughout all functions and scripts. These include the cell grid and the structure information recorded for each site (in structure matrix **A**). It also creates the structure matrix **B**, which contains information about the occupancy of each cell across all timesteps, as well as the matrix **R**, which is a subset of **B** with data from sites close to the edge of the simulation ignored.

```
% Build Globals

function fa_BuildGlobals

global Cc;
Cc = struct('type', [],...
            'indx', [],...
            'dist', [],...
            'colr', []);


Cc(1).type = 'I-I'; Cc(1).indx = [1 1]; Cc(1).dist = 2.5; Cc(1).colr = 'b';
Cc(2).type = 'I-G'; Cc(2).indx = [1 2]; Cc(2).dist = 2.5; Cc(2).colr = 'k';
Cc(3).type = 'I-O'; Cc(3).indx = [1 3]; Cc(3).dist = 2.5; Cc(3).colr = 'c';

Cc(4).type = 'G-G'; Cc(4).indx = [2 2]; Cc(4).dist = 2.6; Cc(4).colr = 'g';
Cc(5).type = 'G-O'; Cc(5).indx = [2 3]; Cc(5).dist = 2.6; Cc(5).colr = 'm';

Cc(6).type = 'O-O'; Cc(6).indx = [3 3]; Cc(6).dist = 2.6; Cc(6).colr = 'r';


%  Structure A contains info about the crystal lattice,
% whose change in radiation we will model.
%  A contains only constant data, we fill a separate structure B,
% which will change over time.
%-------------------------------
global A;
```

```
A = struct('curNr', [],...
           'energy', [],...
           'pType', [],...
           'pIndx', [],...
           'x', [],...
           'y', [],...
           'z', [],...
           'colour', [],...
           'tetrahedral', [],...
           'octahedral', [],...
           'c', [],...
           'cType', [],...
           'cDist', [],...
           'cColr', []);        % includes ID,
% possible enrgies for each site, site type, coords,
% information about neighbouring sites
global B;
B = struct('ID', [],...
           'oldID', {},...
           'pOcup', [],...
           'p0_eV', [],...
           'cType', [],...
           'coordT', []); % includes ID,
% list of IDs current occupying atom has been in,
% occupancy type, energy, list of neighbours occupancy types

global R;
R = struct('SumEv', [], 'coordGa', [],...
           'SumEvReduc',[],'coordGaReduc',[],...
           'VacReducGa',[],'VacReduc0',[]); % Structure for results,
% Reduc for including boundary conditions

end
```

The next function fills out the data reference matrix structure **A**.

```
function fa_Process_Tbl(data00)
global Cc;
global A;
global B;

    I = data00(:,1);
    X = data00(:,2);
    Y = data00(:,3);
    Z = data00(:,4);

    Iu = unique(I);

    PType{Iu(1)} = 'I';
    PType{Iu(2)} = 'G';
    PType{Iu(3)} = 'O';

    Energy(:,1) = data00(:,5);
    Energy(:,2) = data00(:,6);
    Energy(:,3) = data00(:,7);

% -------------
% Calc distances
% --------------
    N = numel(I);
    D = zeros(N);
    Dc= zeros(N);
    %
    for k = 1:N-1
        for kk = k+1:N
            % get distance
            d = sqrt( (X(kk)-X(k))^2+(Y(kk)-Y(k))^2+(Z(kk)-Z(k))^2);
            D(k,kk) = d;

            % find the case
            if ((I(k)==1) && (I(kk)==1))
                ind = 1;
            elseif ((I(k)==1) && (I(kk)==2))
                ind = 2;
            elseif ((I(k)==1) && (I(kk)==3))
                ind = 3;
            elseif ((I(k)==2) && (I(kk)==2))
                ind = 4;
            elseif ((I(k)==2) && (I(kk)==3))
                ind = 5;
            elseif ((I(k)==3) && (I(kk)==3))
                ind = 6;
            end

            % deside on connection
            if d <= Cc(ind).dist
```

```
                dc = 1;
            else
                dc = 0;
            end
            Dc(k,kk) = dc;
        end
    end

    DD = D + D';
    DDc = Dc + Dc';
% --------------------------------------------
    N = numel(I);
    col_str = 'bgrcmky';
    % set rhe first moment in time (before irr)
    tt = 1;

    for k=1:N
        A(k,tt).curNr = k;            % current Nr in the list
        A(k,tt).energy = [];          %
        A(k,tt).pType = PType(I(k));  % current type (string)
        A(k,tt).pIndx = I(k);         % current type (index)
        % 3D coordinates
        A(k,tt).x = X(k);    A(k,tt).y = Y(k);    A(k,tt).z = Z(k);
        % the colour of the node when plotting
        cl = col_str(I(k));
        A(k,tt).colour = cl;
        % Collect current connections
        ConnRow = find(DDc(k,:));    % connections indecies
        DistRow = DD(k,ConnRow);     % connections distances
        % get the colour of the connections
        n = numel(ConnRow);
        cCol = '';
        ind = [];
        for kk=1:n
            j = ConnRow(kk);
            % find the case
            if ((I(k)==1) && (I(j)==1))
                ind = 1;
            elseif ((I(k)==1) && (I(j)==2))
                ind = 2;
            elseif ((I(k)==1) && (I(j)==3))
                ind = 3;
            elseif ((I(k)==2) && (I(j)==2))
            ind = 4;
        elseif ((I(k)==2) && (I(j)==3))
            ind = 5;
        elseif ((I(k)==3) && (I(j)==3))
            ind = 6;
        end
        % set connection's colour
        cCol = [cCol Cc(ind).colr];
    end

    A(k,tt).c = ConnRow;             % set connections
    A(k,tt).cType = I(ConnRow);      % connections types
    A(k,tt).cDist = DistRow;         % set connection distances
    A(k,tt).cColr = cCol;            % set connection's distsnce

end

% Let's talk about energy
for k = 1: numel(A)
    A(k,1).energy = [Energy(k,1),Energy(k,2),Energy(k,3)];
end

% fillIn tetrahedral
for k=1:numel(A)
    if A(k,1).energy(2)==-53.3
        A(k,1).tetrahedral=1;
        A(k,1).octahedral=0;
    elseif A(k,1).energy(2)<0
        A(k,1).tetrahedral=0;
        A(k,1).octahedral=1;
    else
       A(k,1).tetrahedral=0;
        A(k,1).octahedral=0;
    end
end
% then fill in the energy using translations PrOpPerLy
for k = 1: numel(A)
    B(k,1).ID = A(k,1).curNr;
    B(k,1).oldID = {};
    switch A(k,1).pIndx
        case 1
            wv = 0;
            ev = A(k,1).energy(1);
            case 2
                wv = 2;
                ev = A(k,1).energy(2);
            case 3
                wv = 3;
                ev = A(k,1).energy(3);
        end
        B(k,1).p0cup = wv;
        B(k,1).p0_eV = ev;
        x = A(k,1).cType;
        B(k,1).coordT = [numel(x(x==1)),numel(x(x==2)),numel(x(x==3))];
    end

disp('Done - fa_Process_Tbl...');

return;
end
```

The following function fills out the global structure matrix **B**.

```
function fa_fillIn_B()
% Fill in B many time steps
global A;
global B;
global R;
global t;
global steps;
global indReduc;
% ck   - current stage of B
% fk   - future stage of B

    sz = size(B);

    ck = sz(2);

    R(ck).SumEv = sum([B(:,ck).p0_eV]);
    R(ck).coordGa = fa_GaCoord(A, B(:,ck));

    R(ck).SumEvReduc = sum([B(indReduc,ck).p0_eV]);
    R(ck).coordGaReduc = fa_GaCoord(A, B(:,ck), indReduc);

    R(ck).VacReducGa=0;
    R(ck).VacReduc0=0;
```

```
fa_ExpCoord(A, B(:,ck), 2, 3, 'test01');

while ck<=steps

    fk = ck+1;
    b = B(:,ck);

    for k=1:sz(1)        % loop for every node
       bb = b(k);
       if bb.pOcup==0
          continue;
       end
       a = A(k,1);
       % ------------
       n = numel(a.c);

       site_type = a.pIndx;          % site type
       idx = [];
       switch site_type
        case 1
            da = true;
            if bb.pOcup==2
               idx = (a.cType==1) | (a.cType==2);
            elseif bb.pOcup==3
               idx = (a.cType==1) | (a.cType==3);
            else
               da = false;
               idx = [];
            end
        case 2
           da = true;
           idx = (a.cType==1) | (a.cType==2);
        case 3
           da = true;
           idx = (a.cType==1) | (a.cType==3);
       end
       if da
           neigb = a.c(idx);
           av_neigb0 = neigb([b(neigb,1).pOcup]==0);
           n = numel(av_neigb0);

           av_neigb = [];    jjk = 0;
```

```
                for j=1:n
                    jj = av_neigb0(j);
                    if A(jj,1).pIndx==1
                        x_list = A(jj,1).c;

                        y_list = [];   jk = 0;
                        for jjj=1: numel(x_list)
                            if (A(x_list(jjj),1).pIndx==1) && ~(x_list(jjj)==k)
                                jk = jk+1;
                                y_list(jk) = x_list(jjj);
                            end
                        end

                        z = find([b(y_list).pOcup]==bb.pOcup, 1);
                        if ~isempty(z)
                            vliza = false;
                        else
                            vliza = true;
                        end
                    else
                        vliza = true;
                    end
                    if vliza
                        jjk = jjk+1;
                        av_neigb(jjk) = jj;
                    end
                end

                if ~isempty(av_neigb)
                    ev = [];
                    for j = 1:numel(av_neigb)
                        ev(j) = A(av_neigb(j),1).energy(bb.pOcup); % energy
                    end
                    % ------------

                    u = sort(unique(ev),'ascend');
                    m = u(1);
                    I = find(ev==m);
                    imax = numel(I);
                    ii = randi(imax);

                    outID = av_neigb(ii);
                    in_ID = a.curNr;

                    if rand<=t
                        b(outID,1).pOcup = b(in_ID,1).pOcup;
                        b(outID,1).pO_eV = m;
                        b(outID,1).oldID = [b(outID,1).oldID in_ID];

                        b(in_ID,1).pOcup = 0;
                        b(in_ID,1).pO_eV = 0;
                    end
                end
            end
        end

        B(:,fk) = b;

        R(fk).SumEv = sum([b.pO_eV]);
        R(fk).coordGa = fa_GaCoord(A, b);

        R(fk).SumEvReduc = sum([b(indReduc).pO_eV]);
        R(fk).coordGaReduc = fa_GaCoord(A, b, indReduc);

        R(fk).VacReducGa = fa_VaCount(A,b,indReduc,2);
        R(fk).VacReducO = fa_VaCount(A,b, indReduc,3);

        Nstr = num2str(fk);
        if numel(Nstr)==1
            Nstr = ['0' Nstr];
        end

            fa_ExpCoord(A, b, 2, 3, ['test' Nstr]);

        ck = ck+1;
    end

disp('Done, Done Fill in B ');
end
```

The next function calculates the average coordination number for an element.

```
% Coordination number counter
% ------------------------------------
%  fa_GaCoord(A,b, p1, p2)
% FUNCTION
%      Calculates average coordination number
% INPUT
%      A     - lattice structure
%      b     - current timestep structure
%      p1    - code of the leading element
%      p2    - code of the neighbours counted
%
% OUTPUT:
%      Q     - average coordination number

function Q = fa_GaCoord(A, b, indx, p1, p2)
%
if nargin<2
    Q = [];
    disp('not enough input parameters!');
    return;
end

n = numel(b);
if nargin<3;      indx = [];     end
if isempty(indx)
    indx = 1:n;
else
    n = numel(indx);
end

if nargin<4;      p1 = [];      end
if isempty(p1);   p1 = 2;       end
%
if nargin<5;      p2 = [];      end
if isempty(p2);   p2 = 3;       end
%

    CntGa = 0;
    Cnt3 = 0;
    for kk = 1:n
        k = indx(kk);
        bb = b(k);
        if bb.pOcup==p1
            CntGa = CntGa+1;
            a = A(k,1);
            nn = numel(a.c);
            if ~isempty(nn)
                x = [b(a.c).p0cup];
                y = find(x==p2);
                Cnt3 = Cnt3 + numel(y);
            end
        end
    end

    Q = Cnt3/CntGa;

return;
end
```

The final function presented here exports the atomic coordinates of the material at the end of the irradiation simulation.

```
% Vacancy counter
% ------------------------------
%  fa_VacCount(A,b,indx,p1)
% FUNCTION
%      Calculates average coordination number
% INPUT
%      A     - latise structure
%      b     - current timestep structure
%
% OUTPUT:
%      Q     - Number of occupied interstitials

function Q = fa_VaCount(A, b, indx,p1)
%
if nargin<2
    Q = [];
    disp('not enough input parameters!');
    return;
end


n = numel(b);
if nargin<3;      indx = [];     end
if isempty(indx)
    indx = 1:n;
else
```

```
    n = numel(indx);
end


if nargin<4;      p1 = [];      end
if isempty(p1);   p1 = 2;       end



    Cnt = 0;
    for kk = 1:n
        k = indx(kk);
        aa=A(k,1);
        bb = b(k);
        if bb.pOcup==p1 && aa.pIndx==1
            Cnt = Cnt+1;

        end
    end

    Q = Cnt;

return;
end
```

APPENDIX B

LIST OF ABBREVIATIONS

WBGS	Wide bandgap semiconductor
UID	Unintentionally doped
DFT	Density functional theory
TBC	Thermal boundary conductance
TBR	Thermal boundary resistance
EFG	Edge-defined film-fed growth
RMS	Root mean squared
PLD	Pulsed laser deposition
MOCVD	Metal organic chemical vapour deposition
ALD	Atomic layer deposition
AFM	Atomic force microscope
SEM	Scanning electron microscope
EDX	Energy dispersive x-ray spectroscopy
PBS	Polarising beam splitter
FEM	Finite element method
VBM	Valence band maximum
TEM	Transmission electron microscope
XPS	X-ray photoelectron spectroscopy
TTR	Transient thermoreflectance
DSF	Damped shifted force
CS	Core/shell
UFF	Universal force field
MEAM	Modified embedded atom method

MOSFET	Metal-oxide-semiconductor field-effect transistor
BFOM	Baliga figure of merit
HRTEM	High resolution transmission electron microscopy
XRD	X-ray diffraction
GIXRD	Grazing incidence x-ray diffraction
EBSD	Electron back-scatter diffraction
TDTR	Time-domain thermoreflectance
RBS	Rutherford backscattering
IVEM	Intermediate Voltage Electron Microscope
NRT	Norgett-Robinson-Torrens
HOLZ	Higher order Laue zone
ZOLZ	Zero order Laue zone
FOLZ	First order Laue zone
CBED	Convergent beam electron diffraction
FIB	Focused ion beam
CAB	Core and bond
CA	Cellular automaton
SRIM	Stopping range of ions in matter
LAMMPS	Large-scale atomic/molecular massively parallel simulator
VESTA	Visualisation for electronic and structural analysis

BIBLIOGRAPHY

[1] C. Janowitz, V. Scherer, M. Mohamed, A. Krapf, H. Dwelk, R. Manzke, Z. Galazka, R. Uecker, K. Irmscher, R. Fornari, M. Michling, D. Schmeißer, J. R. Weber, J. B. Varley, and C. G. Van De Walle, “Experimental electronic structure of In_2O_3 and Ga_2O_3,” *New Journal of Physics*, vol. 13, p. 085014, 2011.

[2] G. Jessen, K. Chabak, A. Green, J. McCandless, S. Tetlak, K. Leedy, R. Fitch, S. Mou, E. Heller, S. Badescu, A. Crespo, and N. Moser, “Toward realization of Ga2O3 for power electronics applications,” *Device Research Conference - Conference Digest*, vol. 75, no. 62, p. 1, 2017.

[3] J. Y. Tsao, S. Chowdhury, M. A. Hollis, D. Jena, N. M. Johnson, K. A. Jones, R. J. Kaplar, S. Rajan, C. G. Van de Walle, E. Bellotti, C. L. Chua, R. Collazo, M. E. Coltrin, J. A. Cooper, K. R. Evans, S. Graham, T. A. Grotjohn, E. R. Heller, M. Higashiwaki, M. S. Islam, P. W. Juodawlkis, M. A. Khan, A. D. Koehler, J. H. Leach, U. K. Mishra, R. J. Nemanich, R. C. Pilawa-Podgurski, J. B. Shealy, Z. Sitar, M. J. Tadjer, A. F. Witulski, M. Wraback, and J. A. Simmons, “Ultrawide-Bandgap Semiconductors: Research Opportunities and Challenges,” *Advanced Electronic Materials*, vol. 4, no. 1, p. 1600501, 2018.

[4] S. J. Pearton, F. Ren, M. Tadjer, and J. Kim, “Perspective: Ga_2O_3 for ultra-high power rectifiers and MOSFETS,” *Journal of Applied Physics*, vol. 124, no. 22, p. 220901, 2018.

[5] K. D. Chabak, K. D. Leedy, A. J. Green, S. Mou, A. T. Neal, T. Asel, E. R. Heller, N. S. Hendricks, K. Liddy, A. Crespo, N. C. Miller, M. T. Lindquist, N. A. Moser, R. C. F. Jr, and D. E. W. Jr, “Lateral β-Ga_2O_3 field effect transistors,” *Semiconductor Science and Technology*, vol. 35, no. 1, p. 013002, 2020.

[6] Y. Wei, X. Li, J. Yang, C. Liu, J. Zhao, Y. Liu, and S. Dong, “Interaction between hydrogen and gallium vacancies in β-Ga_2O_3,” *Scientific Reports*, vol. 8, no. 1, pp. 1–8, 2018.

[7] Z. Chi, J. J. Asher, M. R. Jennings, and E. Chikoidze, “Ga $_2O_3$ and Related Ultra-Wide Bandgap Power Semiconductor Mitigation,” *Materials*, vol. 15, p. 1164, 2022.

[8] S. J. Pearton, J. Yang, P. H. Cary, F. Ren, J. Kim, M. J. Tadjer, and M. A. Mastro, "A review of Ga_2O_3 materials, processing, and devices," *Applied Physics Reviews*, vol. 5, no. 1, 2018.

[9] S. B. Reese, T. Remo, J. Green, and A. Zakutayev, "How much will gallium oxide power electronics cost?," *Joule*, vol. 3, no. 4, pp. 903–907, 2019.

[10] J. Kim, S. J. Pearton, C. Fares, J. Yang, F. Ren, S. Kim, and A. Y. Polyakov, "Radiation damage effects in Ga_2O_3 materials and devices," *Journal of Materials Chemistry C*, vol. 7, no. 1, p. 10, 2019.

[11] E. G. Stassinopoulos, G. J. Brucker, D. W. Nakamura, C. A. Stauffer, G. B. Gee, and J. L. Barth, "Solar flare proton evaluation at geostationary orbits for engineering applications," *IEEE Transactions on Nuclear Science*, vol. 43, no. 2 PART 1, p. 369, 1996.

[12] J. Zhao, X. Huang, Y. Yin, Y. Liao, H. Mo, Q. Qian, Y. Guo, X. Chen, Z. Zhang, and M. Hua, "Two-Dimensional Gallium Oxide Monolayer for Gas-Sensing Application," *Journal of Physical Chemistry Letters*, vol. 12, p. 5813, 2021.

[13] K. Vimalanathan, T. Palmer, Z. Gardner, I. Ling, S. Rahpeima, S. Elmas, J. R. Gascooke, C. T. Gibson, Q. Sun, J. Zou, M. R. Andersson, N. Darwish, and C. L. Raston, "High shear: In situ exfoliation of 2D gallium oxide sheets from centrifugally derived thin films of liquid gallium," *Nanoscale Advances*, vol. 3, no. 20, p. 5785, 2021.

[14] L. Dejace, N. Laubeuf, I. Furfaro, and S. P. Lacour, "Gallium-Based Thin Films for Wearable Human Motion Sensors," *Advanced Intelligent Systems*, vol. 1, no. 5, p. 1900079, 2019.

[15] S. I. Stepanov, V. I. Nikolaev, V. E. Bougrov, and A. E. Romanov, "Gallium oxide: Properties and applications - A review," *Reviews on Advanced Materials Science*, vol. 44, no. 1, p. 63, 2016.

[16] Z. Guo, A. Verma, X. Wu, F. Sun, A. Hickman, T. Masui, A. Kuramata, M. Higashiwaki, D. Jena, and T. Luo, "Anisotropic thermal conductivity in single crystal β-gallium oxide," *Applied Physics Letters*, vol. 106, no. 11, p. 1, 2015.

[17] M. Kuball and J. W. Pomeroy, "A review of raman thermography for electronic and opto-electronic device measurement with submicron spatial and nanosecond temporal resolution," *IEEE Transactions on Device and Materials Reliability*, vol. 16, no. 4, p. 667, 2016.

[18] C. Yuan, Y. Zhang, R. Montgomery, S. Kim, J. Shi, A. Mauze, T. Itoh, J. S. Speck, and S. Graham, "Modeling and analysis for thermal management in gallium oxide field-effect transistors," *Journal of Applied Physics*, vol. 127, no. 15, p. 154502, 2020.

[19] N. Ma, N. Tanen, A. Verma, Z. Guo, T. Luo, H. G. Xing, and D. Jena, "Intrinsic electron mobility limits in β-Ga2O3," *Applied Physics Letters*, vol. 109, no. 21, p. 1, 2016.

[20] M. I. Pintor-Monroy, D. Barrera, B. L. Murillo-Borjas, F. J. Ochoa-Estrella, J. W. Hsu, and M. A. Quevedo-Lopez, "Tunable Electrical and Optical Properties of Nickel Oxide (NiO_x) Thin Films for Fully Transparent NiO_x-Ga_2O_3 p-n Junction Diodes," *ACS Applied Materials and Interfaces*, vol. 10, no. 44, p. 38159, 2018.

[21] P. Li, H. Shi, K. Chen, D. Guo, W. Cui, Y. Zhi, S. Wang, Z. Wu, Z. Chen, and W. Tang, "Construction of GaN/Ga_2O_3 p-n junction for an extremely high responsivity self-powered UV photodetector," *Journal of Materials Chemistry C*, vol. 5, no. 40, p. 10562, 2017.

[22] A. Mishra, Z. Abdallah, J. W. Pomeroy, M. J. Uren, and M. Kuball, "Electrical and Thermal Performance of Ga_2O_3–Al_2O_3–Diamond Super-Junction Schottky Barrier Diodes," *IEEE Transactions on Electron Devices*, vol. 68, no. 10, p. 5055, 2021.

[23] H. Peelaers and C. G. Van De Walle, "Sub-band-gap absorption in Ga_2O_3," *Applied Physics Letters*, vol. 111, no. 18, p. 182104, 2017.

[24] S. Mu, H. Peelaers, Y. Zhang, M. Wang, and C. G. Van De Walle, "Orientation-dependent band offsets between $(Al_xGa_{1-x})_2O_3$ and Ga_2O_3," *Applied Physics Letters*, vol. 117, no. 25, p. 252104, 2020.

[25] W. Li, K. Nomoto, Z. Hu, D. Jena, and H. G. Xing, "Fin-channel orientation dependence of forward conduction in kV-class Ga_2O_3 trench Schottky barrier diodes," *Applied Physics Express*, vol. 12, no. 6, p. 8, 2019.

[26] "Crystal Structure of β-Ga_2O_3," *Journal of Chemical Physics*, vol. 33, 1960.

[27] I. Cora, F. Mezzadri, F. Boschi, M. Bosi, M. Čaplovičová, G. Calestani, I. Dódony, B. Pécz, and R. Fornari, "The real structure of ϵ-Ga_2O_3 and its relation to κ-phase," *CrystEngComm*, vol. 19, no. 11, pp. 1509–1516, 2017.

[28] S. Yoshioka, H. Hayashi, A. Kuwabara, F. Oba, K. Matsunaga, and I. Tanaka, "Structures and energetics of Ga_2O_3 polymorphs," *Journal of Physics Condensed Matter*, vol. 19, no. 34, p. 346211, 2007.

[29] H. Y. Playford, A. C. Hannon, E. R. Barney, and R. I. Walton, "Structures of uncharacterised polymorphs of gallium oxide from total neutron diffraction," *Chemistry - A European Journal*, vol. 19, no. 8, p. 2803, 2013.

[30] J. E. Swallow, C. Vorwerk, P. Mazzolini, P. Vogt, O. Bierwagen, A. Karg, M. Eickhoff, J. Schörmann, M. R. Wagner, J. W. Roberts, P. R. Chalker, M. J. Smiles, P. Murgatroyd, S. A. Razek, Z. W. Lebens-Higgins, L. F. Piper, L. A. Jones, P. K. Thakur, T. L. Lee, J. B.

Varley, J. Furthmüller, C. Draxl, T. D. Veal, and A. Regoutz, "Influence of Polymorphism on the Electronic Structure of Ga_2O_3," *Chemistry of Materials*, vol. 32, no. 19, p. 8460, 2020.

[31] J. L. Lyons, " Electronic Properties of Ga_2O_3 Polymorphs ," *ECS Journal of Solid State Science and Technology*, vol. 8, no. 7, p. Q3226, 2019.

[32] X. Wang, M. Faizan, G. Na, X. He, Y. H. Fu, and L. Zhang, "Discovery of New Polymorphs of Gallium Oxides with Particle Swarm Optimization-Based Structure Searches," *Advanced Electronic Materials*, vol. 6, no. 6, p. 1, 2020.

[33] H. Sun, K. H. Li, C. G. Castanedo, S. Okur, G. S. Tompa, T. Salagaj, S. Lopatin, A. Genovese, and X. Li, "HCl Flow-Induced Phase Change of α-, β-, and ϵ-Ga_2O_3 Films Grown by MOCVD," *Crystal Growth and Design*, vol. 18, no. 4, p. 2370, 2018.

[34] H. Peelaers, J. B. Varley, J. S. Speck, and C. G. Van De Walle, "Structural and electronic properties of Ga_2O_3-Al_2O_3 alloys," *Applied Physics Letters*, vol. 112, no. 24, p. 242101, 2018.

[35] G. Yang, P. R. Romeo, A. Apostoluk, and B. Vilquin, " First principles study on the lattice thermal conductivity of α-phase Ga2O_3 ," *Journal of Vacuum Science Technology A*, vol. 40, no. 5, p. 052801, 2022.

[36] J. Kim, D. Tahara, Y. Miura, and B. G. Kim, "First-principle calculations of electronic structures and polar properties of (κ,ϵ)-Ga_2O_3," *Applied Physics Express*, vol. 11, no. 6, p. 1, 2018.

[37] S. Seacat, J. L. Lyons, and H. Peelaers, "Properties of orthorhombic Ga_2O_3 alloyed with In_2O_3 and Al_2O_3," *Applied Physics Letters*, vol. 119, no. 4, p. 042104, 2021.

[38] F. Mezzadri, G. Calestani, F. Boschi, D. Delmonte, M. Bosi, and R. Fornari, "Crystal structure and ferroelectric properties of ϵ-Ga_2O_3 films grown on (0001)-sapphire," *Inorganic Chemistry*, vol. 55, no. 22, p. 12079, 2016.

[39] J. M. Johnson, H. L. Huang, M. Wang, S. Mu, J. B. Varley, A. F. Uddin Bhuiyan, Z. Feng, N. K. Kalarickal, S. Rajan, H. Zhao, C. G. Van de Walle, and J. Hwang, "Atomic scale investigation of aluminum incorporation, defects, and phase stability in β-$(Al_xGa_{1-x})_2O_3$ films," *APL Materials*, vol. 9, no. 5, p. 051103, 2021.

[40] H. L. Huang, C. Chae, and J. Hwang, "Perspective on atomic scale investigation of point and extended defects in gallium oxide," *Journal of Applied Physics*, vol. 131, no. 19, p. 190901, 2022.

[41] K. R. Gann, C. S. Chang, M. C. Chang, D. R. Sutherland, A. B. Connolly, D. A. Muller, R. B. Van Dover, and M. O. Thompson, "Initial nucleation of metastable γ-Ga_2O_3 during sub-millisecond thermal anneals of amorphous Ga_2O_3," *Applied Physics Letters*, vol. 121, no. 6, 2022.

[42] L. N. Cojocaru, "Defect-annealing in neutron-damaged β-Ga_2O_3," *Radiation Effects*, vol. 21, no. 3, p. 157, 1974.

[43] J. Lee, E. Flitsiyan, L. Chernyak, J. Yang, F. Ren, S. J. Pearton, B. Meyler, and Y. J. Salzman, "Effect of 1.5 MeV electron irradiation on β-Ga_2O_3 carrier lifetime and diffusion length," *Applied Physics Letters*, vol. 112, no. 8, 2018.

[44] J. Yang, Z. Chen, F. Ren, S. J. Pearton, G. Yang, J. Kim, J. Lee, E. Flitsiyan, L. Chernyak, and A. Kuramata, "10 MeV proton damage in β-Ga_2O_3 Schottky rectifiers," *Journal of Vacuum Science & Technology B, Nanotechnology and Microelectronics: Materials, Processing, Measurement, and Phenomena*, vol. 36, no. 1, p. 011206, 2018.

[45] M. H. Wong, A. Takeyama, T. Makino, T. Ohshima, K. Sasaki, A. Kuramata, S. Yamakoshi, and M. Higashiwaki, "Radiation hardness of β-Ga_2O_3 metal-oxide-semiconductor field-effect transistors against gamma-ray irradiation," *Applied Physics Letters*, vol. 112, no. 2, p. 023503, 2018.

[46] S. Kumar, T. Kamimura, C. H. Lin, Y. Nakata, and M. Higashiwaki, "Reduction in leakage current through interface between Ga_2O_3 epitaxial layer and substrate by ion implantation doping of compensating impurities," *Applied Physics Letters*, vol. 117, no. 19, pp. 3–8, 2020.

[47] H. Peelaers, J. L. Lyons, J. B. Varley, and C. G. Van De Walle, "Deep acceptors and their diffusion in Ga_2O_3," *APL Materials*, vol. 7, no. 2, p. 022519, 2019.

[48] E. Wendler, E. Treiber, J. Baldauf, S. Wolf, and C. Ronning, "High-level damage saturation below amorphisation in ion implanted β-Ga_2O_3," *Nuclear Instruments and Methods in Physics Research, Section B: Beam Interactions with Materials and Atoms*, vol. 379, p. 85, 2016.

[49] E. A. Anber, D. Foley, A. C. Lang, J. Nathaniel, J. L. Hart, M. J. Tadjer, K. D. Hobart, S. Pearton, and M. L. Taheri, "Structural transition and recovery of Ge implanted β -Ga2O3," *Applied Physics Letters*, vol. 117, no. 15, p. 1, 2020.

[50] A. Azarov, C. Bazioti, V. Venkatachalapathy, P. Vajeeston, E. Monakhov, and A. Kuznetsov, "Disorder-Induced Ordering in Gallium Oxide Polymorphs," *Physical Review Letters*, vol. 128, no. 1, p. 1, 2022.

[51] S. B. Kjeldby, A. Azarov, P. D. Nguyen, V. Venkatachalapathy, R. Mikšová, A. MacKová, A. Kuznetsov, O. Prytz, and L. Vines, “Radiation-induced defect accumulation and annealing in Si-implanted gallium oxide,” *Journal of Applied Physics*, vol. 131, no. 12, p. 125701, 2022.

[52] A. Titov, K. Karabeshkin, A. Struchkov, V. Nikolaev, A. Azarov, D. Gogova, and P. Karaseov, “Comparative study of radiation tolerance of GaN and Ga_2O_3 polymorphs,” *Vacuum*, vol. 200, no. October 2021, p. 111005, 2022.

[53] Z. Galazka, R. Uecker, K. Irmscher, M. Albrecht, D. Klimm, M. Pietsch, M. Brützam, R. Bertram, S. Ganschow, and R. Fornari, “Czochralski growth and characterization of β-Ga_2O_3 single crystals,” *Crystal Research and Technology*, vol. 45, no. 12, p. 1229, 2010.

[54] Y. Tomm, P. Reiche, D. Klimm, and T. Fukuda, “Czochralski grown Ga_2O_3 crystals,” *Journal of Crystal Growth*, vol. 220, no. 4, p. 510, 2000.

[55] J. D. Blevins, K. Chabak, G. Jessen, D. Thomson, K. Stevens, G. Foundos, A. Lindsey, J. H. Leach, J. Rumsey, and A. Green, “Growth of 50mm beta-gallium oxide (β-Ga_2O_3) substrates,” *CS MANTECH 2018 - 2018 International Conference on Compound Semiconductor Manufacturing Technology*, vol. 1, no. 010, p. 4, 2018.

[56] X. Tang, B. Liu, Y. Yu, S. Liu, and B. Gao, “Numerical analysis of difficulties of growing large-size bulk β-Ga_2O_3 single crystals with the Czochralski method,” *Crystals*, vol. 11, no. 1, p. 1, 2021.

[57] K. N. Heinselman, D. Haven, A. Zakutayev, and S. B. Reese, “Projected Cost of Gallium Oxide Wafers from Edge-Defined Film-Fed Crystal Growth,” *Crystal Growth and Design*, vol. 22, no. 8, p. 4854, 2022.

[58] Y. Yao, Y. Ishikawa, and Y. Sugawara, “Slip planes in monoclinic β-Ga_2O_3revealed from its 010 face via synchrotron X-ray diffraction and X-ray topography,” *Japanese Journal of Applied Physics*, vol. 59, no. 12, p. 125501, 2020.

[59] O. Ueda, M. Kasu, and H. Yamaguchi, “Structural characterization of defects in EFG- and HVPE-grown β-Ga_2O_3crystals,” *Japanese Journal of Applied Physics*, vol. 61, no. 5, 2022.

[60] A. Usseinov, Z. Koishybayeva, A. Platonenko, V. Pankratov, Y. Suchikova, A. Akilbekov, M. Zdorovets, J. Purans, and A. I. Popov, “Vacancy defects in Ga_2O_3: First-principles calculations of electronic structure,” *Materials*, vol. 14, no. 23, 2021.

[61] Z. Galazka, K. Irmscher, R. Schewski, I. M. Hanke, M. Pietsch, S. Ganschow, D. Klimm, A. Dittmar, A. Fiedler, T. Schroeder, and M. Bickermann, "Czochralski-grown bulk β-Ga_2O_3 single crystals doped with mono-, di-, tri-, and tetravalent ions," *Journal of Crystal Growth*, vol. 529, no. September 2019, p. 125297, 2020.

[62] M. M. Islam, M. O. Liedke, D. Winarski, M. Butterling, A. Wagner, P. Hosemann, Y. Wang, B. Uberuaga, and F. A. Selim, "Chemical manipulation of hydrogen induced high p-type and n-type conductivity in Ga_2O_3," *Scientific Reports*, vol. 10, no. 1, p. 1, 2020.

[63] J. B. Varley, J. R. Weber, A. Janotti, and C. G. Van De Walle, "Oxygen vacancies and donor impurities in β-Ga_2O_3," *Applied Physics Letters*, vol. 97, no. 14, p. 97, 2010.

[64] J. Bae, H. W. Kim, I. H. Kang, G. Yang, and J. Kim, "High breakdown voltage quasi-two-dimensional β-Ga_2O_3 field-effect transistors with a boron nitride field plate," *Applied Physics Letters*, vol. 112, no. 12, 2018.

[65] Z. Cheng, L. Yates, J. Shi, M. J. Tadjer, K. D. Hobart, and S. Graham, "Thermal conductance across β-Ga_2O_3-diamond van der Waals heterogeneous interfaces," *APL Materials*, vol. 7, p. 031118, 2019.

[66] Y. Kwon, G. Lee, S. Oh, J. Kim, S. J. Pearton, and F. Ren, "Tuning the thickness of exfoliated quasi-two-dimensional β-Ga_2O_3 flakes by plasma etching," *Applied Physics Letters*, vol. 110, no. 13, 2017.

[67] T. Matsumae, Y. Kurashima, H. Umezawa, K. Tanaka, T. Ito, H. Watanabe, and H. Takagi, "Low-temperature direct bonding of β-Ga_2O_3 and diamond substrates under atmospheric conditions," *Applied Physics Letters*, vol. 116, no. 14, pp. 2–6, 2020.

[68] T. Matsumae, Y. Kurashima, H. Umezawa, and H. Takagi, "Hydrophilic direct bonding of diamond (111) substrate using treatment with H2SO4/H2O2," *Japanese Journal of Applied Physics*, vol. 59, no. SB, 2020.

[69] P. Sittimart, S. Ohmagari, T. Matsumae, H. Umezawa, and T. Yoshitake, "Diamond/β-Ga_2O_3 p-n heterojunction diodes fabricated by low-temperature direct-bonding," *AIP Advances*, vol. 11, no. 10, pp. 1–7, 2021.

[70] W. Xu, X. Wang, Y. Wang, T. You, X. Ou, G. Han, H. Hu, S. Zhang, F. Mu, T. Suga, Y. Zhang, and Y. Hao, "First Demonstration of Waferscale Heterogeneous Integration of Ga_2O_3 MOSFETs on SiC and Si Substrates by Ion-Cutting Process," *Technical Digest - International Electron Devices Meeting, IEDM*, vol. 2019-December, p. 274, 2019.

[71] W. Xu, T. You, F. Mu, Z. Shen, J. Lin, K. Huang, M. Zhou, A. Yi, Z. Qu, T. Suga, G. Han, and X. Ou, "Thermodynamics of Ion-Cutting of β-Ga_2O_3 and Wafer-Scale Heterogeneous

Integration of a β-Ga_2O_3 Thin Film onto a Highly Thermal Conductive SiC Substrate," *ACS Applied Electronic Materials*, vol. 4, no. 1, p. 494, 2022.

[72] B. R. Tak, S. Kumar, A. K. Kapoor, D. Wang, X. Li, H. Sun, and R. Singh, "Recent advances in the growth of gallium oxide thin films employing various growth techniques - A review," *Journal of Physics D: Applied Physics*, vol. 54, no. 45, 2021.

[73] M. K. Yadav, A. Mondal, S. Das, S. K. Sharma, and A. Bag, "Impact of annealing temperature on band-alignment of PLD grown Ga_2O_3/Si (100) heterointerface," *Journal of Alloys and Compounds*, vol. 819, p. 153052, 2020.

[74] J. Lee, H. Kim, L. Gautam, and M. Razeghi, "High thermal stability of κ-Ga_2O_3 grown by MOCVD," *Crystals*, vol. 11, no. 4, 2021.

[75] Z. Cheng, V. D. Wheeler, T. Bai, J. Shi, M. J. Tadjer, T. Feygelson, K. D. Hobart, M. S. Goorsky, and S. Graham, "Integration of polycrystalline Ga_2O_3 on diamond for thermal management," *Applied Physics Letters*, vol. 116, no. 6, 2020.

[76] O. A. Williams, O. Douhéret, M. Daenen, K. Haenen, E. Osawa, and M. Takahashi, "Enhanced diamond nucleation on monodispersed nanocrystalline diamond," *Chemical Physics Letters*, vol. 445, no. 4-6, pp. 255–258, 2007.

[77] S. Mandal, K. Arts, H. C. Knoops, J. A. Cuenca, G. M. Klemencic, and O. A. Williams, "Surface zeta potential and diamond growth on gallium oxide single crystal," *Carbon*, vol. 181, p. 79, 2021.

[78] A. Petkov, A. Mishra, M. Cattelan, D. Field, J. Pomeroy, and M. Kuball, "Electrical and thermal characterisation of liquid metal thin-film Ga_2O_3–SiO_2 heterostructures," *Scientific Reports*, vol. 13, no. 1, pp. 1–7, 2023.

[79] J. E. Swallow, J. B. Varley, L. A. Jones, J. T. Gibbon, L. F. Piper, V. R. Dhanak, and T. D. Veal, "Transition from electron accumulation to depletion at β-Ga_2O_3 surfaces: The role of hydrogen and the charge neutrality level," *APL Materials*, vol. 7, no. 2, p. 022528, 2019.

[80] J. Lin, Q. Li, T. Y. Liu, Y. Cui, H. Zheng, and J. Liu, "Printing of Quasi-2D Semiconducting β-Ga_2O_3 in Constructing Electronic Devices via Room-Temperature Liquid Metal Oxide Skin," *Physica Status Solidi - Rapid Research Letters*, vol. 13, no. 9, p. 1, 2019.

[81] H. R. Shanks, P. D. Maycock, P. H. Sidles, and G. C. Danielson, "Thermal conductivity of silicon from 300 to 1400°k," *Physical Review*, vol. 130, p. 1743, 1963.

[82] A. Zavabeti, J. Z. Ou, B. J. Carey, N. Syed, R. Orrell-Trigg, E. L. Mayes, C. Xu, O. Kavehei, A. P. O'Mullane, R. B. Kaner, K. Kalantar-Zadeh, and T. Daeneke, "A liquid metal

reaction environment for the room-temperature synthesis of atomically thin metal oxides," *Science*, vol. 358, no. 6361, p. 332, 2017.

[83] A. Martin, C. Du, B. Chang, and M. Thuo, "Complexity and Opportunities in Liquid Metal Surface Oxides," *Chemistry of Materials*, vol. 32, no. 21, p. 9045, 2020.

[84] R. Lin, W. Zheng, D. Zhang, Y. Li, and F. Huang, "Brushed Crystallized Ultrathin Oxides: Recrystallization and Deep-Ultraviolet Imaging Application," *ACS Applied Electronic Materials*, vol. 1, no. 10, p. 2166, 2019.

[85] M. P. Seah and W. A. Dench, "Quantitative electron spectroscopy of surfaces: A standard data base for electron inelastic mean free paths in solids," *Surface and Interface Analysis*, vol. 1, no. 1, p. 2, 1979.

[86] Z. Chen, K. Nishihagi, X. Wang, K. Saito, T. Tanaka, M. Nishio, M. Arita, and Q. Guo, "Band alignment of Ga_2O_3/Si heterojunction interface measured by X-ray photoelectron spectroscopy," *Applied Physics Letters*, vol. 109, no. 10, p. 1, 2016.

[87] Y. W. Huan, K. Xu, W. J. Liu, H. Zhang, D. A. Golosov, C. T. Xia, H. Y. Yu, X. H. Wu, Q. Q. Sun, and S. J. Ding, "Investigation of Band Alignment for Hybrid 2D-MoS_2/3D-β-Ga_2O_3 Heterojunctions with Nitridation," *Nanoscale Research Letters*, vol. 14, no. 1, p. 360, 2019.

[88] S. Geng, S. Zhang, and H. Onishi, "XPS applications in thin films research," *Materials Technology*, vol. 17, no. 4, p. 234, 2002.

[89] A. Waqas, D. Melati, Z. Mushtaq, B. S. Chowdhry, and A. Melloni, "An Improved Model to Predict the Temperature Dependence of Refractive Index of InP-based Compounds," *Wireless Personal Communications*, vol. 95, no. 2, pp. 607–615, 2017.

[90] C. A. Paddock and G. L. Eesley, "Transient thermoreflectance from thin metal films," *Journal of Applied Physics*, vol. 60, no. 1, p. 285, 1986.

[91] P. Hui and H. S. Tan, "A transmission-line theory for heat conduction in multilayer thin films," *IEEE TRANSACTIONS ON COMPONENTS, PACKAGING, AND MANUFACTURING TECHNOLOGY, B*, vol. 17, no. 3, p. 426, 1994.

[92] C. Yuan, W. M. Waller, and M. Kuball, "Nanosecond transient thermoreflectance method for characterizing anisotropic thermal conductivity," *Review of Scientific Instruments*, vol. 90, no. 11, p. 114903, 2019.

[93] J. F. Moulder, W. F. Stickle, W. M. Sobol, and K. D. Bomben, *Handbook of X-ray Photoelectron Spectroscopy*.
Physical Electronics Division, 1992.

[94] D. Zatsepin, D. Boukhvalov, A. Zatsepin, Y. A. Kuznetsova, D. Gogova, V. Shur, and A. Esin, "Atomic structure, electronic states, and optical properties of epitaxially grown β-Ga_2O_3 layers," *Superlattices and Microstructures*, vol. 120, p. 90, 2018.

[95] D. A. Tashmukhamedova and M. B. Yusupjanova, "Emission and optical properties of SiO_2/Si thin films," *Journal of Surface Investigation. X-ray, Synchrotron and Neutron Techniques*, vol. 10, p. 1273, 2016.

[96] J. W. Keister, J. E. Rowe, J. J. Kolodziej, H. Niimi, T. E. Madey, and G. Lucovsky, "Band offsets for ultrathin SiO_2 and Si_3N_4 films on Si(111) and Si(100) from photoemission spectroscopy," *Journal of Vacuum Science & Technology B: Microelectronics and Nanometer Structures*, vol. 17, no. 4, p. 1831, 1999.

[97] T. E. Cook, C. C. Fulton, W. J. Mecouch, K. M. Tracy, R. F. Davis, E. H. Hurt, G. Lucovsky, and R. J. Nemanich, "Measurement of the band offsets of SiO_2 on clean n- and p-type GaN(0001)," *Journal of Applied Physics*, vol. 93, no. 7, p. 3995, 2003.

[98] Z. Zhang, Y. Guo, and J. Robertson, "Atomic structure and band alignment at Al_2O_3/GaN, Sc_2O_3/GaN and La_2O_3/GaN interfaces: A first-principles study," *Microelectronic Engineering*, vol. 216, no. April, p. 111039, 2019.

[99] K. Shi, X. L. Liu, D. B. Li, J. Wang, H. P. Song, X. Q. Xu, H. Y. Wei, C. M. Jiao, S. Y. Yang, H. Song, Q. S. Zhu, and Z. G. Wang, "Valence band offset of GaN/diamond heterojunction measured by X-ray photoelectron spectroscopy," *Applied Surface Science*, vol. 257, no. 18, p. 8110, 2011.

[100] D. E. Field, J. W. Pomeroy, F. Gity, M. Schmidt, P. Torchia, F. Li, P. M. Gammon, V. A. Shah, and M. Kuball, "Thermal characterization of direct wafer bonded Si-on-SiC," *Applied Physics Letters*, vol. 120, no. 11, p. 113503, 2022.

[101] W. Zhu, G. Zheng, S. Cao, and H. He, "Thermal conductivity of amorphous SiO_2 thin film: A molecular dynamics study," *Scientific Reports*, vol. 8, no. 1, p. 1, 2018.

[102] Y. Lee and G. S. Hwang, "Mechanism of thermal conductivity suppression in doped silicon studied with nonequilibrium molecular dynamics," *Phys. Rev. B*, vol. 86, p. 075202, Aug 2012.

[103] P. Jiang, X. Qian, and R. Yang, "Tutorial: Time-domain thermoreflectance (TDTR) for thermal property characterization of bulk and thin film materials," *Journal of Applied Physics*, vol. 124, no. 16, pp. 1–82, 2018.

[104] Y. Song, P. Ranga, Y. Zhang, Z. Feng, H. L. Huang, M. D. Santia, S. C. Badescu, C. U. Gonzalez-Valle, C. Perez, K. Ferri, R. M. Lavelle, D. W. Snyder, B. A. Klein, J. Deitz, A. G.

Baca, J. P. Maria, B. Ramos-Alvarado, J. Hwang, H. Zhao, X. Wang, S. Krishnamoorthy, B. M. Foley, and S. Choi, “Thermal Conductivity of β-Phase $Ga_2O_3$and $(Al_xGa_{1-x})_2O_3$ Heteroepitaxial Thin Films,” *ACS Applied Materials and Interfaces*, vol. 13, no. 32, pp. 38477–38490, 2021.

[105] C. J. Szwejkowski, N. C. Creange, K. Sun, A. Giri, B. F. Donovan, C. Constantin, and P. E. Hopkins, “Size effects in the thermal conductivity of gallium oxide (β-Ga_2O_3) films grown via open-atmosphere annealing of gallium nitride,” *Journal of Applied Physics*, vol. 117, no. 8, 2015.

[106] W. Haynes, *CRC Handbook of Chemistry and Physics, 95th Edition*. CRC Press, Taylor & Francis Group, 2015.

[107] A. Petkov, A. Mishra, J. W. Pomeroy, and M. Kuball, “Molecular dynamics study of thermal transport across Ga_2O_3-diamond interfaces,” *Applied Physics Letters*, vol. 122, no. 3, 2023.

[108] S. I. Stepanov, V. I. Nikolaev, V. E. Bougrov, and A. E. Romanov, “Gallium oxide: Properties and applications - A review,” *Reviews on Advanced Materials Science*, vol. 44, no. 1, p. 63, 2016.

[109] H. Kim, S. Tarelkin, A. Polyakov, S. Troschiev, S. Nosukhin, M. Kuznetsov, and J. Kim, “ Ultrawide-Bandgap p-n Heterojunction of Diamond/ β-Ga_2O_3 for a Solar-Blind Photodiode ,” *ECS Journal of Solid State Science and Technology*, vol. 9, p. 045004, 2020.

[110] A. P. Thompson, H. M. Aktulga, R. Berger, D. S. Bolintineanu, W. M. Brown, P. S. Crozier, P. J. in ’t Veld, A. Kohlmeyer, S. G. Moore, T. D. Nguyen, R. Shan, M. J. Stevens, J. Tranchida, C. Trott, and S. J. Plimpton, “LAMMPS - a flexible simulation tool for particle-based materials modeling at the atomic, meso, and continuum scales,” *Comp. Phys. Comm.*, vol. 271, p. 108171, 2022.

[111] J. Chen, X. Xu, J. Zhou, and B. Li, “Interfacial thermal resistance: Past, present, and future,” *Rev. Mod. Phys.*, vol. 94, p. 025002, Apr 2022.

[112] X. Peng, P. Jiang, Y. Ouyang, S. Lu, W. Ren, and J. Chen, “Reducing Kapitza resistance between graphene/water interface via interfacial superlattice structure,” *Nanotechnology*, vol. 33, no. 3, 2022.

[113] M. A. Blanco, M. B. Sahariah, H. Jiang, A. Costales, and R. Pandey, “Energetics and migration of point defects in Ga_2O_3,” *Physical Review B - Condensed Matter and Materials Physics*, vol. 72, no. 18, p. 1, 2005.

[114] S. Blonski and S. H. Garofalini, “Molecular dynamics simulations of α-alumina and γ-alumina surfaces,” *Surface Science*, vol. 295, p. 263, 1993.

[115] G. Wang, Y. Cui, X. Li, S. Yang, J. Zhao, H. Tang, and X. Li, “Molecular dynamics simulation on microstructure and physicochemical properties of FexO-SiO_2-CaO-MgO-“NiO” slag in nickel matte smelting under modulating CaO content,” *Minerals*, vol. 10, no. 2, pp. 1–15, 2020.

[116] M. Tosi and F. Fumi, “Ionic sizes and born repulsive parameters in the nacl-type alkali halides—ii: The generalized huggins-mayer form,” *Journal of Physics and Chemistry of Solids*, vol. 25, no. 1, p. 45, 1964.

[117] Y.-j. Hu, G. Zhao, M. Zhang, B. Bin, T. D. Rose, Q. Zhao, Q. Zu, Y. Chen, and X. Sun, “Predicting densities and elastic moduli of SiO_2 -based glasses by machine learning,” *npj Computational Materials*, vol. 6, no. 25, p. 1, 2020.

[118] L. M. Morgan, M. Molinari, A. Corrias, and D. C. Sayle, “Protecting Ceria Nanocatalysts - The Role of Sacrificial Barriers,” *ACS Applied Materials and Interfaces*, vol. 10, no. 38, p. 32510, 2018.

[119] P. J. Mitchell and D. Fincham, “Shell model simulations by adiabatic dynamics,” *Journal of Physics: Condensed Matter*, vol. 5, p. 1031, feb 1993.

[120] C. J. Fennell and J. D. Gezelter, “Is the ewald summation still necessary? pairwise alternatives to the accepted standard for long-range electrostatics,” *J. Chem. Phys.*, vol. 124, p. 234104, 2006.

[121] H. Aller, X. Yu, A. J. Gellman, J. A. Malen, and A. J. McGaughey, “Thermal Conductance of β-Ga_2O_3/Metal Interfaces,” *InterSociety Conference on Thermal and Thermomechanical Phenomena in Electronic Systems, ITherm 2018*, vol. 17, p. 567, 2018.

[122] A. K. Rappé, C. J. Casewit, K. S. Colwell, W. A. Goddard, and W. M. Skiff, “UFF, a Full Periodic Table Force Field for Molecular Mechanics and Molecular Dynamics Simulations,” *Journal of the American Chemical Society*, vol. 114, no. 25, p. 10024, 1992.

[123] S. Dong, B. Yang, Q. Xin, X. Lan, X. Wang, and G. Xin, “Interfacial thermal transport of graphene/ β-Ga_2O_3 heterojunctions: a molecular dynamics study with a self-consistent interatomic potential,” *Phys. Chem. Chem. Phys.*, vol. 24, p. 12837, 2022.

[124] M. I. Baskes, “Modified embedded-atom potentials for cubic materials and impurities,” *Phys. Rev. B*, vol. 46, p. 2727, 1992.

[125] K. M. Schmidt, A. B. Buettner, O. A. Graeve, and V. R. Vasquez, “Interatomic pair potentials from DFT and molecular dynamics for Ca, Ba, and Sr hexaborides,” *Journal of Materials Chemistry C*, vol. 6, p. 8649, 2015.

[126] K. Momma and F. Izumi, “VESTA 3 for three-dimensional visualization of crystal, volumetric and morphology data,” *Journal of Applied Crystallography*, vol. 44, no. 6, p. 1272, 2011.

[127] J. Che, T. Çağın, W. Deng, and W. A. Goddard III, “Thermal conductivity of diamond and related materials from molecular dynamics simulations,” *J. Chem. Phys.*, vol. 113, p. 6888, 2000.

[128] Q. Tang, “A molecular dynamics simulation: The effect of finite size on the thermal conductivity in a single crystal silicon,” *Molecular Physics*, vol. 102, p. 1959, 2004.

[129] Z. Guo, A. Verma, X. Wu, F. Sun, A. Hickman, T. Masui, A. Kuramata, M. Higashiwaki, D. Jena, and T. Luo, “Anisotropic thermal conductivity in single crystal β-gallium oxide,” *Applied Physics Letters*, vol. 106, p. 1, 2015.

[130] P. L. Kapitza, “Heat transfer and superfluidity of helium ii,” *Phys. Rev.*, vol. 60, p. 354, 1941.

[131] B. Xu, S. Hu, S. W. Hung, C. Shao, H. Chandra, F. R. Chen, T. Kodama, and J. Shiomi, “Weaker bonding can give larger thermal conductance at highly mismatched interfaces,” *Science Advances*, vol. 7, no. 17, p. 1, 2021.

[132] M. D. Santia, N. Tandon, and J. D. Albrecht, “Lattice thermal conductivity in β - Ga 2 O 3 from first principles,” *Applied Physics Letters*, vol. 107, no. 4, p. 041907, 2015.

[133] T. T. Song, M. Yang, J. W. Chai, M. Callsen, J. Zhou, T. Yang, Z. Zhang, J. S. Pan, D. Z. Chi, Y. P. Feng, and S. J. Wang, “The stability of aluminium oxide monolayer and its interface with two-dimensional materials,” *Scientific Reports*, vol. 6, no. June, p. 1, 2016.

[134] A. Ward, D. A. Broido, D. A. Stewart, and G. Deinzer, “Ab initio theory of the lattice thermal conductivity in diamond,” *Phys. Rev. B*, vol. 80, p. 125203, Sep 2009.

[135] C. Monachon and L. Weber, “Influence of a nanometric Al_2O_3 interlayer on the thermal conductance of an Al/(Si, diamond) interface,” *Advanced Engineering Materials*, vol. 17, no. 1, p. 68, 2015.

[136] X. K. Chen, X. Y. Hu, P. Jia, Z. X. Xie, and J. Liu, “Tunable anisotropic thermal transport in porous carbon foams: The role of phonon coupling,” *International Journal of Mechanical Sciences*, vol. 206, no. June, p. 106576, 2021.

[137] N. T. Taylor, C. J. Price, A. Petkov, M. I. Romanis Carr, J. C. Hale, and S. P. Hepplestone, “The Potential of Overlayers on Tin-based Perovskites for Water Splitting,” *Journal of Physical Chemistry Letters*, vol. 11, no. 10, pp. 4124–4130, 2020.

[138] A. Petkov, D. Cherns, W.-Y. Chen, J. Liu, J. Blevins, V. Gambin, M. Li, D. Liu, and M. Kuball, "Structural stability of β-Ga_2O_3 under ion irradiation," *Applied Physics Letters*, vol. 121, p. 171903, Oct 2022.

[139] J. F. Ziegler, M. D. Ziegler, and J. P. Biersack, "SRIM - The stopping and range of ions in matter (2010)," *Nuclear Instruments and Methods in Physics Research, Section B: Beam Interactions with Materials and Atoms*, vol. 268, no. 11-12, p. 1818, 2010.

[140] M. J. Norgett, M. T. Robinson, and I. M. Torrens, "A proposed method of calculating displacement dose rates," *Nuclear Engineering and Design*, vol. 33, no. 1, pp. 50–54, 1975.

[141] M. F. Chaiken and T. E. Blue, "An Estimation of the Neutron Displacement Damage Cross Section for Ga_2O_3," *IEEE Transactions on Nuclear Science*, vol. 65, no. 5, pp. 1147–1152, 2018.

[142] K. Nordlund, S. J. Zinkle, A. E. Sand, F. Granberg, R. S. Averback, R. Stoller, T. Suzudo, L. Malerba, F. Banhart, W. J. Weber, F. Willaime, S. L. Dudarev, and D. Simeone, "Improving atomic displacement and replacement calculations with physically realistic damage models," *Nature Communications*, vol. 9, no. 1, 2018.

[143] R. E. Stoller, M. B. Toloczko, G. S. Was, A. G. Certain, S. Dwaraknath, and F. A. Garner, "On the use of SRIM for computing radiation damage exposure," *Nuclear Instruments and Methods in Physics Research, Section B: Beam Interactions with Materials and Atoms*, vol. 310, pp. 75–80, 2013.

[144] L. A. Giannuzzi, J. L. Drown, S. R. Brown, R. B. Irwin, and F. A. Stevie, "Applications of the FIB lift-out technique for TEM specimen preparation," *Microscopy Research and Technique*, vol. 41, no. 4, p. 285, 1998.

[145] M. Li, W. Y. Chen, and P. M. Baldo, "In situ transmission electron microscopy with dual ion beam irradiation and implantation," *Materials Characterization*, vol. 173, no. November 2020, p. 110905, 2021.

[146] D. Williams and C. Carter, *Transmission Electron Microscopy: A Textbook for Materials Science*, vol. 1 of *Cambridge library collection*.
Springer, 2009.

[147] D. Fournier, G. L'Esperance, and R. G. Saint-Jacques, "Systematic procedure for indexing HOLZ Lines in convergent beam electron diffraction patterns of cubic crystal," *J Electron Microsc. Tech.*, vol. 13, no. 2, p. 123, 1989.

[148] W.-S. Han, S.-O. Kang, and I.-H. Su, "An Easier Way to Calculate the Crystallographic Interplanar Angles," *Korean J. Crystallography*, vol. 18, no. 1/2, pp. 7–9, 2007.

[149] M. Klinger and A. Jäger, “Crystallographic Tool Box (CrysTBox): Automated tools for transmission electron microscopists and crystallographers,” *Journal of Applied Crystallography*, vol. 48, no. 2015, p. 2012, 2015.

[150] G. Chen, H. Lu, J. Cui, H. Yu, B. Wang, Y. Liu, H. Li, and N. Jiang, “In situ real-time study buckling behavior of boron nitride nanotubes with axial compression by TEM,” *Chinese Chemical Letters*, vol. 30, no. 7, p. 1401, 2019.

[151] Y. Q. Wu, S. Gao, R. K. Kang, and H. Huang, “Deformation patterns and fracture stress of beta-phase gallium oxide single crystal obtained using compression of micro-pillars,” *Journal of Materials Science*, vol. 54, no. 3, pp. 1958–1966, 2019.

[152] Y. Wu, Q. Rao, J. P. Best, D. Mu, X. Xu, and H. Huang, “Superior Room Temperature Compressive Plasticity of Submicron Beta-Phase Gallium Oxide Single Crystals,” *Advanced Functional Materials*, vol. 32, no. 48, 2022.

[153] P. Kumar, K. V. Agrawal, M. Tsapatsis, and K. A. Mkhoyan, “Quantification of thickness and wrinkling of exfoliated two-dimensional zeolite nanosheets,” *Nature Communications*, vol. 6, p. 7128, 2015.

[154] R. A. Evarestov, A. Platonenko, D. Gryaznov, Y. F. Zhukovskii, and E. A. Kotomin, “First-principles calculations of oxygen interstitials in corundum: A site symmetry approach,” *Physical Chemistry Chemical Physics*, vol. 19, no. 37, p. 25245, 2017.

[155] I. Levin and D. Brandon, “Metastable alumina polymorphs: Crystal structures and transition sequences,” *Journal of the American Ceramic Society*, vol. 81, no. 8, p. 1995, 1998.

[156] Y. Tomokiyo, T. Manabe, and C. Kinoshita, “Structural change induced near surfaces of α-Al_2O_3 during electron irradiation,” *Microsc. Microanal. Microstruct.*, vol. 4, no. 1993, p. 331, 1993.

[157] M. Rudolph, M. Motylenko, and D. Rafaja, “Structure model of γ-Al_2O_3 based on planar defects,” *IUCrJ*, vol. 6, no. 1, p. 116, 2019.

[158] A. Dauger and D. Fargeot, “T.E.M. study of Al_2O_3 metastable phases,” *Radiation Effects*, vol. 74, no. 1-4, p. 279, 1983.

[159] W. J. Weber, D. M. Duffy, L. Thomé, and Y. Zhang, “The role of electronic energy loss in ion beam modification of materials,” *Current Opinion in Solid State and Materials Science*, vol. 19, no. 1, pp. 1–11, 2015.

[160] A. Debelle, M. Backman, L. Thomé, W. J. Weber, M. Toulemonde, S. Mylonas, A. Boulle, O. H. Pakarinen, N. Juslin, F. Djurabekova, K. Nordlund, F. Garrido, and D. Chaussende,

"Combined experimental and computational study of the recrystallization process induced by electronic interactions of swift heavy ions with silicon carbide crystals," *Phys. Rev. B*, vol. 86, p. 100102, Sep 2012.

[161] W. A. Hanson, M. K. Patel, M. L. Crespillo, F. Zhang, S. J. Zinkle, Y. Zhang, and W. J. Weber, "Ionizing vs collisional radiation damage in materials: Separated, competing, and synergistic effects in Ti_3SiC_2," *Acta Materialia*, vol. 173, pp. 195–205, 2019.

[162] W. H. Bragg and R. Kleeman, "On the α particles of radium, and their loss of range in passing through various atoms and molecules ," *The London, Edinburgh, and Dublin Philosophical Magazine and Journal of Science*, vol. 10, no. 57, p. 318, 1905.

[163] J. Oddershede and J. R. Sabin, "Bragg rule additivity of bond stopping cross sections," *Nuclear Inst. and Methods in Physics Research, B*, vol. 42, no. 1, p. 7, 1989.

[164] W. Brandt and M. Kitagawa, "Effective stopping-power charges of swift ions in condensed matter," *Phys. Rev. B*, vol. 25, pp. 5631–5637, May 1982.

[165] J. F. Ziegler, "Stopping of energetic light ions in elemental matter," *Journal of Applied Physics*, vol. 85, no. 3, p. 1249, 1999.

[166] P. Gacs, "Reliable cellular automata with self-organization," *Annual Symposium on Foundations of Computer Science - Proceedings*, pp. 90–99, 1997.

[167] A. M. Turing, "The chemical basis of morphogenesis," *Philosophical Transactions of the Royal Society of London. Series B, Biological Sciences*, vol. 237, no. 641, pp. 37–72, 1952.

[168] X. Ma, Y. Zhang, L. Dong, and R. Jia, "First-principles calculations of electronic and optical properties of aluminum-doped β-Ga_2O_3 with intrinsic defects," *Results in Physics*, vol. 7, pp. 1582–1589, 2017.